UNIVERSITÀ DEL SALENTO
FACOLTÀ DI SCIENZE MM. FF. NN.

Dott.ssa Anna Karen Calabrese Melcarne

PhD Thesis

TIME MEASUREMENTS WITH THE ARGO-YBJ DETECTOR

Advisor: Prof. Paolo Bernardini

Coordinator: Prof. Gilberto Leggieri

Dottorato di Ricerca in Fisica XIX ciclo
settore scientifico FIS/04

Introduction

The present thesis has been developed in the ARGO-YBJ experiment, a ground-based observatory at Yangbajing (Tibet) with the main aim to study cosmic rays, in particular γ-radiation at energy threshold of few hundreds of GeV. This goal is achieved by operating with a full coverage array of ~ 6500 m^2 at high altitude (4300 m a.s.l) tackling the low flux of cosmic rays. ARGO is an EAS (Extensive Air Showers) detector and has the capability to sample and reconstruct the shower front of atmospheric cascades by means of good intrinsic time resolution and high space-time granularity.
The first chapter is dedicated to a general overview of the characteristics of EAS pointing out the differences between electromagnetic and hadronic cascades and describing in particular the experimental techniques for γ-ray astronomy. The second chapter provides a description of the ARGO-YBJ detector showing its present status and the main performances that allow for a detailed space-time picture of the shower front and for a continuous monitoring of the all-sky. Moreover a description of the official procedure for the event reconstruction is shown, then the detector monitoring and data analysis are described. In the third chapter is pointed out the importance of a firm calibration in EAS experiments and an original timing off-line calibration method is presented. This method is based on the correction of the systematic time differences between detector units (differences of the transit time of signals from different parts of the detector), which lead to worse angular resolution and wrong reconstruction of the primary direction. The technique has been confirmed by means of simple simulations and it has been developed to work well also when additional systematics due to physics effects (for instance the geomagnetic effect on the secondary particles of the showers) should be taken into account. This procedure is applied to data of ARGO-YBJ experiment (fourth chapter). Moreover all improvements of the method are here described. A complete simulation, using Corsika code to simulate the development of EAS in the Earth's atmosphere up to the ARGO-YBJ altitude and ARGOG program to simulate the detector response, is presented to validate the procedure. Further checks are also presented to confirm the calibration procedure and an estimate of the geomagnetic effect is made by means of simulation. The last chapter shows the effective improvements due to the timing calibration, in particular here the improvements of angular resolution and absolute pointing are shown. The procedure permitted also to start a detailed study of the cosmic ray

showers front. Preliminary measurements of the average EAS disk structure are presented and a first comparison between data and simulation is shown pointing the differences. A more detailed analysis of this measurements could permit a better determination of EAS disk structure and derive hints on shower age, energy and mass composition.

Contents

1

Cosmic rays

Particles coming from outside the Earth's atmosphere constitute the primary cosmic radiation. This is composed by protons, alpha particles, heavier nuclei, electrons and photons. Those are usually meant when talking about cosmic rays. The origin of cosmic rays is still unknown and is the burning question in high energy astrophysics research. Because of their low flux at energies up to 10^{14} eV, indirect measurements studying EASs (Extensive Air Showers) features are needed to get more informations about the nature and the origin of cosmic rays. The cosmic rays will hardly ever hit the ground but will collide (interact) with nuclei of the air, usually several ten kilometers high. In such collisions, many new particles are created and the colliding nuclei evaporate to a large extent. Most of the new particles are π-mesons (pions). Neutral pions decay very quickly, usually into two gamma-rays. Charged pions also decay but after a longer time. Therefore, some of the pions may collide with nuclei of the air before decaying, which would be into a muon and a neutrino. The fragments of the incoming nucleus also interact again, also producing new particles. The gamma-rays from the neutral pions may also create new particles, an electron and a positron, by the pair-creation process. Electrons and positrons in turn may produce more gamma-rays by the bremsstrahlung mechanism. Being charged particles, cosmic rays are scattered and isotropised by the galactic magnetic field and hence lose their original directions. If a neutral radiation like photons (γ-ray) is associated with the presence of energetic particles in a source, they travel in straight lines and their sources can be identified. Thus γ ray astronomy, the study of high energy photons coming from the astrophysical sources, becomes important not only because it permits to study the fenomenology of the sources but also because it provides constraints on the models of acceleration and radiation processes at extreme conditions. There are two main detection methods for γ rays: the first one consists in detecting γ rays directly by

satellite-based telescopes that convert the photon and track the resulting electron-positron pair to determine the photon direction; the second one consists in detecting the EASs produced by interaction of photons with the Earth's atmosphere, using ground-based instruments. Satellite experiments have succeded in detecting photons with energy up to $\sim$ 30 GeV, while ground-based observation lie in the energy range above $\sim$ 100 GeV. This chapter is essentially focused on ground based techniques providing a wide description of the EASs main features.

1.1 Cosmic rays and their origin

Almost 100 years after the first observations of cosmic radiation, the origin of cosmic rays (CR) is not yet fully known. Their elemental composition is still today an open question. At energies around 1 GeV/A all elements known from the periodic table with nuclear charge number Z from 1 to 92 have been found in CRs [2, 3]. Overall, the abundance of elements in CRs is very similar to the abundance found in the solar system, which indicates that CRs are "regular matter" but accelerated to very high energies. This is emphasized by measurements of the CRIS experiment [4] which show that the abundances of particular isotopes in cosmic rays and in the solar system differ by less than 20 %.
The bulk of CRs is assumed to be accelerated in blast waves of supernova remnants (SNRs). This goes back to an idea by Baade and Zwicky who proposed SNRs as cosmic-rays sources due to energy balance considerations [5]. The power required to produce all galactic cosmic rays can be estimated to be $L_{CR} = \frac{v_D \cdot \rho E}{\tau_r} \simeq 5 \cdot 10^{40}$ erg/s, where v_D is the volume of the galactic disk, ρE is the local energy density of cosmic rays, τ_r is their residence time in the volume v_D. Supernovae can supply $L_{SN} \simeq 3 \cdot 10^{42}$ erg/s . They realized that the power necessary to sustain the cosmic-ray flux could be provided when a small fraction $\sim$ 2% of the kinetical energy released in supernova explosions is converted into CRs. Fermi proposed a mechanism to accelerate particles with moving magnetic clouds [6]. This led to todays picture that the particles are accelerated at strong shock fronts in SNRs through first-order Fermi acceleration [7, 8].
Fig. 1.1 shows the observed cosmic rays spectrum at the top of the atmosphere. It extends up to 10^{21} eV, covering more than 10 orders of magnitude in energy. It can be well represented by a power law function as

$$N(E)dE = KE^{-\alpha}dE \tag{1.1}$$

where α is the spectral index.

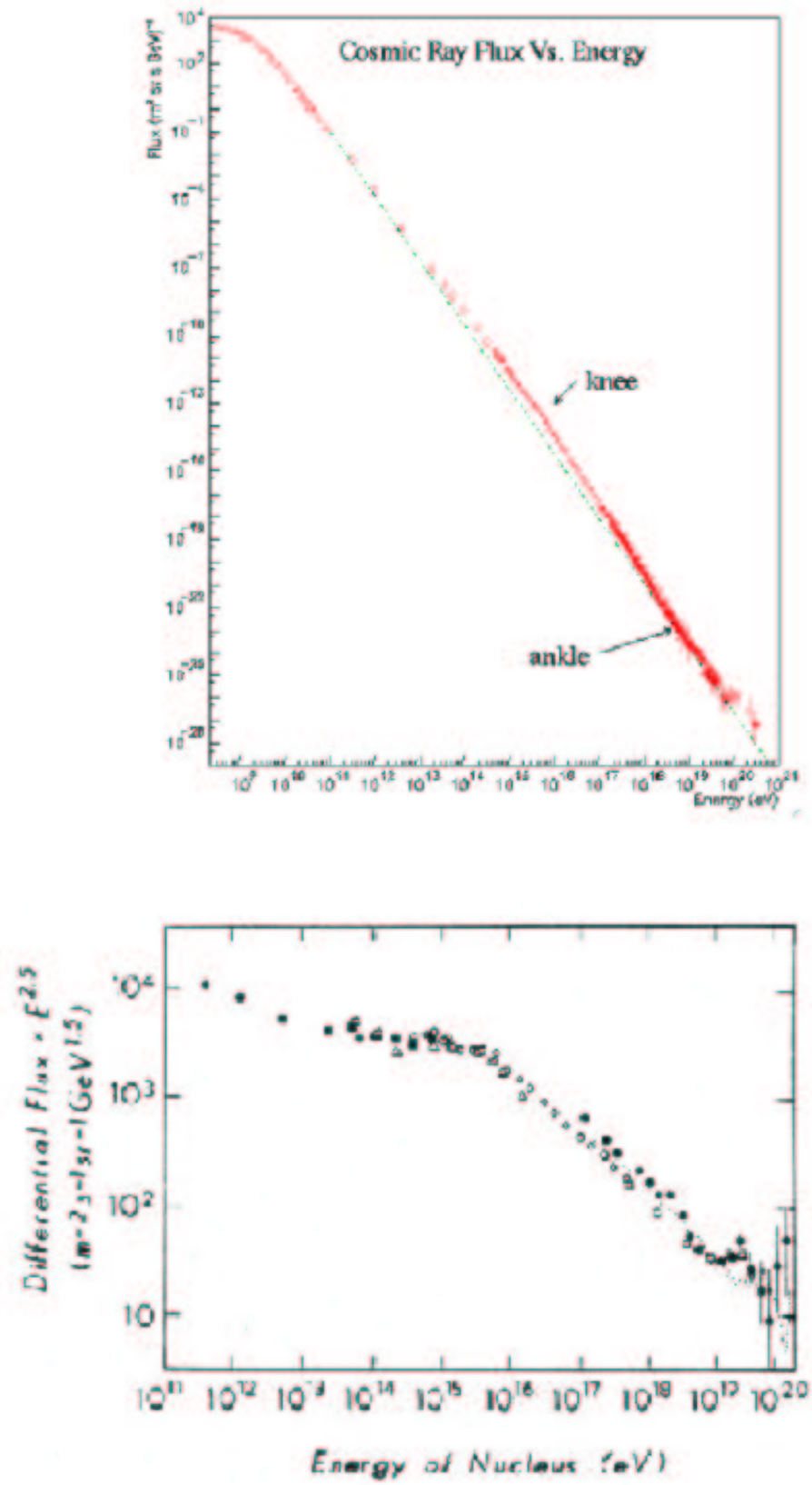

Figure 1.1: Cosmic rays all particle spectrum; $E > 1$ GeV (first plot) and the range from 10^{11} up to 10^{20} eV (second plot).

Its value is between 2.5 and 2.7 up to $10^{15} \div 10^{16}$ eV. The flux decreases from values of several 1000 $(m^2 \cdot sr \cdot s)^{-1}$ at GeV energies to values below 0.01 $(km^2 \cdot sr \cdot year)^{-1}$ at energies exceeding 100 EeV.
At a closer look some structures are seen in the spectrum. The slope of the spectrum changes twice, as it is shown in Fig. 1.1: the first change is in fact at $10^{15} \div 10^{16}$ eV and it is called *the knee*, while the second one is *the ankle* at about 10^{19} eV. The origin of these features are not yet understood, however all theoretical models which try to explain the cosmic ray origin and their acceleration mechanism must include them. Nearly the totality of the cosmic rays flux is thought to be of galactic origin. In many contemporary hypotheses [9] for galactic cosmic rays, *the knee* is attributed to a cut-off for the flux of light elements at energies of several PeV, while the flux of heavier elements is supposed to continue to higher energies. These models expect that primary particles acceleration and propagation is due to magnetic fields, whose effect depend on particle rigidity ($\propto A/Z$), as long as energy losses and interaction effects are small. Supernova remants (SNRs) are thought to be the favourite candidates for the source of cosmic rays with energy up to about $Z \cdot 10^{14}$ eV. The flatter spectrum above *the ankle* is instead interpreted as a cross over from a steeper galactic component, no more confined by galactic magnetic field at those energies, to a new component. This component is generally thought to be extra-galactic.

1.1.1 γ ray Astronomy

Charged cosmic particles bend in presence of magnetic fields: the bending radius R (expressed in cm) of a particle with charge Ze and momentum p (in PeV/c), traveling in a magnetic field B (in μG) is $R = \frac{0.01 \cdot p}{Ze \cdot B}$. The magnetic field in our galaxy is ~ 1 μG and it is roughly parallel to the local spiral arm, but with large fluctuations. Thus, even for protons of energy equal to 10^{19} eV, coming from some galactic source 10 kpc far from Earth, the origin direction is completely lost. Therefore one way to get information about cosmic ray origin is to observe the high energy photons (which do not bend in presence of magnetic fields) produced in the interaction of accelerated particles with matter. During the last 15 years γ astronomy emerged as a powerful tool to gain insight into a number of physical problems related with the most extreme phenomena that occur in the Universe including the origin and the acceleration mechanisms of Cosmic Rays and the study of the last stages of stellar evolution (Supernova Remnants, neutron stars, black holes, etc.).
Photons with energy higher than 0.5 MeV are known as γ rays. The high energy domain (above 30 MeV) spans several decades in the highest end of

the observable electromagnetic spectrum, thus requiring different detection techniques. For this reason the high energy γ ray spectrum is conventionally divided into subranges approximately corresponding to the energy bands over which the different experimental techniques are used. In the VHE (Very High Energy) range (30 GeV - 30 TeV) the low fluxes and the spectral slope of the typical sources require the use of indirect measurements with very large detectors. Due to the opacity of the atmosphere to VHE photons, only the secondary effects of the atmospheric absorption can be detected. Until now three experimental approaches have been used: measurement of the Cherenkov light, fluorescence light observation and collection of the charged particles of the Extensive Air Shower (EAS) using detectors scattered over wide areas.

1.2 Extensive Air Showers and their main features

Above 10^{14} eV the techniques used to study cosmic rays, because of their low flux, exploit the phenomenon of EAS discovered in 1938 independently by Auger [10] and Kohlhorster [11]. A primary cosmic ray entering the atmosphere interacts with electrons and nuclei of atoms and molecules constituting the air: secondary particles can thus be produced. These (together with the primary) proceed to make further collisions, and the number of particles grows. The particle cascade thus formed is named Extensive Air Shower (EAS). Eventually the energy of the shower particles is degraded to the point where ionization losses dominate, and their number starts decreasing. All particles suffer energy losses through hadronic and/or electromagnetic processes. A very energetic primary can create millions of secondaries that begin to spread out laterally more and more from the central axis of the cascade, along their path through the atmosphere, because of transverse momenta acquired by the secondary particles at creation and due to scattering process. Most of these particles will arrive within some hundred meters from the axis of motion of the original particle, now the shower axis. But some particles can be found even kilometers away. Along the axis, most particles can be found in a kind of disk only a few meters thick and moving almost at the speed of light. The bulk of them (Fig. 1.2) produced in hadronic collisions with air nuclei are pions and kaons, which can decay into muons and neutrinos before interacting, thus producing the most penetrating component of atmospheric showers: the muon component. The most intense component, electrons and photons, originates mainly from the fast decay of neutral

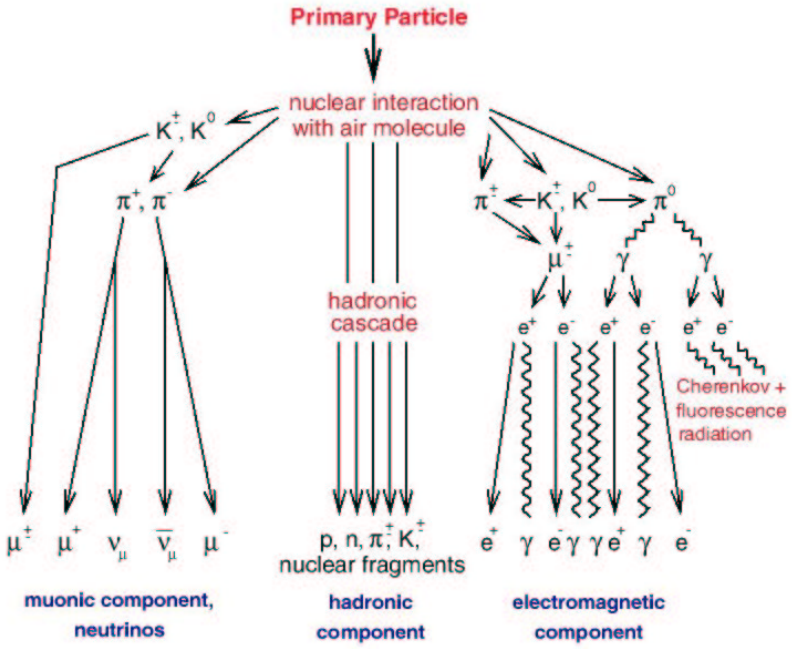

Figure 1.2: EAS progeny.

pions into photons, which initiate electromagnetic showers, thus distributing the originally high energy of the primary particle over millions of charged (and neutral) secondary particles. The longitudinal development of the electromagnetic component shows a growth, a maximum and a decay as the energy of the shower is dissipated. In contrast the muon cascade grows and maximizes, but the decay is only slow as a consequence of the relative stability of muons and the small energy losses by ionization and pair production. The backbone of an air shower is the hadronic component of nucleons, pions and other particles, which feeds the electromagnetic and muonic components. It is often stated that the hadronic component is well concentrated around the shower axis. Nevertheless due to multiple scattering, neutrons in particular, are also distributed far off the centre. The longitudinal EAS profile, i.e. the development of the number of charged particles (shower size) with the cumulated atmospheric depth X (the atmospheric thickness already crossed) can be adequately parameterized by the Gaisser-Hillas function [12], for the electron size, e.g.

$$N_e(X) = N_e^{max} \cdot \left(\frac{X - X_0}{X_{max} - X_0} \right)^{(X_{max} - X_0)/\lambda} \cdot \exp\left(\frac{X_{max} - X}{\lambda} \right) \qquad (1.2)$$

with X the depth at observation, X_0 the depth of the first interaction, and X_{max} the depth of the shower maximum. The attenuation parameter λ is about 70 g cm^{-2}. The difference $(X_{max} - X_0)$ depends on the energy E_0 and the nature of the primary and the difference $(X - X_{max})$ is an indicator of the stage of the development and increases approximately logarithmically with the energy. According to the superimposition model which considers a heavy primary A as a swarm of A nucleons of correspondingly reduced energy, the position of X_{max} depends on E_0/A so that the shift of X_{max} for an EAS induced by a nucleus is proportional to lnA and leads to a shift $\left(X^p_{max} - X^{Fe}_{max}\right) \simeq 100$ g $\cdot cm^{-2}$. This is an essential feature for the mass discrimination. Thus MC simulations shows clear differences in the average longitudinal development of EAS induced by different primaries (Fig. 1.3). The shower development of a heavy ion induced shower starts earlier, and reaches the maximum earlier than proton induced showers of the same energy. Gamma ray induced showers would show much less fluctuations and are poor in muons due to the small cross-sections of meson production by photons and electromagnetic muon pair creation.
The charged particles, particularly the electromagnetic component, are accompanied by an additional EAS phenomenon, the production of atmospheric Cherenkov light which carries information about the longitudinal shower development, especially about the height X_{max} of the shower maximum. At higher energies the shower can be efficiently observed by the fluorescence light of N_2 molecules, induced by the charged particles in air. Air Fluorescence abservations are able to reconstruct the longitudinal shower profile.

1.2.1 Electromagnetic Cascades

Electromagnetic air-showers are cascades initiated in the atmosphere by photons, electrons or positrons, as is shown schematically in Fig. 1.4. Photons are attenuated in matter via photoelectric effect, Compton scattering and pair production. In air, the last one dominates above few tens of MeV. High energy electrons predominantly lose energy in matter by ionisation and bremsstrahlung. The critical energy E_c, that is the energy at which ionization losses and radiative losses are equal, is about 85 MeV in air. Thus the development of the electromagnetic cascade is governed by bremsstrahlung from electrons and pair production from photons. At high energies, the pair production length is approximately equal to the radiation length for bremsstrahlung. Indeed, the cross section for pair production can

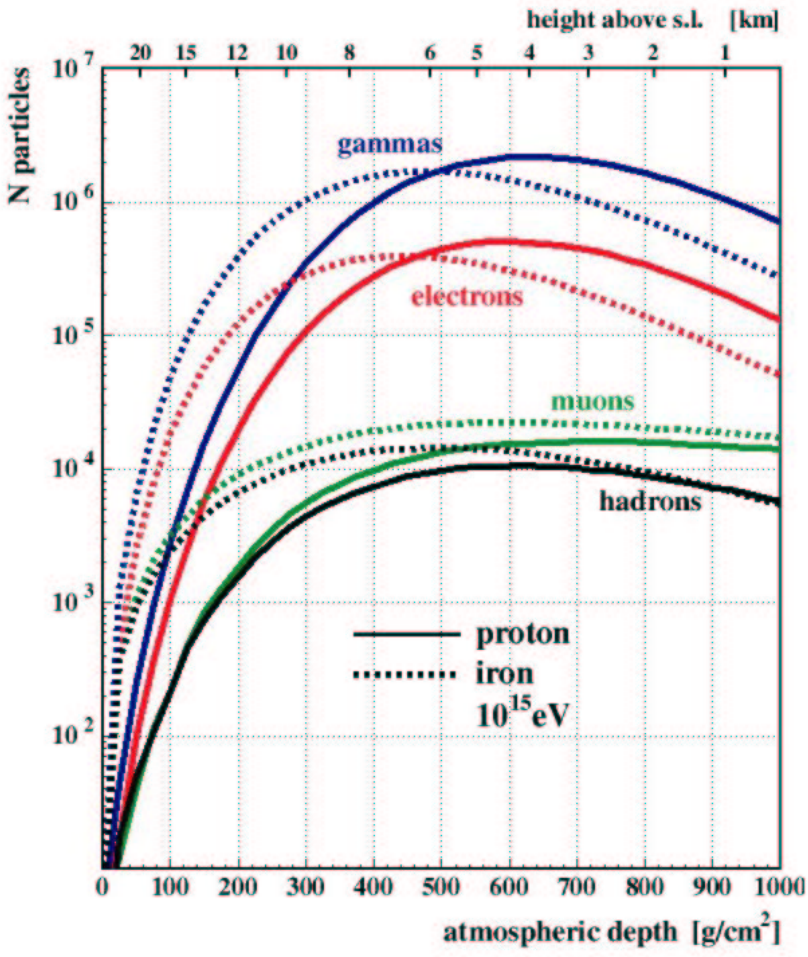

Figure 1.3: Longitudinal EAS development of the average total intensities (sizes) of different particle components of EAS of vertical incidence (from MC simulations by Corsika [13]). The primary is a proton or an iron nucleus with an energy of 10^{15} eV.

approximately be written as

$$\sigma_{pair} \simeq \frac{7}{9} \cdot \frac{A}{N_A} \cdot \frac{1}{X_0} \tag{1.3}$$

where X_0 is the radiation length and N_A is the Avogadro number. Moreover, the energy of the incident particle, at each interaction step, can be assumed to be equally shared among the particles participating in the process. A very simple model can be built to describe the main feature of particle multiplication in electromagnetic showers: a primary photon of initial energy

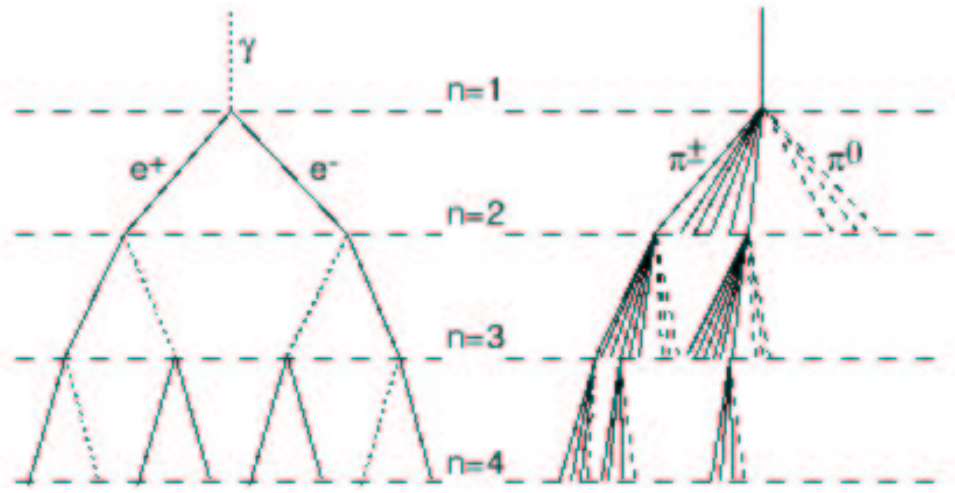

Figure 1.4: Schematic view of an electromagnetic cascade (left) and a hadronic shower (right).

E_0 generates an e^+e^- pair. An electron radiates a single photon after traveling one splitting length $d = X_0 \cdot ln2$, where X_0 is the radiation length ($X_0^{air} = 36.66\ g/cm^2$). An electrons looses on average half of its energy through radiation over the distance d. After traveling the same distance a photon splits into an e^+e^- pair. In either instance, the energy of a particle is assumed to be equally divided between two outgoing particles. After n splitting lengths, at a distance $x = nX_0ln2$, the total shower size (electrons and photons) is $N = 2^n = exp(x/X_0)$ and the initial energy E_0 is distributed over N particles. The splitting continues until the energy per particle E_0/N is too low for pair production or bremsstrahlung. A shower initiated by a primary photon reaches its maximum size N_{max} when all particles have the energy E_c, which means $E_0 = E_cN_{max}$. The penetration depth X^γ_{max} at which the shower reaches its maximum is obtained by determining the number n_c of splitting lengths, required to reduce the energy per particle to E_c. Since $N_{max} = 2^{n_c}$, the number of splitting lengths is $n_c = ln(E_0/E_c)/ln2$, giving $N_{max} = E_0/E_c$ and

$$X^\gamma_{max} = n_cX_0ln2 = X_0ln(E_0/E_c) \tag{1.4}$$

The elongation rate Λ specifies the increase of X_{max} with energy E_0 and is defined as $\Lambda \equiv dX_{max}/dLogE_0$. Eq. 1.4 gives $\Lambda^\gamma = ln10 \cdot X_0 = 84.4$ g/cm^2 per decade of primary energy for electromagnetic showers in air. Thus $X_{max} = 597g/cm^2 + 84g/cm^2 \cdot lg(E_0/PeV)$ is expected. So, X^γ_{max}, the depth at which the shower contains the maximum number of particles N_{max}, depends logarithmically on the primary energy, while N_{max} depends linearly on the incident energy.

1.2.2 Hadronic showers

The hadronic showering process is dominated by a succession of inelastic hadronic interactions. Hadronic cosmic rays entering the atmosphere are subject to strong interactions in collisions with atmospheric nuclei, such as nitrogen and oxygen. Part of the primary energy is transformed into rest mass of new hadrons (mostly pions, and sometimes kaons), another part of it goes into their kinetic energy, and another part goes into disrupting the target nucleus with subsequent emission of protons and neutrons. Energetic primary particles and, in case of heavy primaries, their spallation [1] fragments, continue to propagate in the atmosphere and interact successively, producing more particles along their trajectories, and likewise for the newly created energetic secondaries. This continues until the energy per hadronic particle drops below $\sim$ 1 GeV, the energy necessary for multiple pion production. The most abundant particles emerging from energetic hadronic collisions are indeed pions, but kaons, hyperons, charmed particles and nucleon-antinucleon pairs are also produced. The development of an EAS for a given energy and primary is mainly dependent on two factors: the inelastic cross-section σ_{inel} of primary and secondary particles with air and the average fraction of the available energy transferred into secondary particles (usually named inelasticity k_{inel}). Cosmic radiation is composed above all by protons, thus the most frequent first interaction is proton-nucleus. Fig. 1.5 shows the total and elastic cross section of the proton-proton interaction. $\sigma_{p,p}$(E) varies slowly over a range of many decades in energy, from$\sim$ 40 mb at 10 GeV to $\sim$ 90 mb at 10^7 GeV. The interaction mean free path λ_i can be calculated from the interaction cross section σ_i:

$$\lambda_i = \frac{A}{N_A \sigma_i} \tag{1.5}$$

where A is the mass number of the target nucleus. In case of proton inelastic collisions in air, the interaction mean free path is $\lambda_i \simeq 80$ g/cm^2, so protons

[1] A nuclear reaction induced by high energy bombardment and involving the ejection of two or more small particles or fragments leaving only one large residual nucleus.

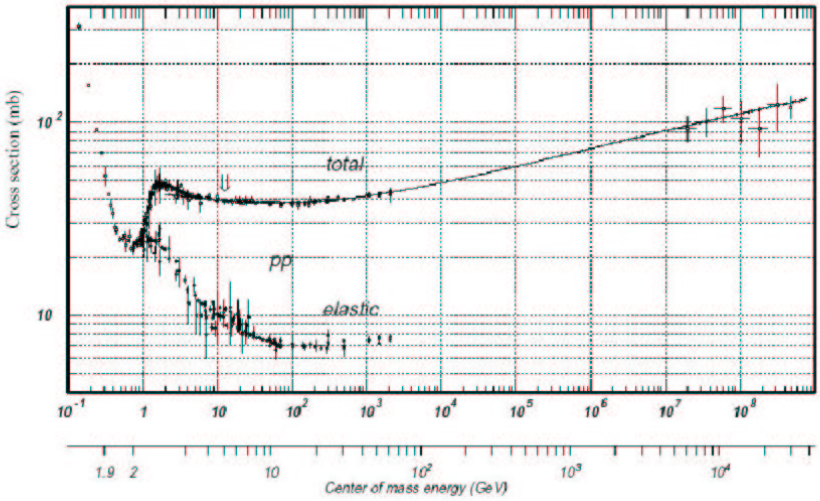

Figure 1.5: Total and elastic pp cross section as a function of laboratory beam momentum and center of mass energy.

undergo on average 12 interactions along a vertical trajectory trough the atmosphere down to sea level. For comparison, for a projectile nucleus with mass number $A = 25$, the interaction mean free path is approximately 23 g/cm^2 in air, corresponding to about 50 interactions for vertical trajectory trough the atmosphere. So there is no chance for a heavy nucleus to penetrate down to sea level. Most of the primary heavy nuclei are fragmented in the first interaction, which occurs at a higher altitude than in the case of protons because of the much larger interaction cross section and correspondingly shorter interaction mean free path.
Hadrons may suffer energy losses due to strong interactions in collisions with nucleons and nuclei when propagating in a medium. A hadron with initial energy E_0, undergoing n interactions with a mean inelasticity $< k >$ will retain on average an energy $E = E_0(1 - \langle k \rangle)^n$. For a vertically incident high energy proton trasversing the full atmosphere down to the sea level, $< k >= 0.5$ and $n = 12$, so that the energy reduction factor is

$$\frac{E}{E_0} = (0.5)^{12} \simeq 2.5 \cdot 10^{-4} \tag{1.6}$$

1.2.3 Characheristics of electromagnetic and hadronic showers

The Fig. 1.6 gives an example of the two kinds of shower having both primary energy equal to 1 TeV: the pure electromagnetic shower is shown on the left side, while the hadronic one is shown on the right side. Cosmic ray showers are much more chaotic than the γ-ray ones, which tend to be very smooth and have most of their particles located near the core. Indeed, the transverse momentum of hadronic interactions is much greater than that of electromagnetic ones; the average transverse momentum of hadronic interactions is approximately 400 MeV, while the transverse momentum characterising the electromagnetic showers is mainly due to the multiple scattering. Secondary particles in electromagnetic showers are mostly electrons, positrons and photons as well as in hadronic ones, but the latter also contain other types of particle among which are muons. Moreover, on average γ ray showers have more particles than cosmic-ray showers of the same energy. This is because much of the energy in cosmic-ray showers is carried off by muons. Since muons do not readily interact, there is less energy available for the production of new particles.

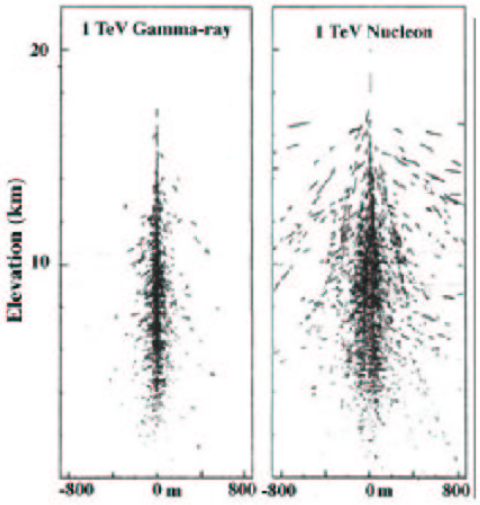

Figure 1.6: Electromagnetic (left) and hadronic (right) air-showers generated by primaries with energy of 1 TeV.

1.3 Experimental technique for γ ray astronomy

Photons from γ ray astrophysical sources, depending on their energy, have to be detected either outside the atmosphere, before interacting with it, by devices located on space vehicles or on the Earth, at sea level or at high mountain altitude, after their interaction with the atmosphere. Fig. 1.7 shows the plot of the γ ray shower size (number of charged particles which develop in the air-shower) as a function of the atmospheric depth or of the altitude at several values of the primary energy: γ rays with energy larger than 10^{11}eV have low probability to be detected on Earth. The atmosphere is opaque to HE photons (30 MeV - 30 GeV) and to some VHE photons (30 GeV - 30 TeV), depending on the observational altitude. In this energy range instruments working outside the atmosphere are needed. Making use of detectors flown on satellites is the simplest way to avoid the problem of the atmosphere. A space borne γ ray detector usually consists in:

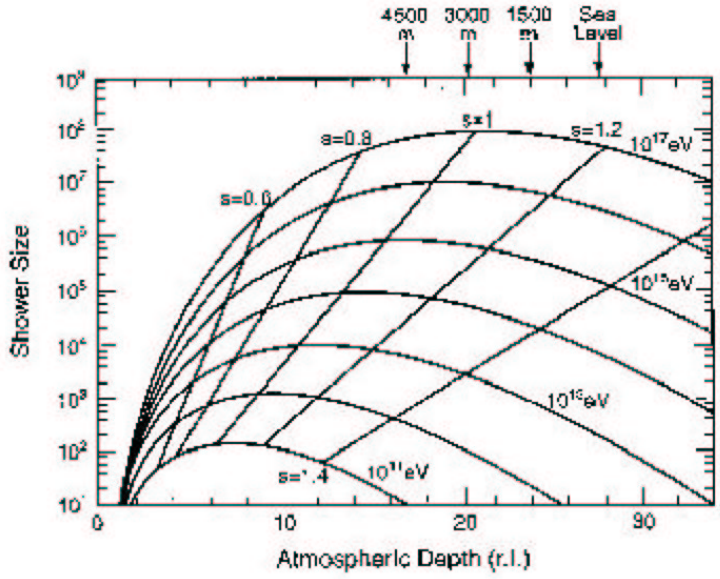

Figure 1.7: Shower size as a function of the atmospheric depth for photon-initiated showers. The values of the energy showed on the curves are the photon primary energies.

- a particle detector in which photons interact, converting into electron-positron pairs, whose tracks are recorded;

- a calorimeter in which electrons and positrons release their energy;
- an anti-coincidence detector constituted by a thin sheet of scintillator, surrounding the tracker to reject charged cosmic rays.

The strong limitation for this technique is the fact that the flux of γ ray source is typically very low and decreases rapidly with the energy: therefore, since the size of the detectors is constrainted by the weight that can be placed on satellites, their collection area is not large. Hence the rapid decreasing of the typical fluxes determines a maximum energy at wich the collection area suffices for a statistically significant detection. EGRET, one of the most successful satellite-experiment, operated in the energy range from 20 MeV to 30 GeV with an energy resolution of about 20%, an angular resolution improving from $\sim 10^\circ$ at 60 MeV to $\sim 0.5^\circ$ at 10 GeV, an effective area of $\sim 1000\ cm^2$ at several hundred MeV and a field of view of ~ 1.5 sr. It reached a 3σ sensitivity limit of $\sim 10^{-7} cm^{-2} s^{-1}$. While the next generation satellite GLAST should be sensitive up to 200 GeV. In the VHE range the low fulxes and the spectral slope of the typical sources require the use of cery large detectors.

1.4 Ground based detectors

Along the last decade, ground-based detection became an effective investigation method. These detectors make use of an indirect technique: the primary particle, a photon from the astronomical source or a cosmic ray, interacts with the atmosphere, producing a lot of secondary particles which in turn interact with the atmosphere. The extensive air-shower formed by the primary can be detected by observing:

- secondary particles on the ground;
- Cherenkov light emitted by charged secondary particles;
- fluorescence light emitted by N_2 molecules excited by charged secondary particles.

The different experimental techniques are summarised in Fig. 1.8 and briefly described in the next sections. Ground -based experiments detect a source as an eccess of events from a certain direction with respect to an overwhelming uniform background. The ratio signal/noise as a function of the detector parameters is considered in the following expression:

$$\left(\frac{signal}{noise}\right) \propto \frac{R_\gamma Q \sqrt{A^{eff} T}}{\sigma_\theta} \tag{1.7}$$

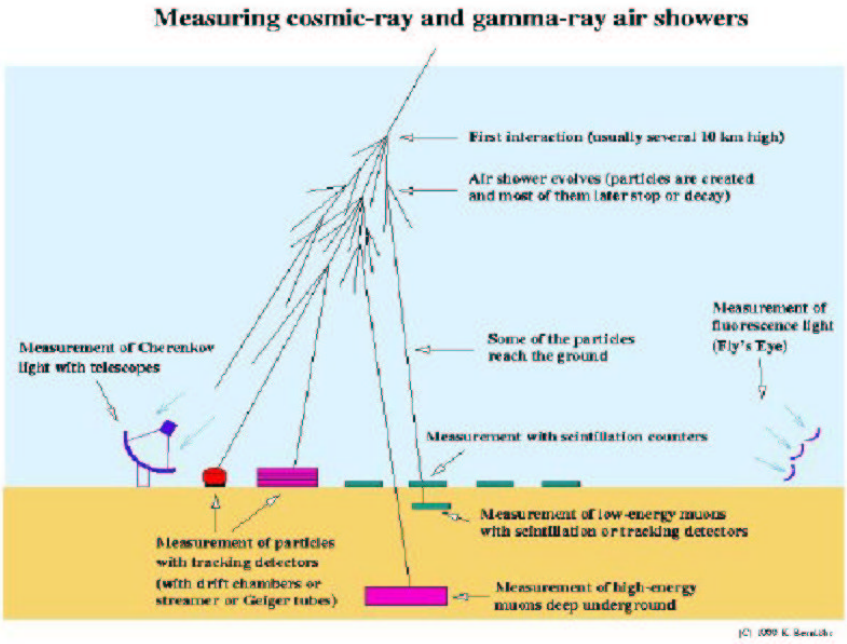

Figure 1.8: Summary of the experimental techniques used in order to detect γ-ray and comic-ray air showers.

where A^{eff} is the effective detector area, T is the exposure time, σ_θ is the angular resolution, R_γ is the relative $\gamma/hadron$ trigger efficiency, Q is the $\gamma/hadron$ identification efficiency. The signal/noise ratio is a linear function of Q and R_γ. The signal depends essentially on the angular resolution because, at least for point sources, a better reconstruction of the direction produces a more narrow spatial distribution of the signal and a smaller amount of background. Further improvements in the sensitivity level can be achieved by rejecting part of the background on the basis of subtle differences in the cascades. On the other hand, the fact that the atmosphere can be considered a part of the detector itself allows for a further increase of the detection area: due to their lateral extension, EAS can be detected even if they partially intersect the detector active area. Therefore, the collection area of a ground-based detector can be much larger than its geometrical extension. Together with the angular resolution and the γ/hadron separation, the following relevant properties characterize a ground-based detector:

- **energy threshold**. Given a minimum number of secondary particles (or Cherenkov photons) required to trigger the detector, the threshold

energy is detemined by the atmospheric absorption. This implies that the threshold becomes higher with the zenith angle because of the increasing thickness of atmosphere and becomes lower with increasing altitude above sea level.

- **field of view (FoV)**. The FoV is the portion of the overhead sky that can be seen at a time. Therefore, it represents the angular limit for the continuous monitoring of the sky.

- **duty cycle**. The time fraction of actual data taking is the temporal limit to the continuous monitoring of the sky.

1.5 Cherenkov light observation

High energy charged particles, moving with a speed higher than the light speed in the medium, generate Cherenkov radiation which is strongly forward peaked with an opening angle, in the air, of $\sim 1.2^{\circ}$ at the emission and can be measured on the ground with light-detector. It is emitted by the shower cascade throughout the atmosphere and offers the possibility of measuring the total energy of the shower and of tracing the shower development. Due to the changing refractive index and the characteristic Cherenkov angle the lateral distribution has a particular structure, and the shape of the distribution around 100 m gets sensitive to the height of emission. The light from the early part, where the energies of the particles are still very high and the Cherenkov photon scattering angles small, is concentrated in a characteristic ring near 100 m. The resulting lateral distribution is the superposition from all heights, and its shape depends on the shower development. If the shower maximum gets nearer to the ground, more light is produced near the shower core. That means the lateral distribution drops faster the closer the shower maximum is to the detector. The simplest configuration of Atmospheric Cherenkov Telescopes (ACTs) is one parabolic or spherical mirror with diamater size between 2 and 10 meters, collecting the Cherenkov light which is then reflected to an array of photomultiplier tubes (PMTs), placed in the focal plane of the mirror. Array of Cherenkov telescopes also exist. Gamma ray observation with these instruments is affected not only by the cosmic ray background but also by the night-sky background, which amounts to about 1 photon ns^{-1} m^{-2}, mostly from the Milky Way. The ratio between the Cherenkov signal S and night-sky background B can be

expressed as:

$$\frac{S}{\sqrt{B}} = \frac{\epsilon A \rho_\gamma}{\sqrt{\Phi_B \Omega A \epsilon t}} = \frac{\rho_\gamma}{\sqrt{\Phi_B}} \sqrt{\frac{A\epsilon}{\Omega t}} \tag{1.8}$$

where A is the collecting area, ρ_γ is the Cherenkov photon density on the ground, ϵ the efficiency of light collection, Φ_B the night-sky background flux, t the width of the trigger time window and Ω the solid angle subtended by each photomultiplier. Eq. 1.8 evidences that in order to improve the Cherenkov light detection, the area A must increase while the time t and the solid angle Ω must be as small as possible. The mirror size is mainly limited by costs. On the other hand the ACTs used in the search for γ ray sources relie on the techniques developed to reject the huge cosmic ray background. These technique exploit the following features:

- The cosmic ray background is uniformly distributed, while the γ rays come from the source direction which is followed by telescope. The reconstruction of the incident direction of the air shower allows to reject events whose reconstructed direction does not match with the source direction.
- The Cherenkov light distribution is different between γ initiated shower and proton initiated one (good hadron rejection).
- The angular resolution is $\sim< 0.1°$.

The angular resolution and sensitivity of ACTs make them ideal to study steady VHE emission as well as short-term flaring from known sources. However, ACTs have a relatively narrow field of view, $\sim 4°$. Thus they are not well suited to perform sky surveys, monitor transient sources for episodic emission, search for transient emission from a source at an unknown direction (such as from a GRB), or to probe structures which are larger than their field of view.

1.6 Fluorescence light observation

The technique relies on the fact that ionizing particles can excite N_2 molecules in the atmosphere. Such excited molecules emit fluorescence photons (typically within $10-50$ ns after excitation). The optical fluorescence comes from various bands of the molecular nitrogen ion, with light emitted between 3000 and 4000 $\mathring{A}$. It happens to be just the wave band for which the atmosphere is quite transparent. The attenuation length is approximately

15 km for vertical incidence. The fluorescence light production efficiency per shower is weakly dependent on pressure and temperature. The fluorescence light is isotropically emitted and can be detected at large distance from the shower axis. Thus it can be distinguished from air Cherenkov light that is emitted in the forward direction and confined to short distances from the shower axis. Fly's Eye was the first air fluorescence detector to produce significant physics results. The fluorescence light is collected using a lens or a mirror and projected onto a camera, located in the focal plane. Essentially the camera is an assembly of a large number of PMTs tubes, each loooking at a certain region of the sky. The camera pixelizes the image and records the time interval of the light arrival in each pixel element. The amount of light detected by each phototube could be related to the number of electrons in the shower at a specific level of the development of the shower. Unlike other detectors this technique allows the direct measurement of the longitudinal development of the EAS. However, such as ACTs, they can only be used on clear, dark nights.

1.7 Extensive Air Shower Arrays

Extensive air-shower particle detector array sample the charged particles of the shower front at ground level. Typically they consist of a certain number of charged particle detectors, usually $\sim 1\ m^2$ scintillation counters, spread over an area of $10^4 - 10^5\ m^2$ with a spacing of $10 - 20$ m. The total sensitive area is therefore less than 1% of the total enclosed area. The shower is sampled at a single depth (the observation level) and with an additional sampling of the shower front at fixed points. This results in a high degree of uncertainty in the reconstruction due to fluctuations. The sparse sampling sets the energy threshold (~ 50 TeV) and determines a poor energy resolution ($\sim 100\%$). The direction of the incoming primary particle is reconstructed with the fast timing method making use of the relative times at which the individual detection units are fired by the shower front. Thus the resolution in the measurement of the primary direction σ_θ is related to the resolution of the relative time measurements and to their total number:

$$\sigma_\theta \propto \frac{\sigma_t}{\sqrt{\rho}} \tag{1.9}$$

where σ_t is the time resolution and ρ is the density of indipendent detector elements sampling the shower front. Once the detector area is larger than the typical lateral extension of air showers, thus providing an optimal lever arm, the angular resolution can be further improved by increasing the

sampling density. Another important parameter of an air-shower detector is its threshold energy. It is generally defined as the primary energy at which the trigger probability reaches either 10 % or 50 %. It depends on the minimum number of counters required in order to reconstruct the events, on the size and spacing of the array detectors and on the location altitude. Usually al least ten counters are required for a good accuracy in the direction reconstruction. The energy threshold is not a well-defined quantity. Fig. 1.9 shows the trigger probability of air-showers as a function of the primary energy. The function describing this relation is not a step-function because of the fluctuations involved in the development of the atmospheric shower, mainly due to the altitude of the first interaction point, and also to the core position and to the incident angle. The energy threshold which is possible to reach by a certain apparatus, lowers with altitude. Fig. 1.10 shows the

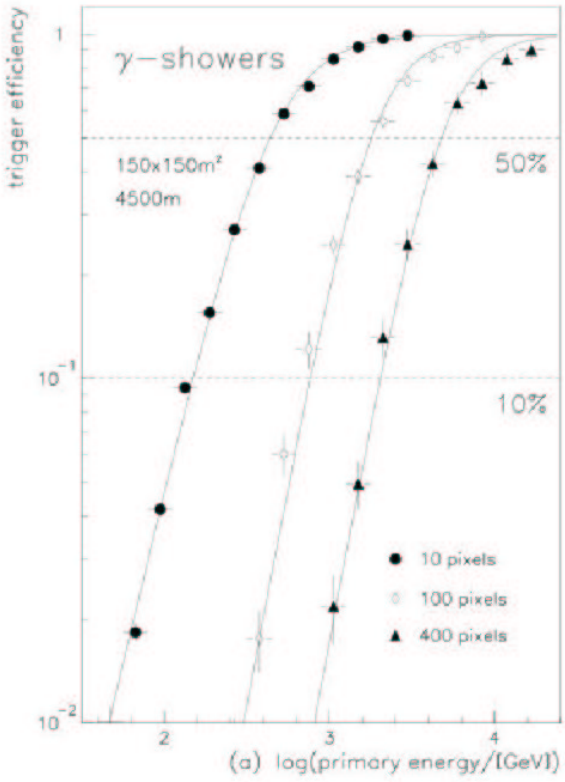

Figure 1.9: Trigger efficiency as a function of the primary particle energy for three trigger conditions (10,100,400 pixels respectively spread on 150 × 150 m^2 at 4500 m of altitude).

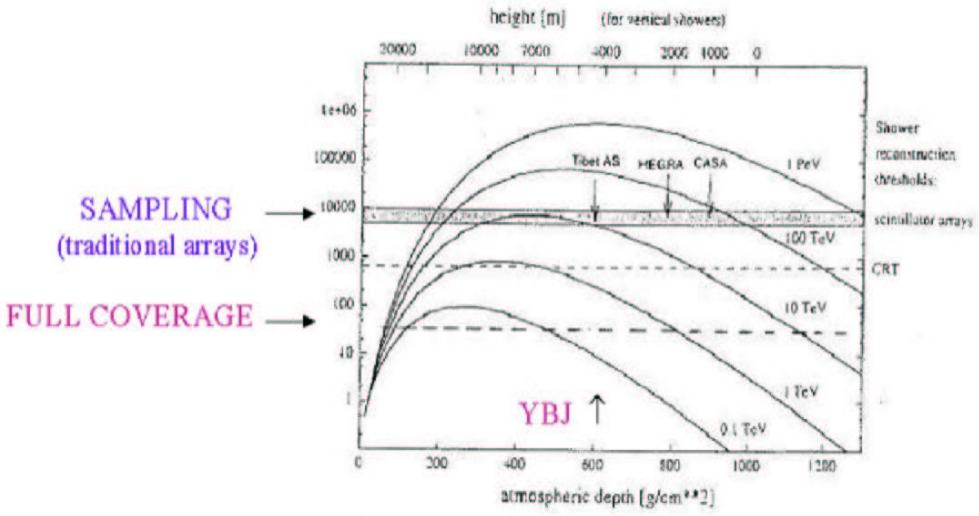

Figure 1.10: Shower size as a function of the atmospheric depth for photon initiated showers. The values of the energy showed on the curves are the photon primary energies.

shower size as a function of the altitude relative to electromagnetic showers for several primary energies. The primary energy of electromagnetic showers with a given size which is possible to observe lowers as the altitude increases. In Fig. 1.10 some examples of shower arrays: CASA, HEGRA and Tibet AS_γ. They use the sampling technique, i.e. the base detectors are spaced. At a given altitude the implementation of the full coverage technique allows lower energy thresholds to be reached: at Yanbaijing site (4300 m a.s.l.), a threshold of few hundreds of GeV can be obtained. The higher energy regions (VHE and above regions) of γ-ray astronomy are not very well explored. Till now no systematic survey of the VHE γ-ray sky has been performed owing to the fact that all VHE detections have been made by means of air-Cherenkov telescopes, which have a duty cycle of $\sim 5-10$ % and relatively narrow field of view ($\sim 10^{-2}$sr). The Milagro [14] and ARGO-YBJ experiments have a peak sensitivity near 1 TeV and a large field of view. They will able to monitor all the sky in the VHE γ-band. In contrast to ACTs they can operate 24 hours per day, regardless of weather, and are able to continuously observe every source in their field of view, every day of the year. Milagro is a water Cherenlov EAS detecor located near Los Alamos at 2360 m sea level, while ARGO-YBJ, that will described in the next chapter, benefits from the much higher altitude (4300 m a.s.l) with respect to Milagro.

2

The ARGO-YBJ experiment

ARGO-YBJ is a full-coverage air shower detector optimized for the detection of cosmic rays and γ radiation with an energy threshold of a few hundreds GeV. It consists of a single layer of RPCs (Resistive Plate Counters) covering an area $\sim 10^4\ m^2$ and providing to image with high efficiency and sensitivity atmospheric showers initiated by primaries of energies up to 500 TeV. The shower array is able to monitor the Northern Hemisphere in the declination band $-10^\circ < \delta < 70^\circ$ continuously and systematically. Since its geographic location (the Yanbajing Cosmic Ray Laboratory has been built at 4300 *ma.s.l.* in Tibet) ARGO-YBJ will exploit the Crab "standard-candle" as a reference photon beam continuously "ON" for developing the experimental technique appropriate to the GeV-TeV γ ray astronomy. Data gathered with ARGO will allow to face a wide range of fundamental issues. The most important of them is γ astronomy: more than 300 galactic and extragalactic point candidate sources can be monitored with a sensitivity to unidentified ones better than 10% of the Crab flux. It is also designed to detect Gamma Ray Bursts at energies above 10 GeV and to make Solar and Heliosphere Physics. The experiment has also the posssibility to measure the antiproton to proton ratio in the TeV range and the primary proton spectrum in the region around the *knee*. Additional objectives will come from using ARGO as a traditional array covering the full energy range from 10^{11} to 10^{16} eV. In fact it has to be stressed that ARGO main features provide a high granularity space-time picture of the shower front, detailed study of shower properties. For instance, multicore-events, time distributions of EAS particles, multifractal structure of particle densities near the core, can be performed with unprecedented resolution. In this Chapter it will be described in detail the detector lay-out, the performances and the present status of the experiment.

2.1 Detector LAY-OUT

The detector is a squared array of 1848 RPC ([25]). It consists of an internal carpet of 1560 RPC which cover an area of $\sim 5772\ m^2$, while the surrounding area is only partially ($\sim$ 50%) instrumented with RPCs increasing the detection area to $10^4\ m^2$ (sea Fig.2.1). The outer ring improves the apparatus

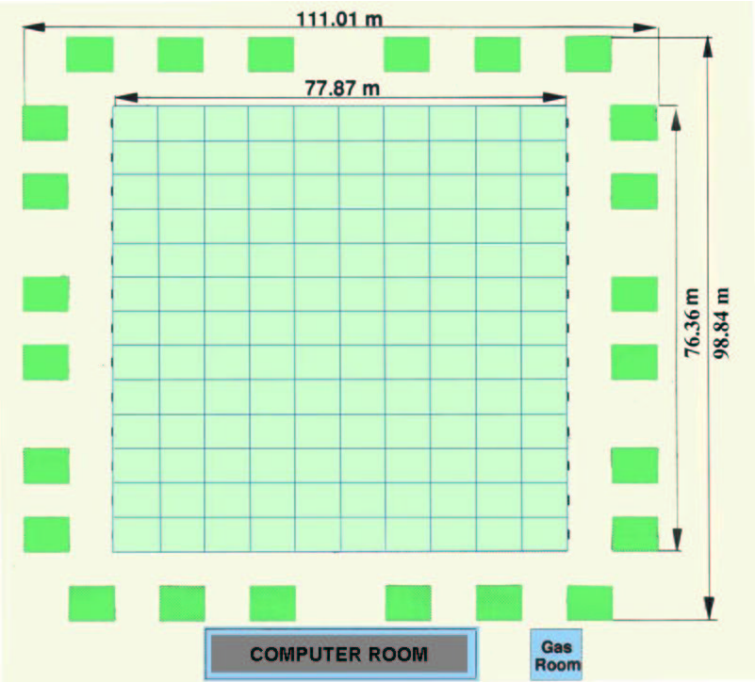

Figure 2.1: Detector lay-out.

performance, enlarging the fiducial area for the detection of showers with the core outside the full coverage carpet. Moreover a lead converter 0.5 cm thick will cover uniformly the carpet: it will work as a photon converter, increasing the number of charged particles and thus lowering the energy threshold. The thickness of the lead layer has been chosen in order to achieve an overall gain in the number of the detected ($\simeq$ 1.8 with respect to the case without converter). At the same time, the absorption process removes particles with a large time delay (due to the low energy), thus reducing the intrinsic time spread of the shower front and allowing for a better angular resolution. The Figs. 2.2 and 2.3 show, respectively, a schematic cross-section of the detector and a picture of the basic element, a RPC.

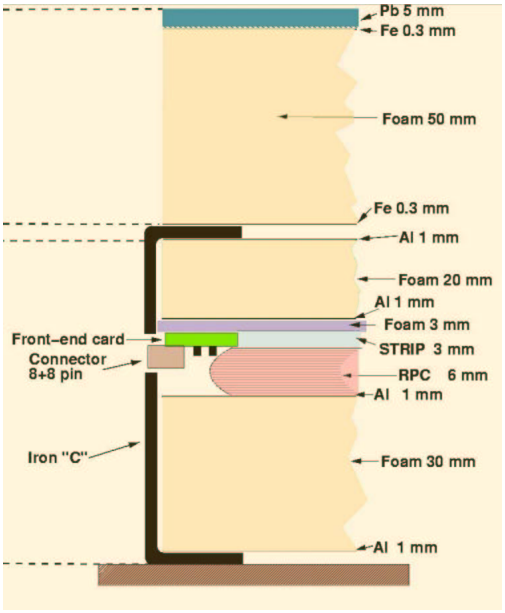

Figure 2.2: Schematic cross-section of the ARGO-YBJ detector.

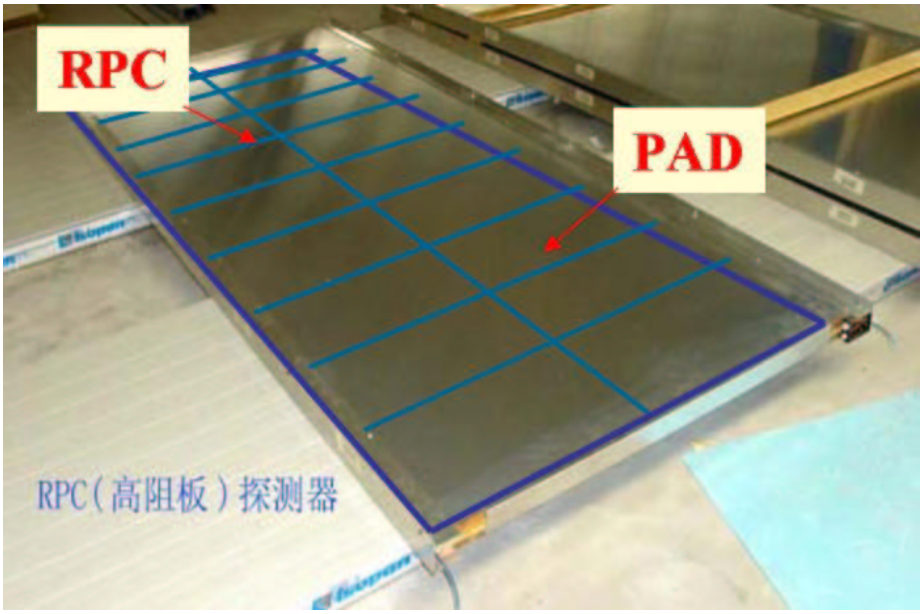

Figure 2.3: Picture of an RPC.

2.2 Resistive plate Counters

RPCs are gaseous detectors which detect the passage of charged particles because of their ionization losses in the gas. The use of RPC in a surface (carpet) set-up allows many advantages, among which are:

- low cost
- high efficiency
- high space and time resolution
- easy access to any part of detector
- robust assembling
- easy to achieve $> 90\%$ coverage
- mounting without mechanical supports

Each counter is assembled in a box of $2850 \times 1225 \times 47\ mm^3$. Two external shaped rigid panels consisting of an Aluminum (200 μm thick) foil, glued on a 1.5 cm foam layer, are used as a protection for the gas volume and to fix the chamber elements. A copper foil (17 μm thick), glued on a PET foil (190 μm) is used for analog read-out of the total induced charge produced in the gas volume (BIG PAD in Fig. 2.4). The copper foil is cut in half in order to obtain two pick-up electrodes of dimension $125 \times 140\ cm^2$ each. The chamber is constituted of a foam layer (3 mm thick) glued on PET foil (250 μ),the gas volume and a strip panel. Two rigid panels sandwich the elements described above: they are connected by Aluminum "L" shaped sections. The gas volume consists of two bakelite electrode plates of volume resistivity in the range $0.5 \div 1 \cdot 10^{12}\ \Omega$ cm, which form a 2mm gas gap. A grid of cylindrical spacers (1 cm diameter, with pitch of 10 cm) is used to guarantee that gas volume planes are flat. The strip panel consists of a sandwich of the following elements:

- a 17 μm copper foil glued on a 190 μm PET foil. The copper foil, faced to the gas volume, is cut into 80 strips of width 6.75 cm and length 61.8 cm.
- 3 mm foam layer
- 17 μm copper foil, glued on a 50 μm PET foil.

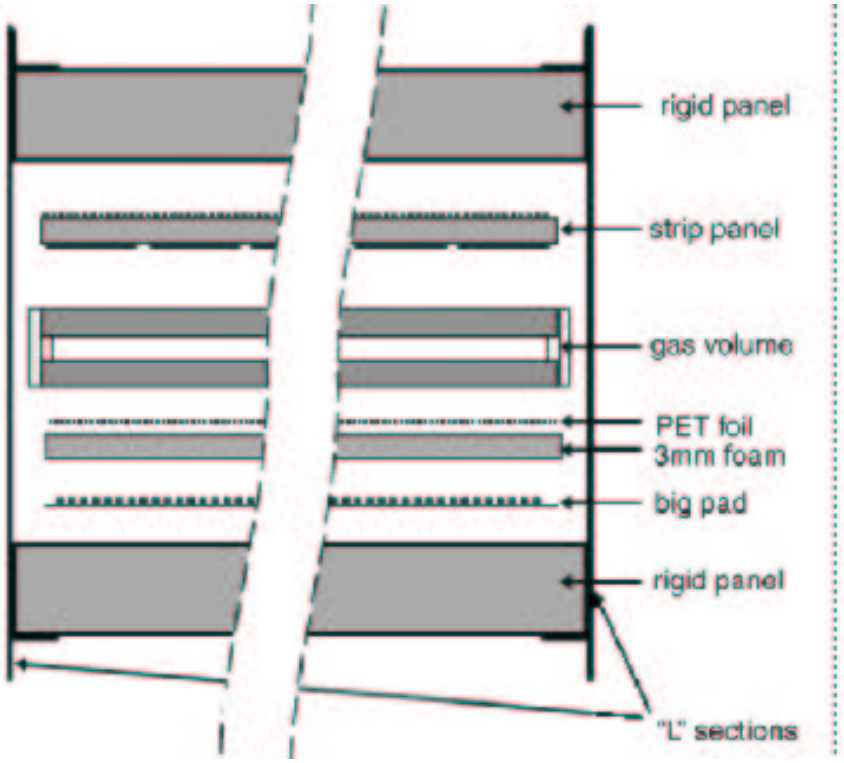

Figure 2.4: Cross view of the ARGO-YBJ RPC.

This copper foil is used as reference ground for the picked-up signals. At the edge of the detector the strips are connected to the front end electronics and terminated with 50 Ω resistors. Eight contiguous strips form a logical PAD ($56 \times 61.8\ cm^2$); the OR of these strips is used for triggering purposes and produces the time signal to be measured by the TDC. The output of each chamber consists of:

- a digital read-out from the PADs used for triggering and space-time reconstruction;
- a pattern of fired strips which allows one to count the number of particles for low density events;
- an analog read-out with charge information collected by two BIG PADS $125 \times 140\ cm^2$.

The counters operate in streamer mode with a gas mixture of Argon (15%), isobuthane (10%) and tetrafluoroethane (75%), at a voltage of 7500 V.

They have a single counting rate below 500 Hz/PAD and provide an efficiency greater than 96% and a time resolution of $\sim$ 1 ns, thus they exhibit high efficiency and excellent time resolution. Since the average strip density is about 22 strips/m^2, it is expected from the digital read-out a particle density of 10 particles/m^2 thereby providing a good linear response. All the enviromental and detector parameters, namely atmospheric pressure, external air temperature (see Sec. 2.8), high voltage power supply, current drawn by each RPC, gas temperature and humidity, are continuously monitored.

2.3 Trigger Logic

The basic detection unit is the CLUSTER, a set of 12 contiguous RPCs. The signals from each CLUSTER are organized by a front-end pre-processing electronics (Local Station) in order to give a continuous counting of the fired PADs (PAD multiplicity) in a time window of 150 ns. This guarantees that the particles of the same shower are in coincidence. At any trigger occurence, the space and time information from each Local Station is collected and elaborated in the Central Station for event building and storage. The energy experimental range is very large, bridging the GeV and TeV energy regions of the showers, and moreover the particle density distribution changes with the distance from the shower axis. Showers with very low energy, in the range of a few hundreds GeV, are expected to fire less than 100 PADs spread on the entire carpet. At very high energy, in the range of tenths of TeV and beyond, the showers present a specific spatial distribution, characterized by a core structure. The trigger logic should be able to select events exceeding a programmable threshold of PADs, fired by the same shower. Three different trigger subsystems have been implemented by ARGO-YBJ:

- Low Multiplicity Trigger (LMT)
- Fast Trigger (FT)
- High Multiplicity Trigger (HMT)

All these triggers are based on the fired PADs counters generated by the Local Stations on a given number of CLUSTERs [26]. The first trigger logic generates a signal when a programmed threshold of fired PADs is reached or exceeded on the entire detector (LM Trigger). A specific threshold can be assigned to each SUPERCLUSTER (4 CLUSTERS) and the module generates a Fast Trigger if at least 1 SUPERCLUSTER hit number exceedes its correspondent threshold. The same procedure is repeated for larger

portions (ULTRACLUSTER,sector and ARGO in time windows respectively of 210,360,420 ns). The third trigger logic produces an output when a programmable threshold of CLUSTERs with a specific multiplicity is excedeed (HM Trigger). The CLUSTERs logic outputs one of the multiplicity buses when respectively : LMT and FT (from ≥ 1 to ≥ 6), HMT (≥ 7, ≥ 16, ≥ 32, ≥ 64) PADs are fired in the CLUSTER.

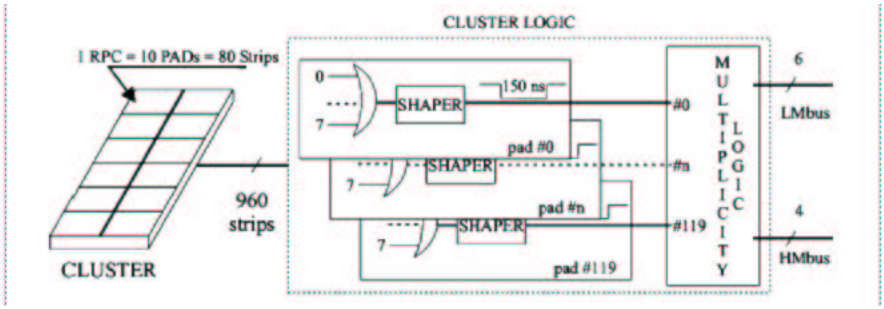

Figure 2.5: The CLUSTER logic diagram.

2.4 Experimental status and observational techniques

Argo-YBJ started the data acquisition at the beginnings of the year 2004, when only 6 CLUSTERs were installed. At present the whole detector has been installed and it is currently operating with about 5600 m^2 of the array (central carpet) in data taking. After the trigger criteria have been met, the information from all the PADs fired within a 2 μs window are stored and constitute what is called the raw event. The number of fired PADs is called event multiplicity. The information stored for each fired PAD is:

- the mask of fired strips within the PAD
- the PAD time

The number of fired strips (strip multiplicity) is an almost direct measurement of the number of charged particles traversing the PAD's area. The times are read by means of a TDC with a 1.042 ns bin, operating in common stop. Presently the detector is operating exploiting two observational techniques. The former is based on the requirement that a minimum number of PADs must be fired in the central carpet (shower mode

technique): Argo-130 CLUSTERs configuration (carpet without the ring) collects data with a trigger LM=20 since July 2006. The detector is working also in scaler mode: the counting rate of ≥ 1, ≥ 2, ≥ 3 and ≥ 4 particles on each CLUSTER in 150 ns coincidence time, is recorded at fixed time intervals (0.5 ns). This technique allows the detection of secondary particles from very low energy showers ($E > 10$ GeV) that reach the ground in a number insufficient to trigger the detector operating in shower mode. In this case the arrival direction is not measured but the single rate measurement will be used to search for low energy transient phenomena such as Gamma Ray Bursts and to study cosmic ray modulations due to solar activity. Moreover, the same data can be used to check the detector stability. The expected rate is $5 \cdot 10^6$ Hz.

2.4.1 Detector performances

The high time resolution and the space granularity of the digital read-out allow for a very detailed image of the shower profile. A good capability of reconstructing the primary particle direction through the shower image is necessary to accomplish the ARGO-YBJ design sensitivity to γ ray sources. Fig. 2.6 shows an example of a shower event detected by ARGO-104. This figure allows to point out how ARGO-YBJ peculiar features give a unique way to deeply investigate the structure and lateral development of EASs, by means of a full space-time reconstruction and the study of the topological structure and time profile of the shower front. Fig. 2.7 provides the image (like a pure space pattern) of a very large shower, most probably initiated by a several TeV primary detected by the whole ARGO-YBJ central carpet (ARG0-130). For this kind of shower events, whose core is inside the active detector area, both the lateral hit density profile and the time width of the shower front can be precisely measured at different distances from the core position. Moreover,for such very energetic shower events saturating the digital strip information, the charge read-out has been implemented by instrumenting each RPC also with two large size PADs. The analog charge information from a BIG - PAD large one half of the RPC area is then digitized and included in the normal event data stream. Fig. 2.8 is an example of the events as seen by the analog read-out, where the highest charge peak corresponds to about 3500 particles intercepting one BIG - PAD ($\sim$ 2000 charged particles/m^2).

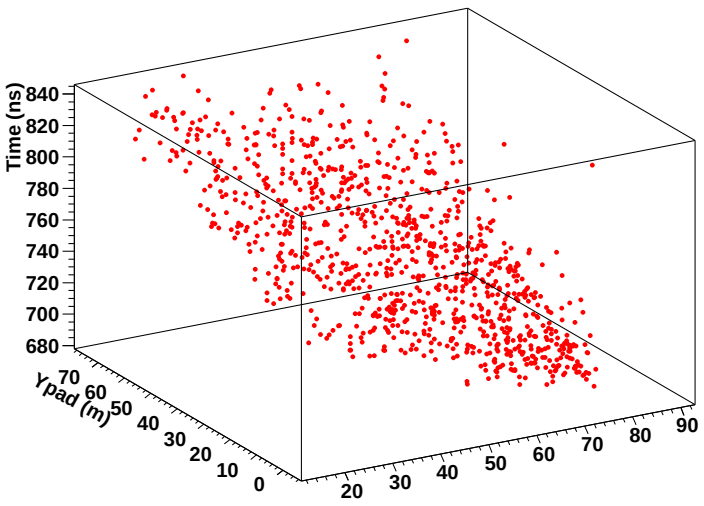

Figure 2.6: Space-time picture of a shower event.

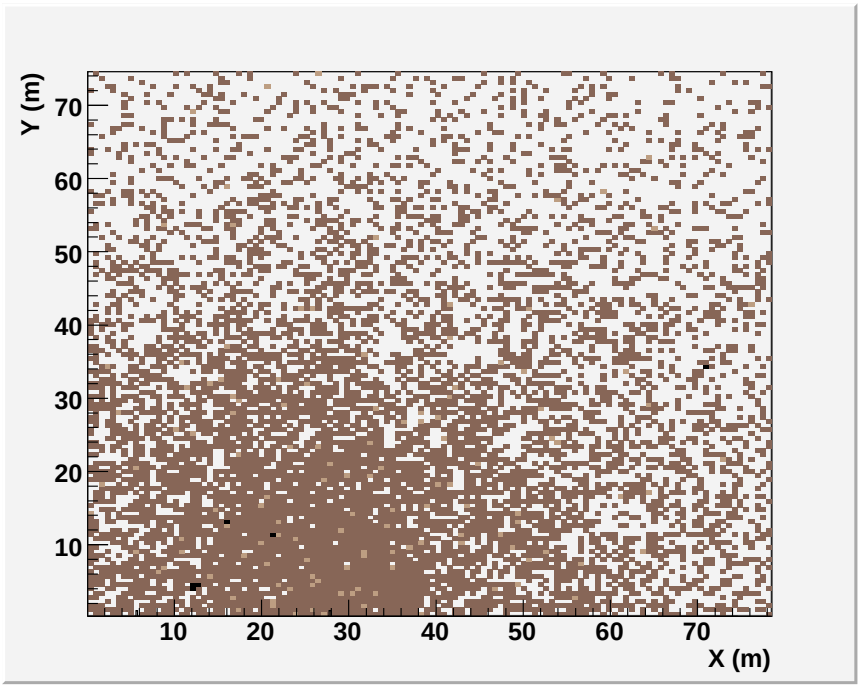

Figure 2.7: X-Y map of a large shower.

2.5 Event Reconstruction

The official code of ARGO-YBJ is MEDEA++. It reconstructs events for both real and MC data. The code language is C++ and it produces ROOT

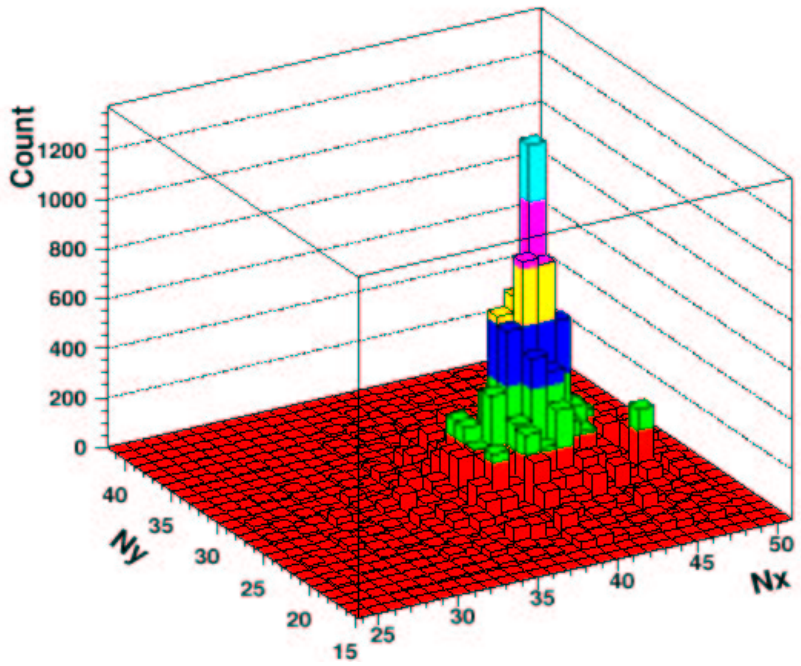

Figure 2.8: Charged density profile of one event as reconstructed by means of the analog read-out. The charge peak corresponds to about 3500 particles.

ntuples with main features of reconstructed events for higher level analyses: on-line monitoring, sky maps, full reconstruction (core reconstruction and arrival direction reconstruction of the primary) available to perform all kind of analysis for ARGO-YBJ. Actually Medea++ goes through three levels of reconstruction. The first level, RecLevel0, is applied only to true data in order to decode the DAQ input file and to convert the event format to be elaborated in the next reconstruction level. Monte Carlo data do not need the decoding procedure, therefore the reconstruction of this kind of events begins from RecLevel1. RecLevel1 essentially connects each hit to the associated PAD. Thus from a hit, the corresponding element can be accessed and for each detector element the corresponding hits can be retrieved. Moreover RecLevel1 rejects the hits that are in detector elements which are not active or not properly working and sorts the hits according to the time. The event reconstruction is essentially performed in RecLevel2 and is developed in tre steps:

- noise filter
- Core reconstruction

- Direction reconstruction

The noise filter simply selects within the 2μs event window a subwindow (default 400 ns) whose multiplicity is maximal. This allows to further reject noise hits, e.g. the hits which are believed to be background or instrumental noise. Then all the hits selected by the Noise Filter are fitted according to a plane. After the core position is estimated a conical fit is performed to the hits.

2.6 Shower Core reconstruction

Different alghoritms have been investigates to reconstruct the shower core position [27], but the most performant is the Maximum Likelihood Method. The algorithm uses the theoretical information about the shape of charged particles distribution. The widely used Nishima-Kamata-Greisen (NKG) function is an approximate analytical solution of the cascade equations and provides a prediction about the expected density distribution. In the ARGO-YBJ code the NKG function has been modified on the basis of some simulation and optimized for showers initiated by photons. The pattern of the event is $X = (\vec{r}_i, n_i)_{i=1,...N}$ where n_i and $\vec{r}_i$ are the number of particles on and the position of the i-th pixel, respectively. N is the number of pixels. The likelihood function $LF(X \mid \eta, \vec{r}_c)$ depends on the shower size η and on the shower core position $\vec{r}_c = (x_c, y_c)$. The core reconstruction consists in search for the values of (x_c, y_c) which make maximum the likelihood. The probability of observing m particles in a pixel whose distance from the core is $R = \mid \vec{r} - \vec{r}_c \mid$ can be written as:

$$p(m) = \frac{\mu^m}{m!}\, e^{-\mu} \tag{2.1}$$

where $\mu = \rho(R)$ is the expected average number of particles according to the NKG-like function. The detector area is divided in a grid of N_S active pixels of equal area. Typically the module (3 RPC chambers of area $S \sim 11.6\ m^2$) is used as pixel and $N_S = 520$ for 130 CLUSTERS. The value of N_S can be lower if some cluster is excluded from the data-taking. The likelihood function becomes

$$LF2 = \prod_{k=1}^{N_S} p(m_k) \tag{2.2}$$

where the number of particles m_k on the k-th module is the number of fired strips on that module. The corresponding log-likelihood function is,

therefore:

$$LLF2 = \ln S \sum_{k=1}^{N_S} m_k + \sum_{k=1}^{N_S} m_k \ln \rho(R_k) - S \sum_{k=1}^{N_S} \rho(R_k) - \sum_{k=1}^{N_S} \ln(m_k!) \quad (2.3)$$

We observe that

$$\sum_{k=1}^{N_S} m_k = N_{strip}$$

that is the total number of fired strips on the entire array. Requiring

$$\frac{\partial(LLF2)}{\partial \eta} = 0$$

the shower size results

$$\eta = \frac{N_{strip}}{S \sum_{k=1}^{N_S} \rho(R_k)}$$

The problem reduces to the minimization of the likelihood with respect to two variables (x_c,y_c) and the two steps minimization approximation is not necessary. A single numerical minimization has been used.

2.7 Arrival Direction reconstruction: planar or conical fit

Three different alghorithms have been implemented in Medea++ to determine the direction of the showers and the detector angular resolution [28]. The usual method is performing χ^2 fit to the recorded arrival times t_i by minimization of the quantity:

$$\chi^2 = \sum_i (f - t_i)^2 \quad (2.4)$$

where the sum includes all PADs with a time signal. This quantity is not properly a standard χ^2 because the sum quantity are not divided by the time uncertainty. Usually the function f describes a plane, a cone with a fixed cone slope or a plane with curvature corrections. The fit parameters are a time offset and the two direction cosines. This represents in general terms the usual fitting procedure. Improvement to this scheme can be achieved by excluding from the analysis the time values belonging to the non-gaussian tails of the arrival time distribution by performing some successfull χ^2 minimizations for each shower.

2.7.1 Planar fit

The simplest algorithm for the reconstruction of the direction of the incoming primary particle is the planar fit. This algorithm assumes that the front of the incoming particles forming the EAS can be parameterized by a plane. The fit to the arrival times of the EAS particles is accomplished by minimizing the following expression χ^2:

$$\chi^2 = \sum_i ((t_i - t_0) - \frac{x_i}{c} l - \frac{y_i}{c} m)^2 \tag{2.5}$$

whre t_i is the time measured by the i-th PAD, x_i and y_i are the coordinates of this PAD, l and m are the director cosines of the planar surface and t_0 the arrival time in the point of coordinates (0,0). The minimization is repeated some times. After the first fit, all the hits with more than 50 ns of deviation from the reconstructed shower front are rejected. In the following iterations the RMS of the residuals of the previous fit (σ_{res}) is calculated. Then all the hits with a deviation larger that Nσ_{res} are rejected. The value of N is tunable, typically $N = 5$. Moreover, the reconstructed direction at step n is compared with the reconstructed direction at step (n-1). If the two directions differe less than P degrees (where P is another tunable parameter) then the minimization procedure ends and the last reconstructed shower front is assumed as that giving the best estimate of the direction of the primary cosmic ray. The main advantage of this algorithm is that the χ^2 minimization has an analytical solution. Therefore, the algorithm is very fast and it can be applied to all showers without any pre-requisite. The main disadvantage is that the EAS front is not planar, but is better approximated by a cone.

2.7.2 Conical Fit

A better estimation of the shower direction is instead reached with a conical parameterization of the shower front. The fit is made by minimizing the following quantity:

$$\chi^2 = \sum_i ((t_i - t_0) - \frac{x_i}{c} l - \frac{y_i}{c} m - \frac{R_i}{c} \alpha)^2 \tag{2.6}$$

on the plane perpendicular to the shower direction. The α parameter is the cone slope that can be a free parameter of the fit or can be fixed to a Monte-Carlo derived value ($\alpha = 0.03$); R_i is the distance of the PAD from the shower axis. The main disadvantage is that the minimization of the χ^2 function can not be analytically solved. On the contrary, Eq. 2.6 can be

analytically minimized if one assumes that R_i is a fixed quantity. An iterative procedure is used in which R_i is calculated using the direction reconstructed in the previous step. In the first step, as starting direction, the direction calculated with the planar fit algorithm described in section 2.7.1 is used.

2.8 Detector monitoring and data analysis

One of the major problems in experiments producing a very large amount of data like ARGO-YBJ is to have fast efficient tools to check their quality and select them for a given analysis. ARGO-YBJ is starting to accumulate around 200 TB of data each year. The data taking unit is the run, indicating a time window during which data taking conditions remained stable: raw data files are currently at most 1 GB in size. ARGO-YBJ collaboration has performed the data quality check in different steps:

- online monitoring of the detector operation [29].
  The Detector Control System (DCS) has been designed to monitor the following quantities:
  - the gap currents for each RPC, the voltage powering the RPC front-end electronics and receiver boards, the local temperature and the barometric presuure in the experimental hall: these parameters are sampled every few seconds.;
  - the applied voltage and the absorption current in every high-voltage channel;
  - the gas pressure for the Argon line and the bottle weights for the liquid gas bottles.

Fig. 2.9 and Fig. 2.10 show the daily trends of two enviromental parameters (pressure and temperature). These trends are crucial for many analyses and detector check. For instance they permit to correlate the RPC gap current with the local temperature, and with the barometric pressure.

- online monitoring looking at detector performances [30], (number of hit for each PAD and for each CLUSTER, TDC distribution for each CLUSTER). This monitoring allows to check the proper operation of all parts of the detector.

- offline analysis of the detector operation and data consistency looking at: not-reconstructed quantities like the trigger rate, PAD and CLUSTER occupancy; and reconstructed variables like azimuth and zenith distribution, χ^2 from the planar and conical fit,etc., etc.

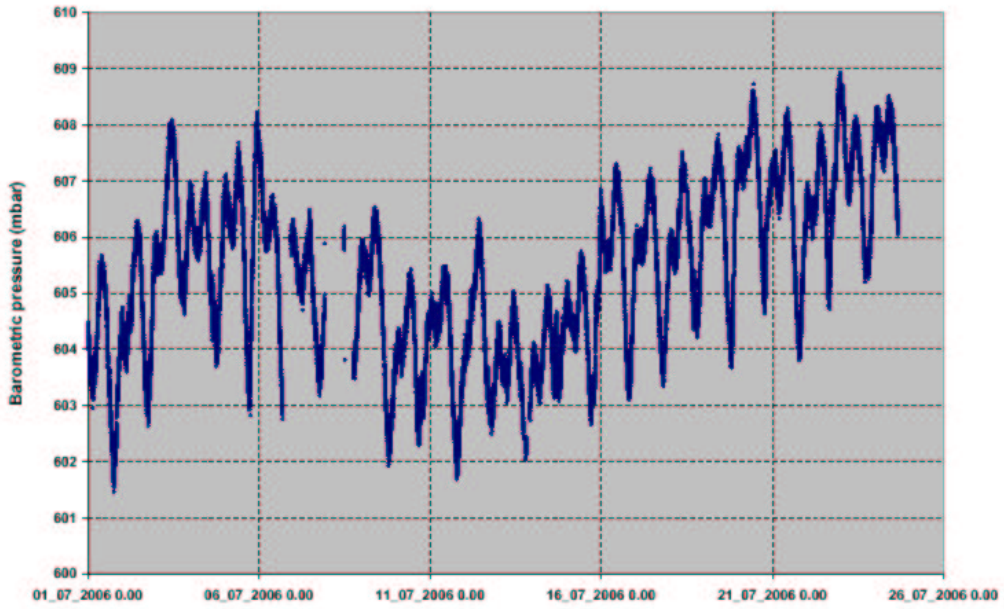

Figure 2.9: Barometric pressure (mbar). The data have been collected in July 2006.

The monitoring of the reconstructed variables is very powerful to check the quality of the data-taking. Mean values of direction cosines close to zero, uniform azimuthal distribution, stable mean value of the shower fit χ^2 indicate good data with proper timing calibration. As an example, a subtle problem in the DAQ was fixed thanks to the anomaly in the trend of the planar fit χ^2. The mean number of fired clusters and the mean number of hits were stable in the events collected during the day January 9, 2005 (see Fig. 2.11) but the χ^2 profile was not stable. This anomalous trend was due to a DAQ-misalignment for CLUSTER 135 and 67. The hits of these clusters were wrongly collected in the previous event. Fig. 2.12 shows the residuals from planar fit in two different periods (red markers: DAQ for cluster 135 is right, blue markers: DAQ for cluster 135 is wrong). For clusters 134 and 136 the DAQ is right and the residual are stable. Fig. 2.13 and Fig. 2.14 clarify the DAQ problem: CLUSTER 135 is missing in the event 1512345 and its hits are wrongly collected in the event 1512344.

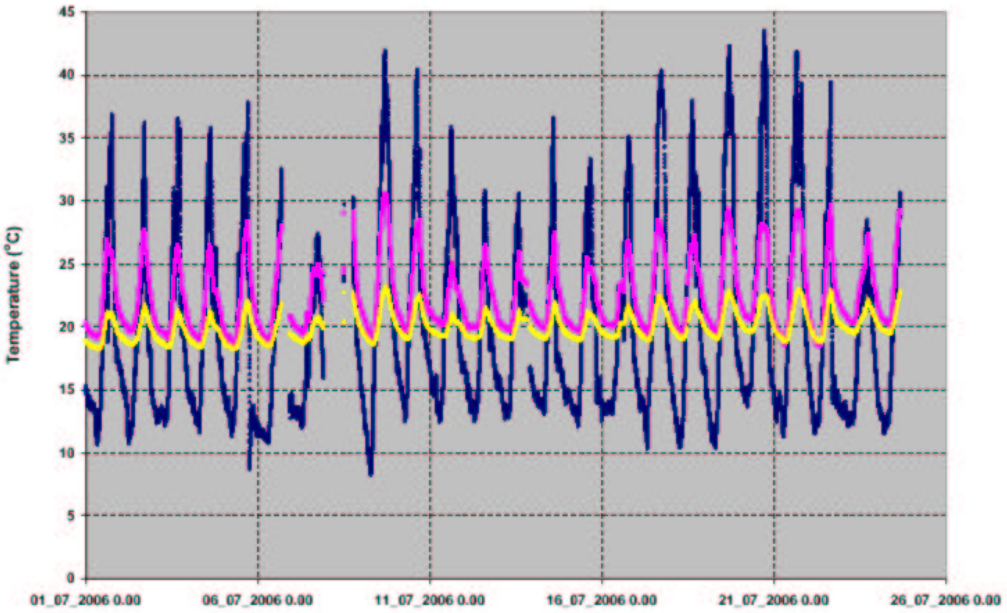

Figure 2.10: Temperature vs time: external (blue curve), inside the laboratory (purple curve) and measured close to the chambers (yellow curve). The data have been collected in 26 days in July 2006.

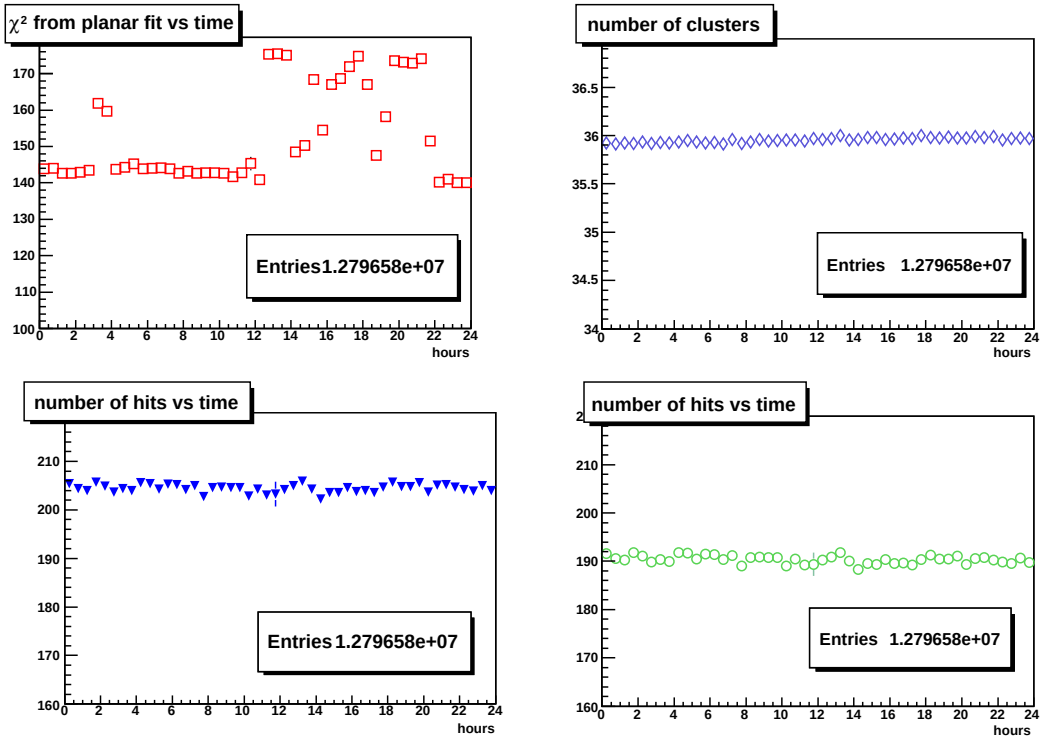

Figure 2.11: Profiles of different variables versus time: χ^2 from planar fit, number of fired clusters, number of all hits, number of hits used in the planar fit.

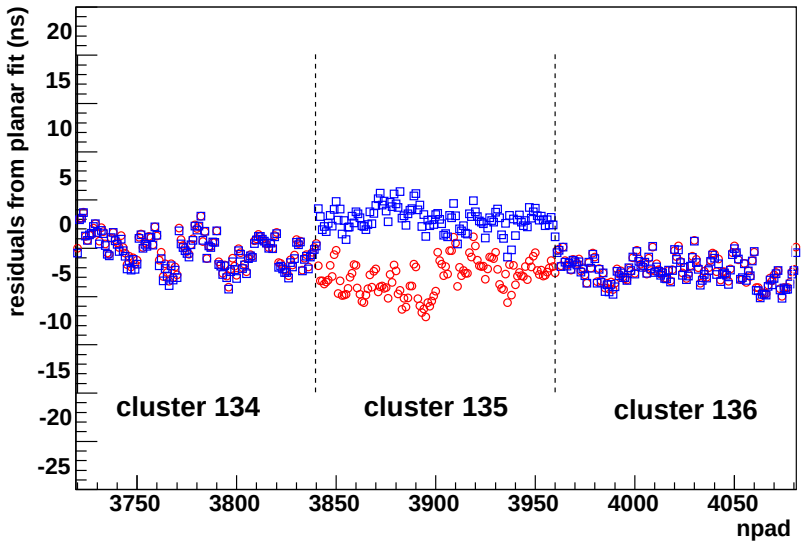

Figure 2.12: Residuals from planar fit (without calibration) for the PADs of three CLUSTERs (134, 135, 136). Red markers: data collected without DAQ problem. Blue markers: the DAQ problem is there. More details in the text.

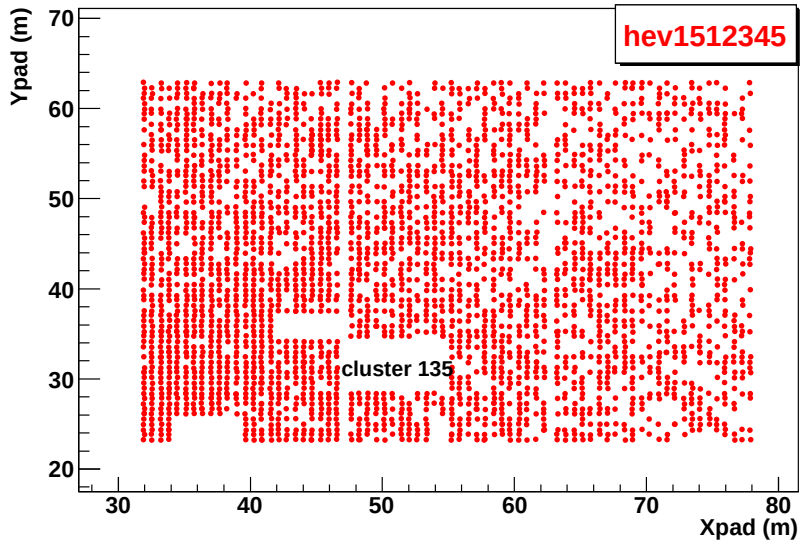

Figure 2.13: X-Y pattern of the event registered with the number 1512345. The hits of cluster 135 are missing. They are recorded in the previous event (1512344).

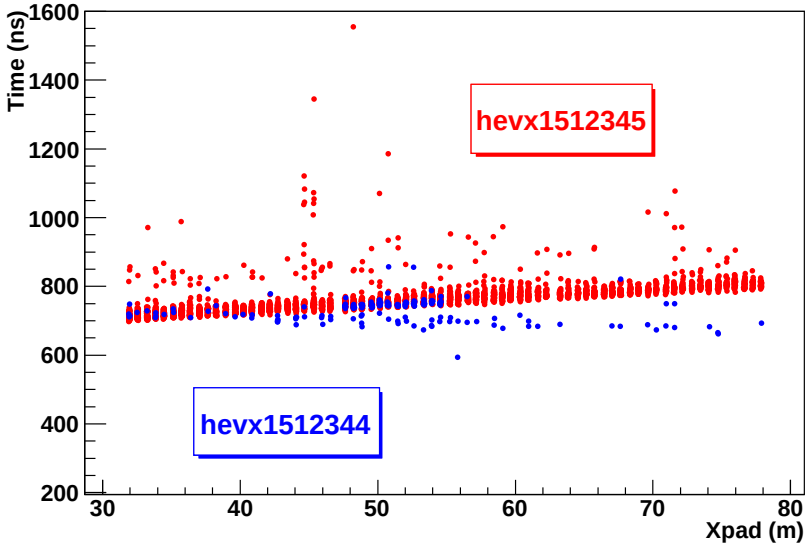

Figure 2.14: Time vs PAD x-coordinate for two events. Some hits (cluster 135) of event 1512345 have been recorded like hits of event 1512344.

3

Timing Calibration in EAS experiments

In Extensive Air Shower experiments, the primary direction is reconstructed by the space-time pattern of secondary particles. The time offsets are the systematic time differences between detector units (differences of the transit time of signals from different parts of the detector), which lead to worse angular resolution, and more seriously, to wrong reconstruction of the primary direction. As a consequence the azimuthal distribution is deformed according to a quasi-sinusoidal modulation [38, 39]. Thus the correction of these systematic time offsets [32] is crucial for the primary direction reconstruction, much more when the EAS detector is devoted to gamma ray astronomy and the pointing accuracy is required in order to associate the signals with astrophysical sources. In this chapter an off-line calibration method is presented and studied by means of proper simulations. It allows to calibrate a shower array repeatedly just using the collected data without disturbing the standard acquisition. The originality of this calibration method is the definition of a Characteristic Plane introduced to analyze the effects of the time systematic offsets, such as the quasi-sinusoidal modulation on azimuth angle distribution. This calibration procedure works also when a pre-modulation on the primary azimuthal distribution is expected, for instance due to the geomagnetic field [33]. The correctness of this calibration method has been checked by means of simple simulations both in the case of uniform and modulated azimuthal distribution. The procedure has been also applied to the ARGO-YBJ detector (see Chap. 4).

3.1 Angular resolution and pointing accuracy in EAS experiments

The accuracy in the reconstruction of the shower arrival direction mainly depends on the accuracy in the measurement of the relative arrival times of the shower particles by means of the timing pixels of the detector. In γ-ray astronomy a good angular resolution (measurement of the arrival direction) not only allows for a precise source localization, but is an essential requirement to achieve higher sensitivity since it determines the size of the angular bin opened around the source (or the binning in the sky map in the case of blind search), and, in turn, the amount of background. A point source is inferred from an excess of showers arriving from a particular direction of the celestial sphere. Because of the finite instrumental resolution, showers from a point source appear to arrive from a finite region of the sky and are therefore accompanied by a background of nearly isotropic cosmic rays. An accurate determination of both signal and background from a particular direction therefore requires a good understanding of the angular resolution of the detector. Indeed, the better the angular resolution, the smaller the required search region around a possible source, and thus the lower the background. For a point source, the signal/background ratio is larger when the square of the angular resolution is smaller. As a consequence it is important to verify that the apparatus is operating with the estimated angular resolution, and that no significant systematic "pointing errors" are present. An alternative source in order to calibrate the detector performance in the event reconstruction is the Moon (see [34]). The Moon has an angular radius $R_{moon} = 0.26°$, it must cast a shadow in the high-energy cosmic ray flux (*shadow of the Moon*). The shadowing of cosmic rays from the direction of the Moon, is therefore useful in measuring the angular resolution of an array. Besides detecting the Moon position in the sky allows to determine the absolute orientation of the detector. In fact observing the expected depth of shadowing verifies the array pointing accuracy and stability. In principle, the size of the deficit gives information about the angular resolution while the position of the dip provides information about the pointing error. The results of angular resolution and pointing absolute after calibration will be shown in Chap. 5.

3.2 Calibration procedure

In EAS experiments,for an event i the time t_{ij} can be measured on each fired detector unit j, whose position $(x_j,\ y_j)$ is well known. The primary

direction cosines $l_i = \sin\theta_i \cos\phi_i$, $m_i = \sin\theta_i \sin\phi_i$ (θ_i and ϕ_i are zenith and azimuth angles) are reconstructed by a least squares fit. Taking into account the time offset Δ_j typical of the detector unit and assuming that the shower front is plane and the time-spread due to its thickness is negligible, the plane-equation is

$$c(t_{ij} - \Delta_j - t_{0i}) = l_i x_j + m_i y_j \tag{3.1}$$

where c is the light velocity, and t_{0i} is another parameter of the fit. But the time offset Δ_j is unknown and the goal of the calibration is just to determine it. Usually the times are corrected to reduce the residuals with respect to the planar fit of the showers (*Residual correction*) but this does not guarantee the removal of the complete offset. Therefore one can assume that the time offset Δ_j is the sum of two terms: the residual term δ_j^{res} and another unknown term.

3.2.1 Simulation and Residual Correction

A traditional off-line calibration method is based on the study of the time-residuals e.g. the differences between time estimated by means of the planar fit of the shower and the time measured by the detector unit. The effects of the timing inaccurancies were studied first using a fast geometrical simulation. The calibration method has been checked introducing different time-offsets for each detector unit and looking for the capability of the method to remove these offsets. Random zenith (θ) and azimuth (ϕ) angles were extracted according to a flat distribution of the azimuth angle and according to the zenith distribution:

$$\frac{dN}{d\theta} \propto \sin\theta \cos^n\theta \tag{3.2}$$

typical of the air shower arrival directions, where n has been chosen equal to 7.725. The primary directions were reconstructed by a toy-array of 72×70 detector units. The times for 5040 units were calculated according to the shower front and then shifted by offsets introduced ad-hoc (each unit with its offset, first plot of Fig. 3.1).

Then a planar front is reconstructed by means of the χ^2 minimization. The mean values of the residuals after the planar reconstruction are, as expected, coherent (not equal to) with the offsets of each unit. Thus the *Residual correction* is given by the residuals due to the given offsets. It is not expected that the *Residual correction* removes completely the introduced offsets. In the second plot of Fig. 3.1 the new offsets are in the range $-0.01 \div 0.07$ ns, close to zero, but a further systematical correction is necessary in order to remove completely the offsets.

3.3 Characteristic Plane Definition

After the estimate of δ_j^{res} by means of *Residual correction*, the plane-equation goes like:

$$c\left(t_{ij} - \delta_j^{res} - t'_{0i}\right) = l'_i x_j + m'_i y_j \tag{3.3}$$

giving the fake direction cosines $l'_i = \sin\theta'_i \cos\phi'_i$, $m'_i = \sin\theta'_i \sin\phi'_i$. From Eq.s 3.1 and 3.3 it results:

$$\Delta_j = a_i \frac{x_j}{c} + b_i \frac{y_j}{c} + \delta_{0i} + \delta_j^{res} \tag{3.4}$$

where $a_i = l'_i - l_i$, $b_i = m'_i - m_i$, and $\delta_{0i} = t'_{0i} - t_{0i}$. This last term is an irrelevant time-shift equal for all the units. Neglecting the residuals one can conclude that the offset Δ_j is correlated with the position of the detector unit. This result is coherent with the result of the Residual correction (second plot of Fig. 3.1). The quantities a_i, b_i define a Characteristic Plane (CP) in the (x, y, Δ) space, depending only on the fired unit pattern, representing the difference between the reconstructed plane (FP: Fake Plane) and the real one (RP: Real Plane). Events firing different sets of units have different CPs, while events firing the same set of units have the same CP, that is the difference between the FP and RP is the same. We define the CP of an EAS array like the average difference between FPs and RPs, i.e. the systematic deviation between FP and RP (the pointing accuracy). The CP is fully determined by the direction cosines

$$a = \langle l' \rangle - \langle l \rangle = \sin\theta_0 \cos\phi_0, \qquad b = \langle m' \rangle - \langle m \rangle = \sin\theta_0 \sin\phi_0 \tag{3.5}$$

where the mean values are estimated on a large sample of events and θ_0, ϕ_0 are zenith and azimurh angles of the vector normal to the CP.

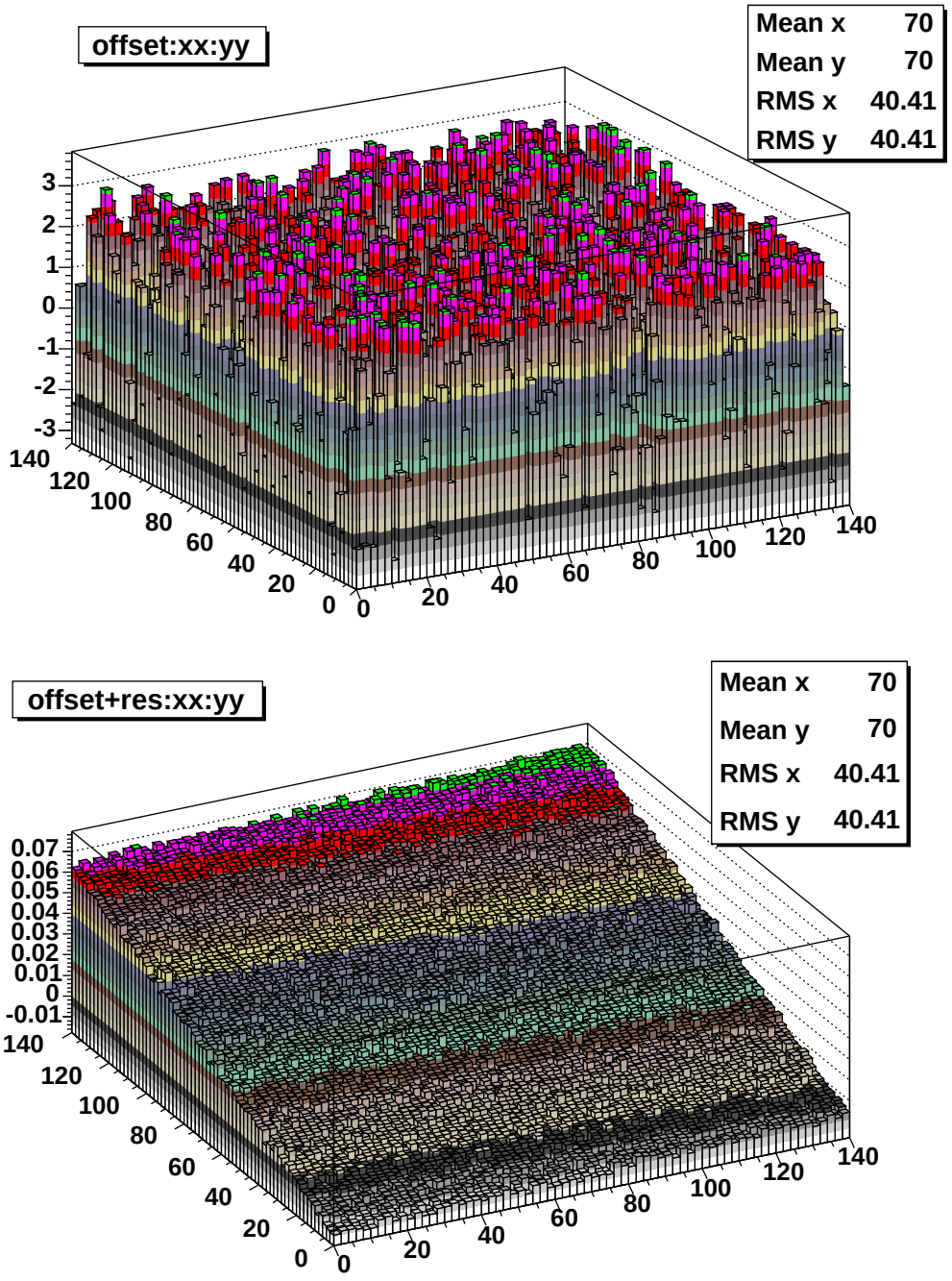

Figure 3.1: Geometrical simulation - The unit-offset versus the unit-position before (first plot) and after (second plot) the *Residual Correction*. Another correction is necessary in order to remove completely the time shifts.

3.3.1 Quasi-Sinusoidal Modulation

The primary azimuth angle can be described by a probability function (PDF) (see [37]) $f(\phi|\theta)$. The presence of the characteristic plane introduces a quasi-sinusoidal modulation of the reconstructed azimuth angle distribution :

$$f'(\phi'|\theta) = f(\phi|\theta)\left[1 + \frac{r}{\sqrt{1 - r^2\sin^2(\phi' - \phi_0)}}\cos(\phi' - \phi_0)\right] \tag{3.6}$$

where $r = \sin\theta_0/\sin\theta$. The PDF of the reconstructed azimuth angle is a combination of multi-harmonics of odd orders with the the amplitude approximately proportional to r^{2n+1} $(n = 0, 1, 2...)$ when $r << 1$. The time offset does not introduce even order modulations into the reconstructed azimuth angle distribution. When $f(\phi|\theta) = 1/2\pi$, the first harmonic becomes dominant and the PDF of the reconstructed azimuth angle goes as

$$f'(\phi'|\theta) = \frac{1}{2\pi}\left[1 + r\cos(\phi' - \phi_0)\right] \tag{3.7}$$

One can observe that the modulation parameters depend on the angles θ_0 and ϕ_0 connected to the CP (see Eq.s 3.5). The phase is just ϕ_0, while the amplitude is proportional to r. By integrating $f'(\phi'|\theta)$ over θ it results

$$f'(\phi') = \frac{1}{2\pi}\left[1 + \sin\theta_0\left\langle\frac{1}{\sin\theta}\right\rangle\cos(\phi' - \phi_0)\right] \tag{3.8}$$

A fast Monte Carlo simulation was done to check the above conclusion. The azimuth angle was sampled uniformly over $[0, 2\pi]$ and the zenith angle from a distribution modulated according to $sin\theta\cos^n\theta$ (the mode value is $\sim 22^\circ$ and $\langle 1/\sin\theta\rangle = 3.44$). CPs with different θ_0 and ϕ_0 were assumed, subtracting $\sin\theta_0\cos\phi_0$ and $\sin\theta_0\sin\phi_0$ from the original direction cosines, respectively, in order to get the new direction cosines. Fig. 3.2 shows the reconstructed azimuth distributions for two different CPs with $\theta_0 = 0.02\ rad$, $\phi_0 = 0.4\ rad$ and $\theta_0 = 0.20\ rad$, $\phi_0 = 1.2\ rad$, respectively. The first distribution is well reproduced by a best-fit function like that of the Eq. 3.8 as expected for small values of θ_0. Also the fit parameters are in agreement with the simulation parameters. The higher order harmonics must be taken into account in order to well reproduce the second distribution ($A2$ and $A3$ are the amplitudes of 2nd and 3rd harmonics) because in this case θ_0 and r are larger.

3.4 Characteristic Plane Correction

According to Eq. 3.1, if l_i and m_i were exactly known, then any event can be used to relatively calibrate all the detector units hit by that shower, while

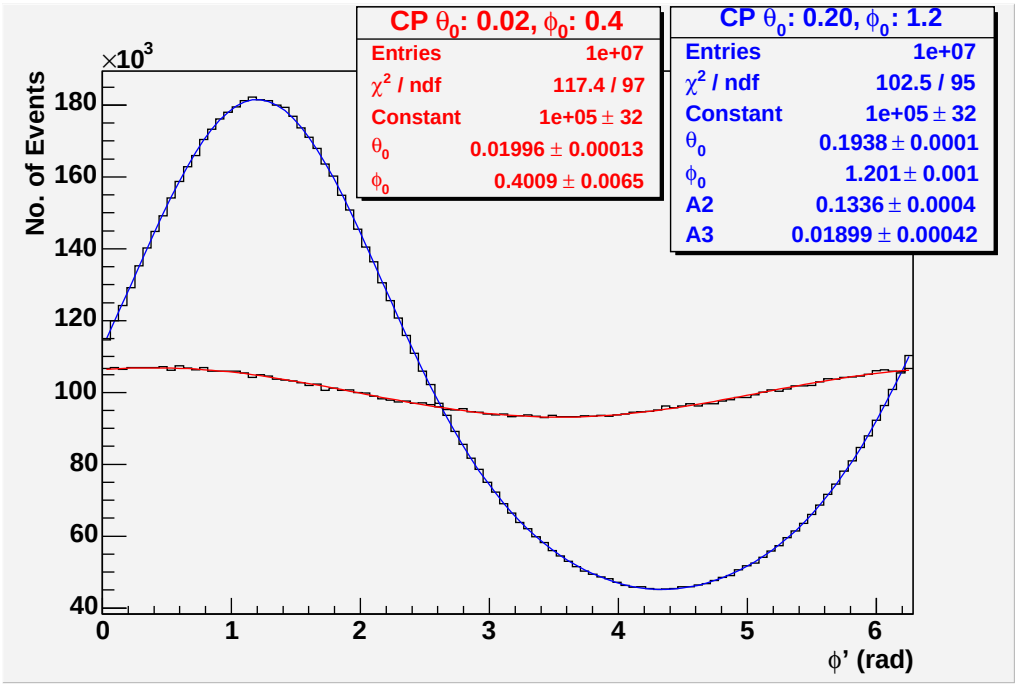

Figure 3.2: Azimuth angle distributions fitted with harmonic functions (see the text for comments).

$l'_i - a$ and $m'_i - b$ can be taken as unbiased estimate of l_i and m_i. Therefore the time correction is determined by a and b, i.e. the CP of the EAS array, according to Eq. 3.4.

Assuming that the primary azimuth angle is independent on the zenith angle and distributes uniformly, then $\langle l \rangle = 0$, $\langle m \rangle = 0$. Thus $a = \langle l' \rangle - \langle l \rangle = \langle l' \rangle$, $b = \langle m' \rangle - \langle m \rangle = \langle m' \rangle$, which means that the CP of an EAS array can be determined by the mean values of the reconstructed direction cosines. Then the time offsets can be calculated by means of the off-line analysis of the collected data.

3.4.1 CP method checks

One million of showers were extracted from the same distributions of θ and ϕ used in Sec. 3.3.1. The arrival primary directions were reconstructed by an array of detector units (10×10 units on a surface of 40×40 m^2). The times measured by each unit were shifted by systematic time offsets (first plot of Fig. 3.3). As a consequence the primary directions were reconstructed with respect to a CP with $a = 3.97 \times 10^{-3}$ and $b = 7.34 \times 10^{-3}$ (mean values of the

reconstructed direction cosines). From the Eq.s 3.5 it is trivial to estimate $\theta_0 = 8.3 \times 10^{-3}\ rad$ and $\phi_0 = 1.07\ rad$.

The reconstructed azimuth distribution is fitted according to Eq. 3.8 (see the first plot of Fig. 3.4). As expected the modulation coefficient $p1$ and the phase $p2$ are compatible with $\sin\theta_0 \langle 1/\sin\theta \rangle = 0.029$ and ϕ_0, respectively. The angles between reconstructed and "true" direction are shown in the first plot of Fig. 3.5.

The calibration based on the CP method allows to correct the time measurements, removing the effect of the time offset on each detector unit. In the second plot of Fig. 3.3 the offset-calibration differences are almost null and the RMS is lower than $2.3 \times 10^{-2}\ ns$. As an effect of the CP calibration the modulation disappears in the azimuth distribution (second plot of Fig. 3.4) and the reconstructed directions are very close to the "true" ones (see the second plot of Fig. 3.5). Then the validity of the CP method is fully confirmed.

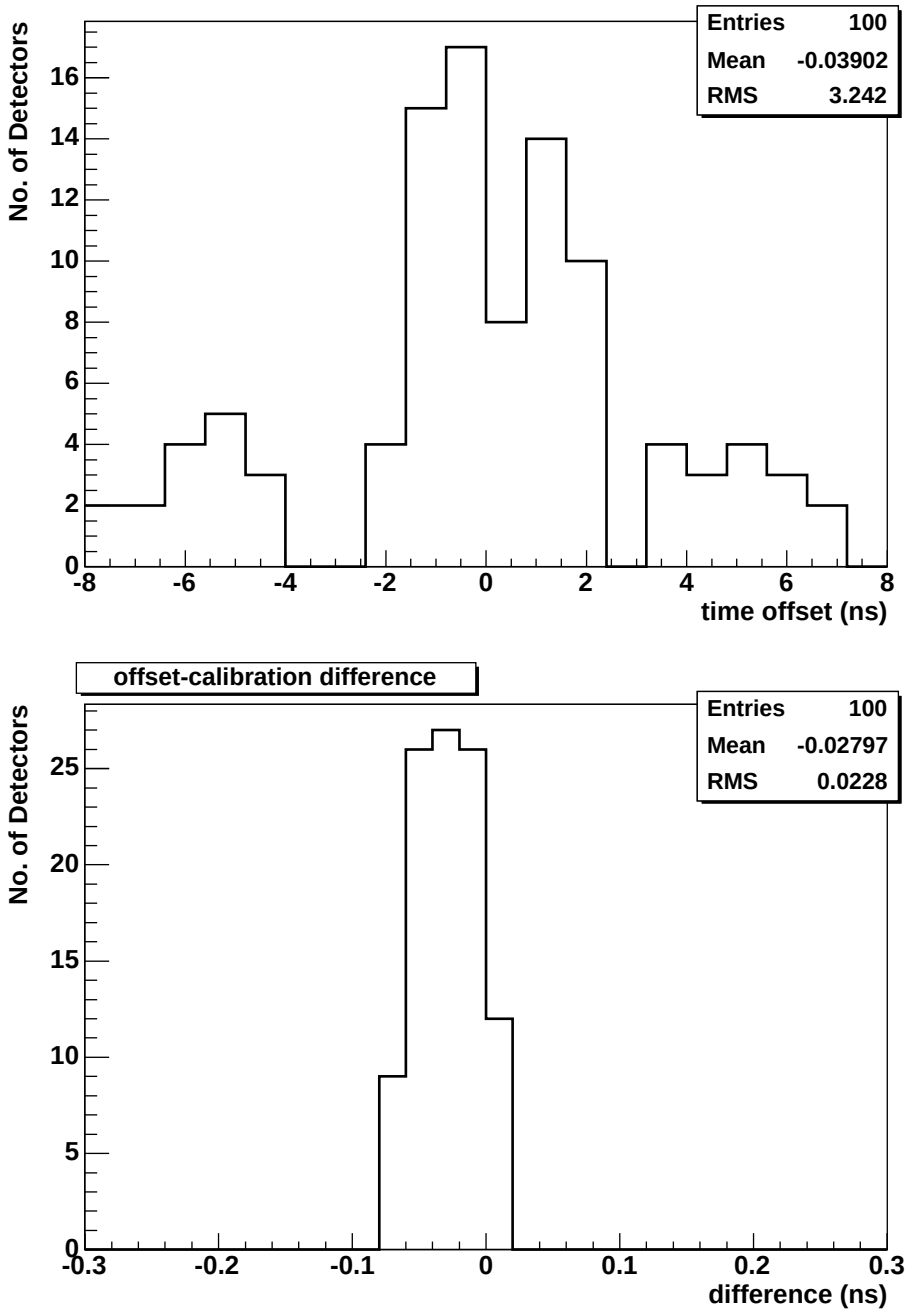

Figure 3.3: First plot: systematic time offsets introduced in the simulation of the time measurement. Second plot: differences between systematic offset and calibration correction.

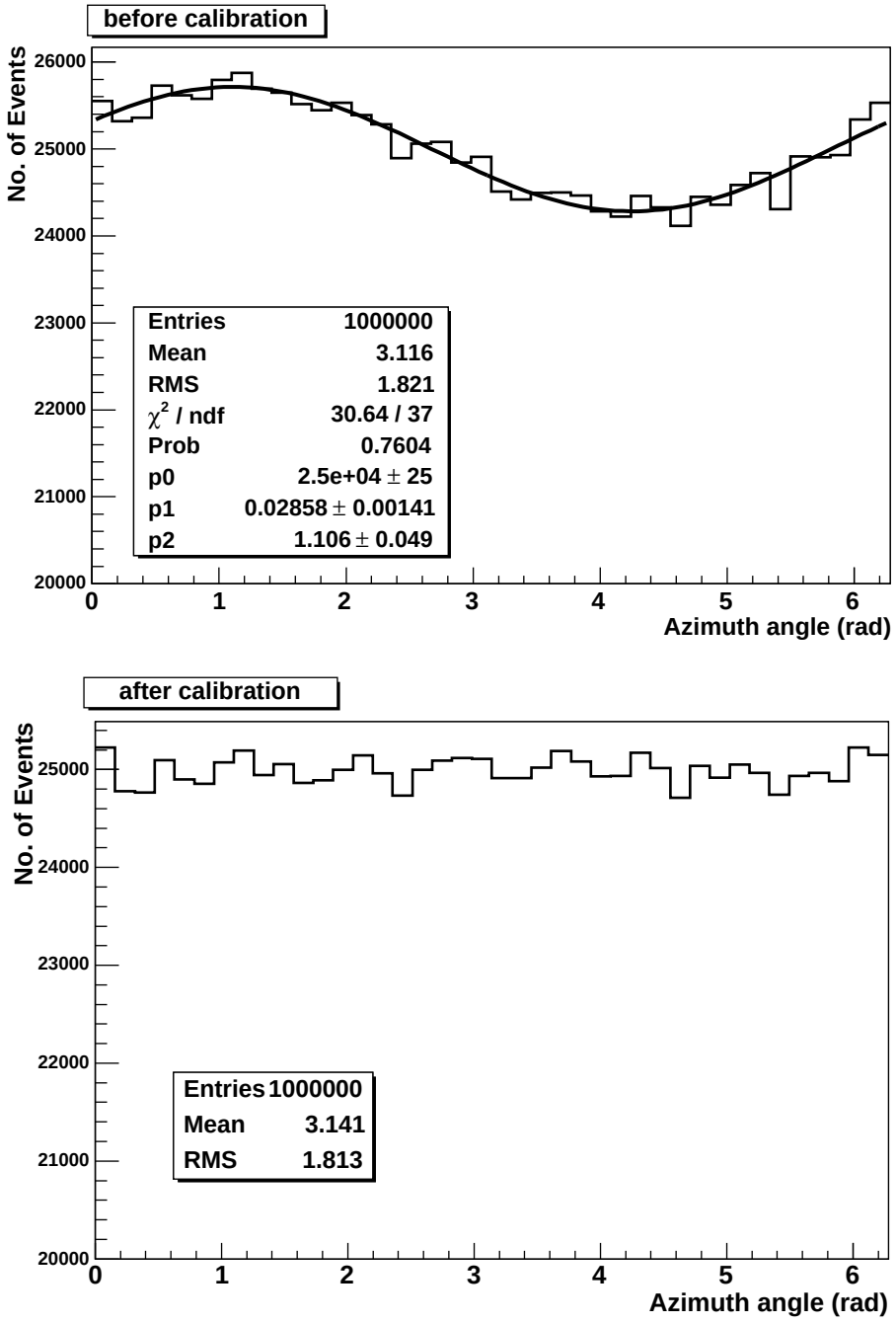

Figure 3.4: Azimuth distribution (first plot: before CP calibration, second plot: after CP calibration). In the first plot the sinusoidal fit is superimposed.

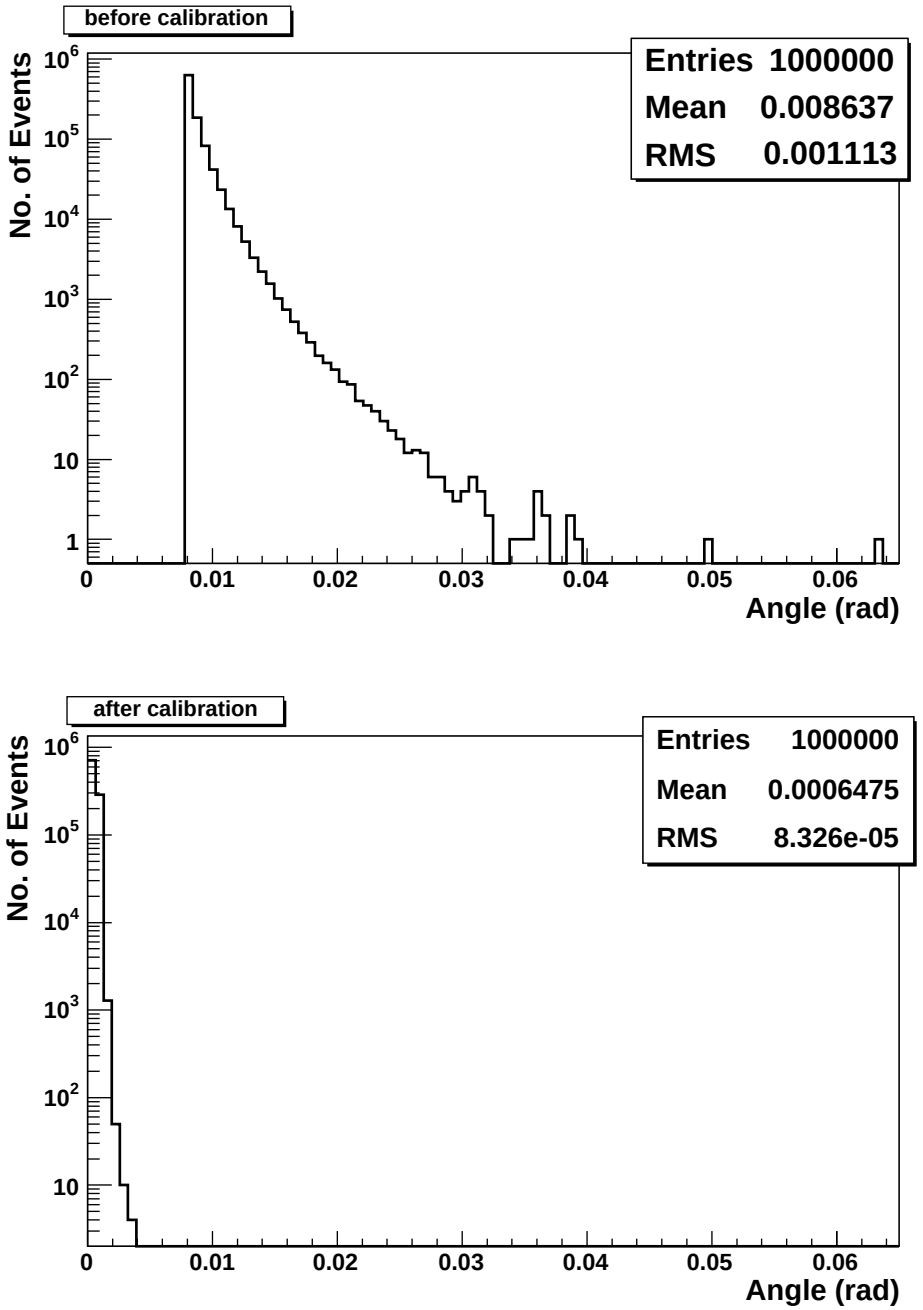

Figure 3.5: Angles between "true" and reconstructed directions (first plot: before CP calibration, second plot: after CP calibration).

3.4.2 Pre-modulation on the primary azimuth angle

The assumption for the CP method is that the mean values of the primary direction cosines are null. Generally this is not true for EAS experiments. The possible primary anisotropy, the detection efficiency depending on the azimuth angle, the geomagnetic effect, and so on, introduce pre-modulation into the azimuth angle distribution. Assuming that the ϕ-distribution is independent on θ, the pre-modulation can be described typically as:

$$f(\phi) = \frac{1}{2\pi}\left[1 + \sum_{n=1}^{\infty} g_n \cos(n\phi + \phi_n)\right]. \tag{3.9}$$

Only $g_1 \cos(\phi + \phi_1)$ contributes to the mean values of the primary direction cosines. Therefore they result

$$\langle l \rangle = +\frac{g_1}{2}\cos\phi_1 \langle \sin\theta \rangle, \qquad \langle m \rangle = -\frac{g_1}{2}\sin\phi_1 \langle \sin\theta \rangle. \tag{3.10}$$

The CP method annulls $\langle l \rangle$ and $\langle m \rangle$ leaving a sinusoidal modulation on the distribution of the new ϕ'' azimuth angle. When g_1 and g_2 are small enough and the higher order harmonics can be ignored (see Sec. 3.3.1) the distribution approximately is

$$f''(\phi'') = \frac{1}{2\pi}\left[1 + g_1' \cos(\phi'' + \phi_1) + g_2 \cos(2\phi'' + \phi_2)\right] \tag{3.11}$$

where

$$g_1' = g_1\left[1 - \frac{1}{2}\langle \sin\theta \rangle \left\langle \frac{1}{\sin\theta} \right\rangle\right]. \tag{3.12}$$

On the basis of this result one can conclude that the calibration with the CP method does not remove completely the pre-modulation on the primary azimuthal distribution. The g_1, g_2 amplitudes and the ϕ_1, ϕ_2 phases can be determined from the reconstructed azimuth angle distribution according to Eq.s 3.11 and 3.12. Then the direction cosines of the real CP can be determined by subtracting the pre-modulation term (Eq.s 3.10).

Fast simulations have been used also to check the calibration method in the case of pre-modulation with one and two harmonics ($g_1 = 0.05$, $\phi_1 = 0.3\ rad$ and $g_2 = 0.02$, $\phi_2 = 1.2\ rad$). The results are very similar to those of Sec. 3.4.1 confirming that the method works also when a pre-modulation is present. In Fig. 3.6 the "true" azimuthal distribution and the distribution after the first step of the calibration are shown. As expected the second distribution is well reproduced by Eq.s 3.11 and 3.12.

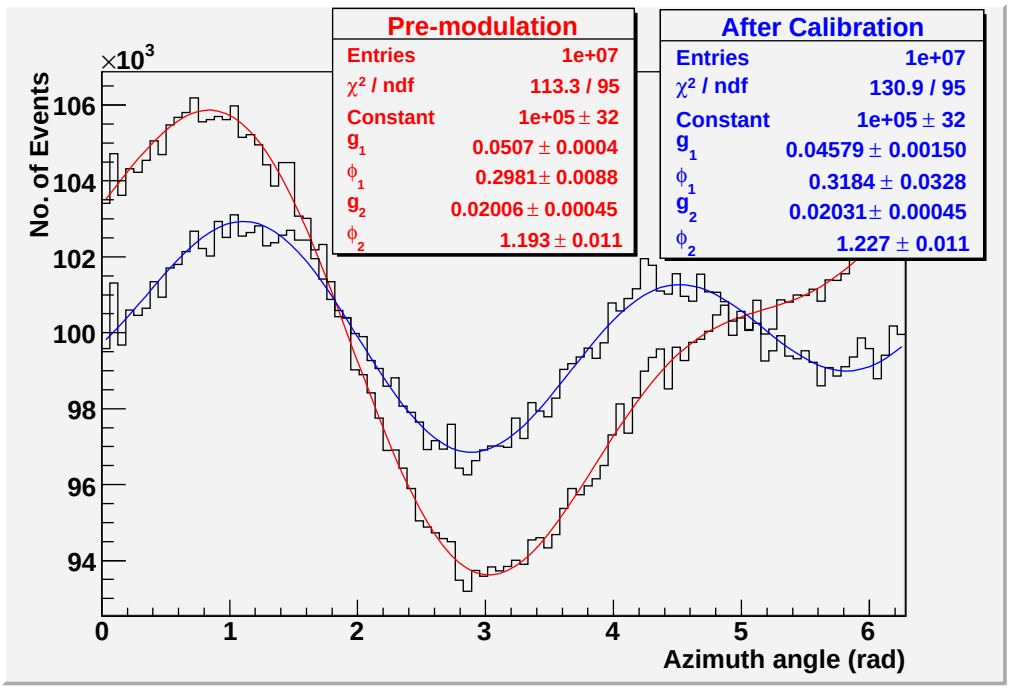

Figure 3.6: The pre-modulation "true" azimuth angle distribution is fitted by the function $f(\phi) = k\,[1 + g_1\ \cos(\phi + \phi_1) + g_2\ \cos(2\phi + \phi_2)]$. The after-calibration azimuthal distribution is fitted according to Eq.s 3.11 and 3.12. The fit-parameter values are in full agreement.

3.4.3 Geomagnetic Effect

The geomagnetic field inflects the charged primaries and leads to the well known East-West effect (with the modulation period of π which does not modify the mean values of the reconstructed direction cosines and does not invalidate the CP method), while the secondary charged particles of EAS are separated in the geomagnetic field with the lateral distribution getting wider and flatter, thus affecting the detection efficiency [33]. A non-vertical geomagnetic field destroys the uniformity of the detection efficiency along the azimuth angle which will further leads to quasi-sinusoidal modulation on the azimuth angle distribution [35]. The geomagnetic effect on the secondaries is typically the most significant pre-modulation (as described in Sec. 3.4.2) with amplitude of the order of few percent and very slight variations with the zenith angle. This is just the case discussed in the above section and the modulation can be determined according to Eq. 3.11, after which the time can be off-line calibrated using the CP method.

3.5 Geometrical simulation: TDC distribution

We investigated the shape of the times measured by the units of a detector array as a function of unit position. A one-dimensional array of 100 units was taken into account and one million of showers was extracted from the usual zenith distribution. Because the array is one-dimensional, the azimuth angle is replaced by left and right directions. In a first step, planar showers are simulated (50% from left, 50% from right). The measured times are registered for each unit. The mean TDC values versus unit position are shown in Fig. 3.7 (red profile of first plot). The profile is flat in the middle, with a small rising on the edges of the array. This profile does not reproduce the real TDC distribution. Different result by simulating conical showers: red curve, second plot in Fig. 3.7. The measured time profile shows a concave shape centered in the array, without flat regions. This result is due to the different detection efficiency (see Fig. 3.8): early particles require a smaller detection area

$$\frac{S_0}{\cos(\theta - \alpha)}$$

with respect to the larger area

$$\frac{S_0}{\cos(\theta + \alpha)}$$

for last particles.

The geometrical simulation has been performed also in the case of left-right asymmetry in the flux (blue shapes) in order to understand the effect of the geomagnetic field on the TDC map. The shapes are strechted according to the asymmetry: the mean times are higher where the flux is higher. We verified also, with the same simple simulation, that the times distributions of the single detector unit are larger on the edge and more narrow in the middle of the array.

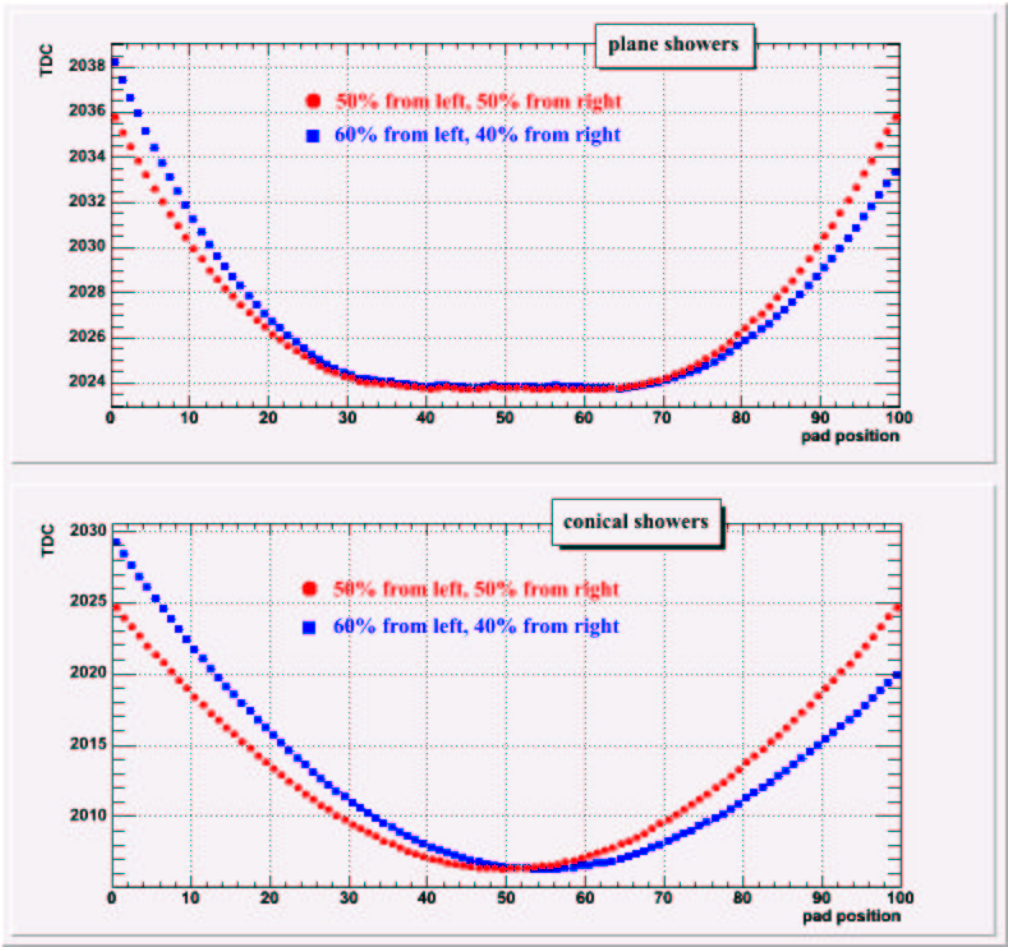

Figure 3.7: One-dimensional geometrical Simulation: time distributions vs detector-unit position. First plot for planar showers, second plot for conical showers. Red curves are due to a symmetrical flux from left and from right, blue curves when the flux from left is 60% and that from right is 40%.

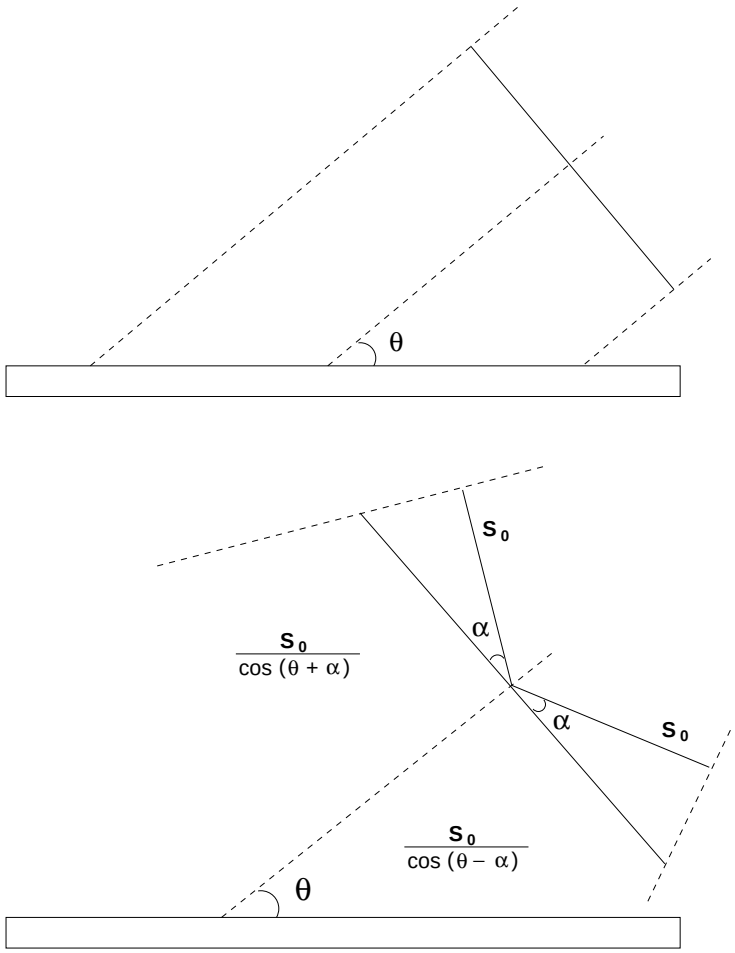

Figure 3.8: Sketch of the one-dimensional array used in the fast simulation. First:planar shower. Second: conical shower (the detection of the early particles is more efficient than that of the last particles).

4

Offline Timing Calibration for ARGO-YBJ detector

A hard work has been performed to calibrate in time the ARGO-YBJ detector. Usually in EAS experiments, the space-time information of the secondary particles is used to reconstruct the primary direction, which is greatly affected by possible time offsets. A hardware calibration is generally used and also for Argo-YBJ experiment it has been performed for a small portion of the detector (300 PADs). Due to the large of number of PADS the hardware calibration was unpratical: it takes time and man power and it must be repeated in different enviroment conditions. Moreover an electronic calibration by means of a proper signal is possible from the Local Station to the Central Station, but not from the PAD to the Local Station. Therefore planning, implementing and testing an off-line calibration was one of the major issue of ARGO-YBJ collaboration. The offline calibration has been implemented during the year 2004 when six CLUSTERs (ARGO-6) were in operation. Then it has been widely tested using data of ARGO-42 (42 CLUSTERs operating during the year 2005). The study of the calibration procedure allowed to understand deeply some systematics surviving in the procedure and introduce a new method named Characteristic Plane (CP) widely described in Chapter 3. The calibration procedure works using the run data collected without disturbing data acquisition. It has been performed using planar fit but a further improvement has been reached using conical fit to reconstruct the shower front. The validity of the procedure has been checked perfoming a dedicate MC and the application of CP correction with conical fit will be presented for ARGO-130 (130 CLUSTERS) in this Chapter too. Moreover a comparison with manual calibration for 300 PADs has been done pointing out a good agreement between manual and offline calibration. Here also an estimate of geomagnetic effect will be presented with a complete

simulation with 42 CLUSTERS.

4.1 Calibration Procedure

The calibration procedure has been implemented during the year 2005 using data collected at very beginning of May 2004.It has been implemented using Medea++ code and reconstructing the showers by a planar fit.The runs have been chosen in order to have a stable data taking. Here the results for ARGO-42 are presented. The used data sample is reported in Table 4.1. The time corrections are applied by means of an external ASCII file read by Medea++ by means of a CONFIGURATION FILE $UserConfiguration.input$. The other variables in this file are shown in Table. 4.2. The timing correction of 5040 PADs (Fig. 4.1) has been performed in three steps: the times are firstly corrected to reduce the residuals with respect to the planar fit of the showers (*Residual correction*, repeated twice) and then an additive correction has been applied to remove the systematical time-shift surviving after *Residual correction*. This is completely equivalent to performing the CP correction widely described in Chapter 3. Thus the full calibration correction for PAD results

$$\Delta_j = \delta_j^{res} + \langle l_i' \rangle \frac{x_j}{c} + \langle m_i' \rangle \frac{y_j}{c} \tag{4.1}$$

equal to (3.4) where the term δ_0 is omitted because it is an offset common to all PADs. The PAD positions (x_j,y_j) are well known. To calibrate the array we need the *Residual correction* for each PAD and the mean values of the direction cosines. The residuals are plotted for some PAD in Fig. 4.2. In order to determine the peak position, a Gaussian fit is applied in the range ± 10 ns around the bin with maximum number of entries. In each bin 200 entries have been removed in order to avoid bias due to off-shower hits. In the following with the term residual we will indicate the mean of the Gaussian curve. The residuals before the calibration are shown in Fig. 4.3 for all PADs of 42 CLUSTERs.

Calibration data set (LM 60):
test-5949-20050091311.000 .001 .002 .003 .004 .005
test-5951-20050091554.000
test-5954-20050091614.000
test-5956-20050091619.000
test-5958-20050091637.000
test-5959-20050091654.000 .001
test-5960-20050091734.000 .001
test-5961-20050091814.000
test-5962-20050091845.000
test-5963-20050091920.000
test-5964-20050091932.000 .001 .002 .003
test-5966-20050092108.000 .001 .002
test-5967-20050092228.000 .001 .002 .003 .004
Check data set (LM 120) :
test-0071-20050530340.000 .001 .002
Check data set (LM 60) :
test-0079-20050530738.000 .001

Table 4.1: List of the runs used for ARGO-42 calibration. The time of the run is used to define the name of the file. Different files have been used to check the calibration results, with two trigger conditions (LM 120, LM 60).

int FitMinSize = 20	Minimum shower size for direction reconstruction
int FitMaxIter = 30	Maximum number of iteration in direction reconstruction
double FitSigmaCut = 3.0	Maximum distance of the hit from the shower front to be accepted in the next fit iteration (number of sigmas)
double FitFirstStep = 100	Maximum residual accepted in the first iteration (ns)
double DirPrecision = 0.01	Precision in the reconstruction of the direction to stop the iteration process (degree)
double PlanarFitSigmaCut = 3.0	Maximum distance of the hit from the shower front to be accepted in the next fit iteration for planar fit(number of sigmas)
double TimeWindow=400.0	Time window for noise filter (ns)

Table 4.2: Variables set in the CONFIGURATION FILE for calibration procedure.

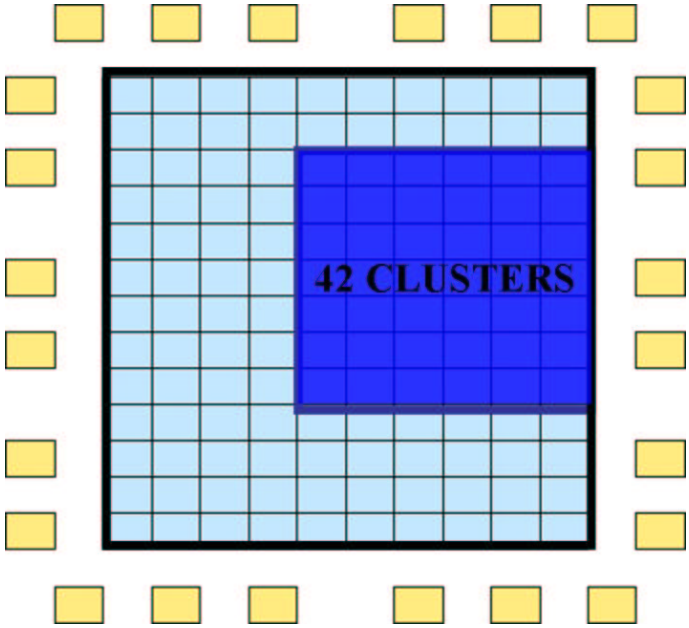

Figure 4.1: The data used for this calibration have been collected with 42 CLUSTERs.

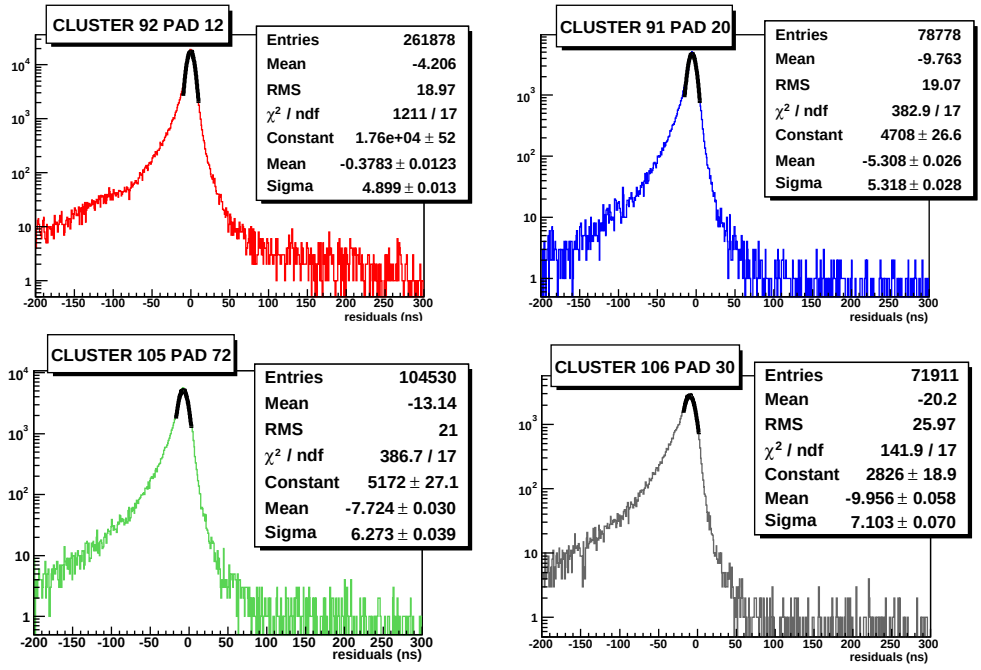

Figure 4.2: Distribution of the residuals (differences betwwen time estimated by planar fit and measured time) for single PADs (PADs 12,20,72 and 30 of CLUSTERs 92,91,105,106, before calibration. The Gaussian fit is applied in the range ± 10 ns around the bin with maximum number of entries. The mean of the Gaussian curve is called the residual of the PAD.

The estimate of the mean values of the direction cosines is necessary in order to complete the calibration correction. In Fig. 4.6 the direction cosine distributions are shown at different steps of the procedure. The full corrections are shown in Fig. 4.4. After calibration the residuals become those of Fig. 4.5. We observe that they are distributed on a saddle surface (third plot). The study of this result by means of a full MonteCarlo will be described in Sec. 4.2. Anyway the residuals are in a range of $\sim 0.5\ ns$.
The results are summarized in Table 4.3 and in the third plot of Fig.s 4.5 and 4.6. As expected at the end of the calibration procedure, the mean values of the direction cosines are compatible with zero, the mean value of the χ^2 for the planar fit of the showers is lower. The azimuth distribution is close to be uniform and the change of the mean θ is negligible.

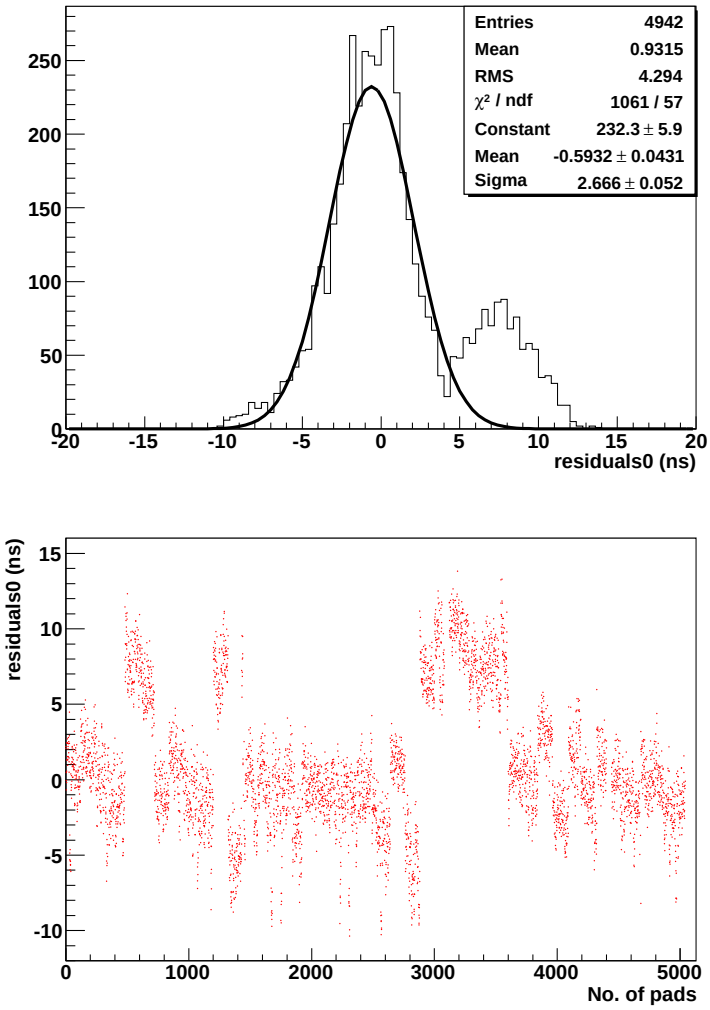

Figure 4.3: Residuals before the calibration procedure. Distribution of residuals (first plot), residuals versus PAD index (second plot). A gaussian fit is superimposed in the first plot, but we do not expect a Gaussian distribution. The residuals depend on electronics, cable length and systematic shifts for some CLUSTERs are expected.

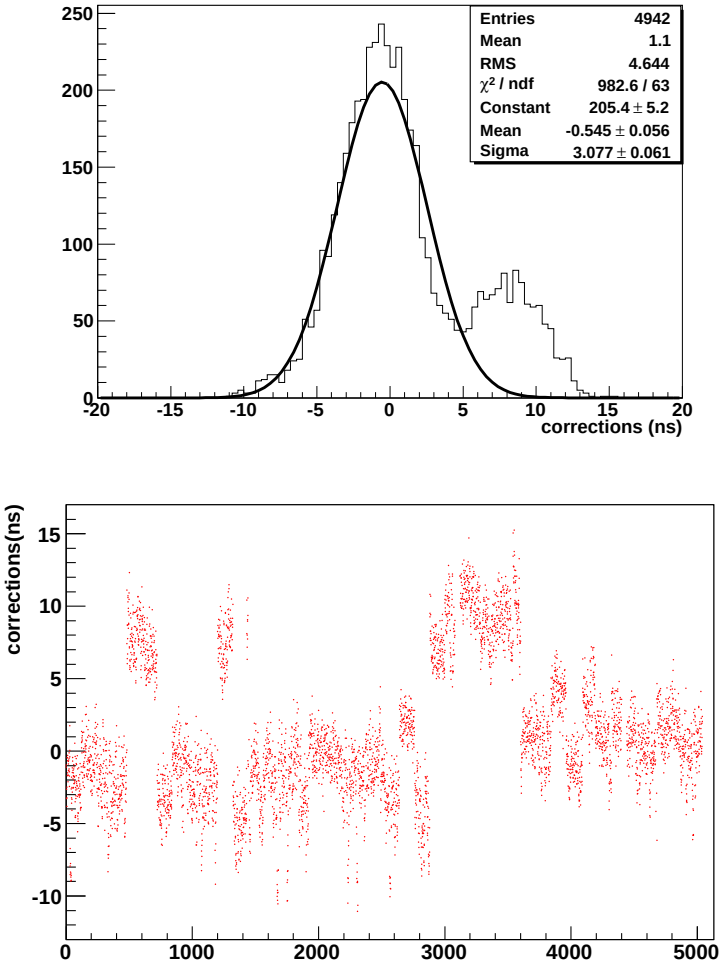

Figure 4.4: CP corrections. Distribution of corrections (first plot), corrections versus PAD index (second plot). They are similar to the residuals but the CP correction has been added.

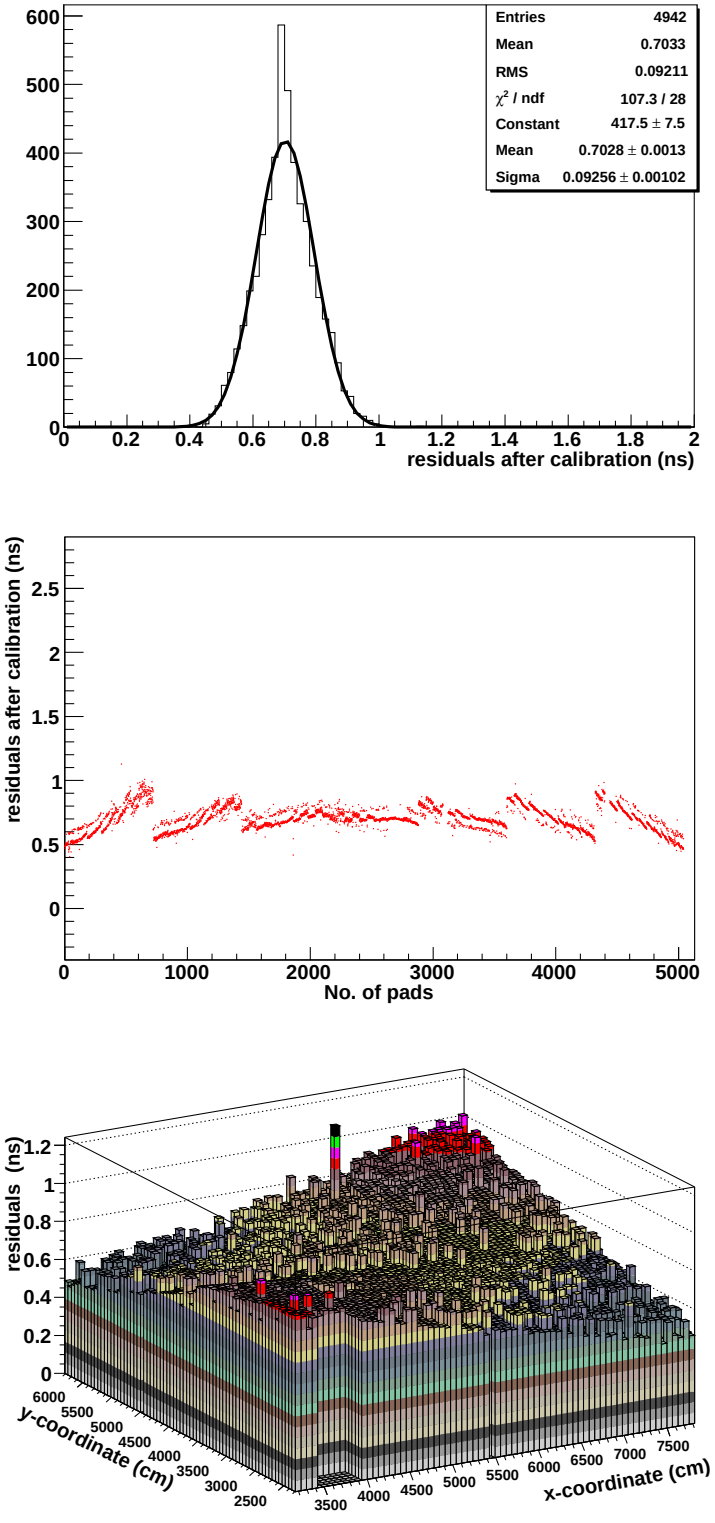

Figure 4.5: Residuals after the calibration procedure. Distribution of residuals (first plot), residuals versus pad number (second plot) and residuals versus pad position (third plot). Observe the saddle shape in the last plot (see comments in the text).

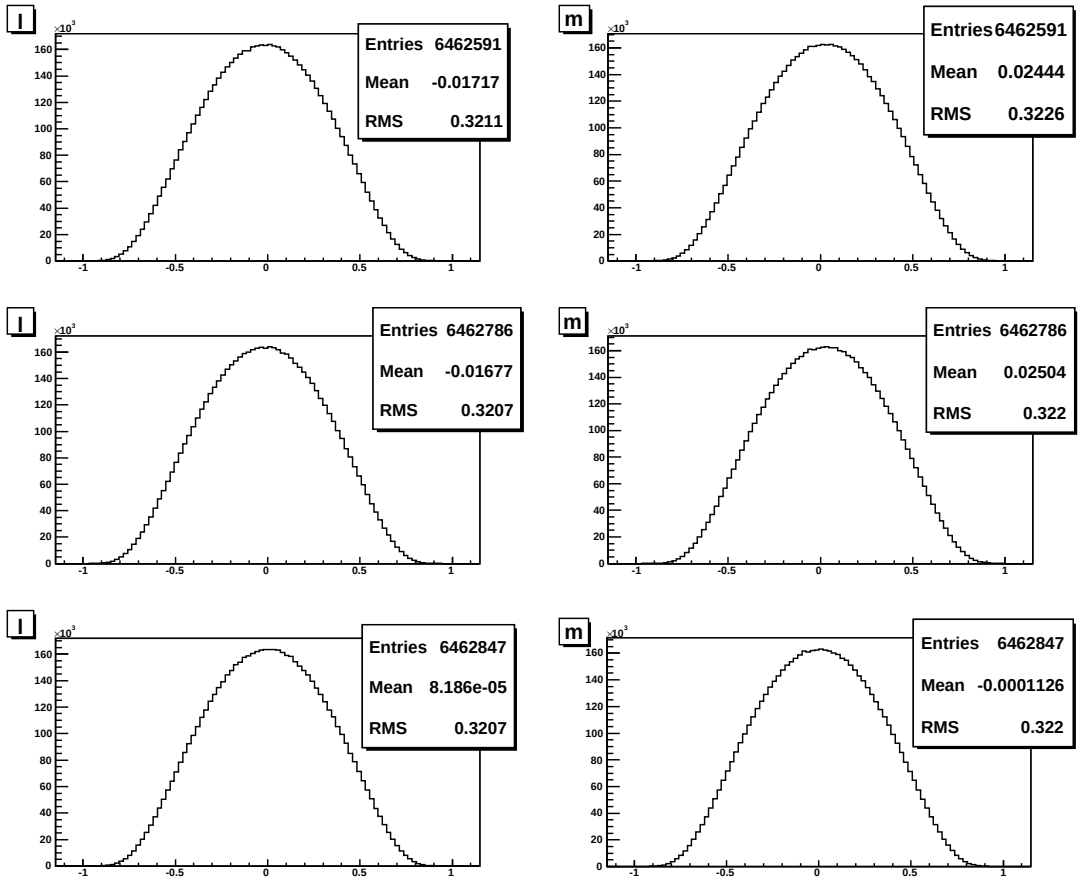

Figure 4.6: Calibration data set - Distribution of direction l and m cosines before the calibration, with only the residual correction and with also the systematic correction.

	Before correction	Residual correction	Residual + systematic corrections
Residual mean value (ns)	0.93	0.71	0.71
Residual RMS (ns)	4.29	0.10	0.10
Mean χ^2 for planar fit of the shower (ns^2)	121.3	94.2	94.2
$< l > (\times 10^{-4})$	-171.7 ± 1.3	-167.7 ± 1.3	$+0.8 \pm 1.3$
$< m > (\times 10^{-4})$	$+244.4 \pm 1.3$	$+250.4 \pm 1.3$	-1.1 ± 1.3
χ^2/ndf for uniform fit of the ϕ distribution	$34 \times 10^3/71$	$35 \times 10^3/71$	159/71
Mean θ value (degrees)	25.33	25.29	25.23

Table 4.3: Values of some parameters at different steps of the calibration procedure for ARGO-42.

4.1.1 TDC distributions

The original TDC values are not directly used in the calibration procedure, but the residual and systematic corrections have effect on them. The spread of the TDC values is ~ 20 ns before the calibration. The improvement due to CP corrections has been tested: the spread is reduced to ~ 6 ns. In Fig. 4.7 the TDC peaks are displayed versus the pad position. A regular concave shape (circular symmetry) is present: the internal pads have the lowest TDC values and the external pads have the highest TDC values. In other words typically the external pads fire before the internal ones (see Sec. 3.5).

4.1.2 Calibration stability

A monitoring of calibration by means of χ^2 from planar fit has been performed to define a period in which calibration was still valid. In principle, if data are collected during a period of stable data taking, it has been verified calibration remains valid. However continuos changes during the installation of CLUSTERs to complete the detector, didn't permit until now to define a definitive period of constant calibration validity. Moreover it has been verified that changes of Local Stations and cables introduce differences in TDC distributions which affect CP corrections. Nevertheless we verified that after more than six weeks the calibration is still valid. The data used for this check have been collected at February 22 with trigger LM 120. Applying the time-corrections the residual values result in a range of ~ 1 ns (Fig. 4.8)

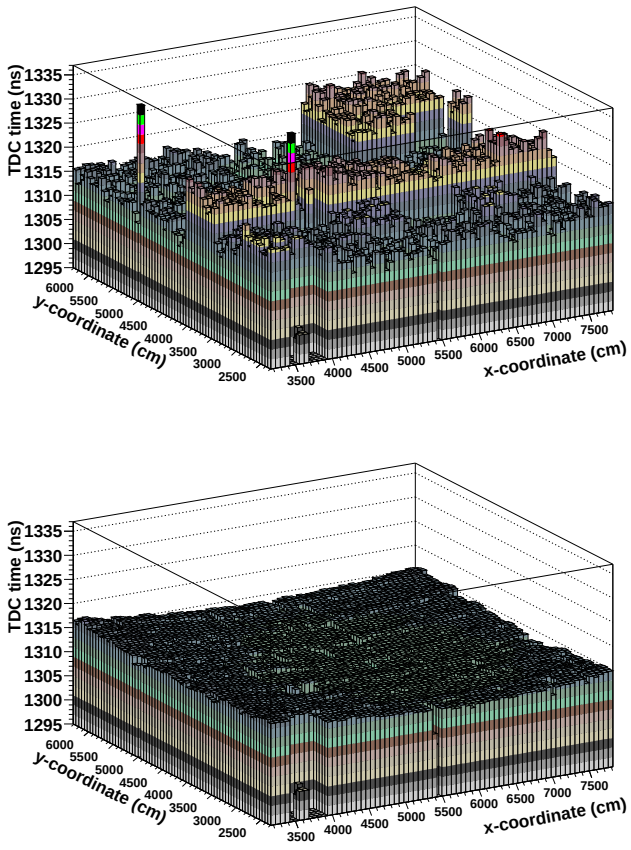

Figure 4.7: Calibration data set - The TDC peaks versus the pad coordinates before and after the calibration.

and the azimuth distribution is flat (Fig. 4.9). The residual distribution for the calibration data set (Fig. 4.5) is more narrow but we have to keep in mind that the calibration is optimized for that sample and the statistics of the check data set is lower. The validity of the calibration has been checked also for data collected with trigger LM 60 (see Table 4.1) with the same good results.

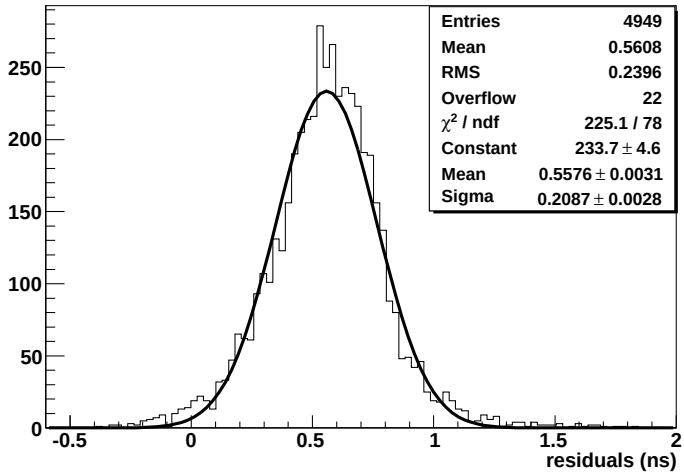

Figure 4.8: Check data set (LM 120) - Residual distribution after the calibration.

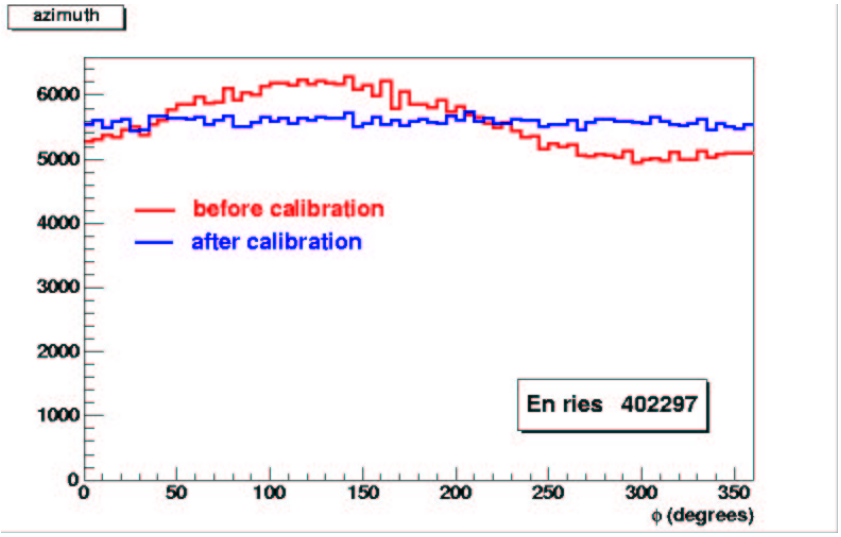

Figure 4.9: Check data set (LM 120) - The azimuth distribution before and after the calibration.

4.2 Simulation

A complete simulation in order to check the validity of the procedure and to understand the saddle shape of the residuals after calibration has been performed. 4 millions of protons have been generated using the software package CORSIKA [41] with energy in the range 100 GeV - 100 TeV (with spectral index $\gamma = -2.7$) and $\theta < 60°$. The secondary particles of the EAS induced by the protons reaching the ARGO-YBJ surface are propagated through the detector by ARGOG, a Monte Carlo program developed to fully simulate the detector [40]. In this case only 42 CLUSTERs have been simulated, with a trigger efficiency of 25% on a generation area of 200×200 m^2 requiring LM 60. The residuals for 5040 PADs are calculated according to the planar shower front and are shown in the first plot of Fig. 4.10. *Ad-hoc* systematic time-offsets (second plot of Fig. 4.10) have been introduced in the detector in order to mis-calibrate it (each PAD has been shifted with the associated offset). The calibration procedure has been applied and the final residuals are shown in the third plot of Fig. 4.10. The calibration removes the delays, in fact the root mean square (RMS) of residual distribution reduces from 1.593 ns to 0.04 ns after calibration. Nevertheless a small systematics has been introduced: the residual of third plot are so different with respect to residuals of first plot of Fig. 4.10. An overcorrection has

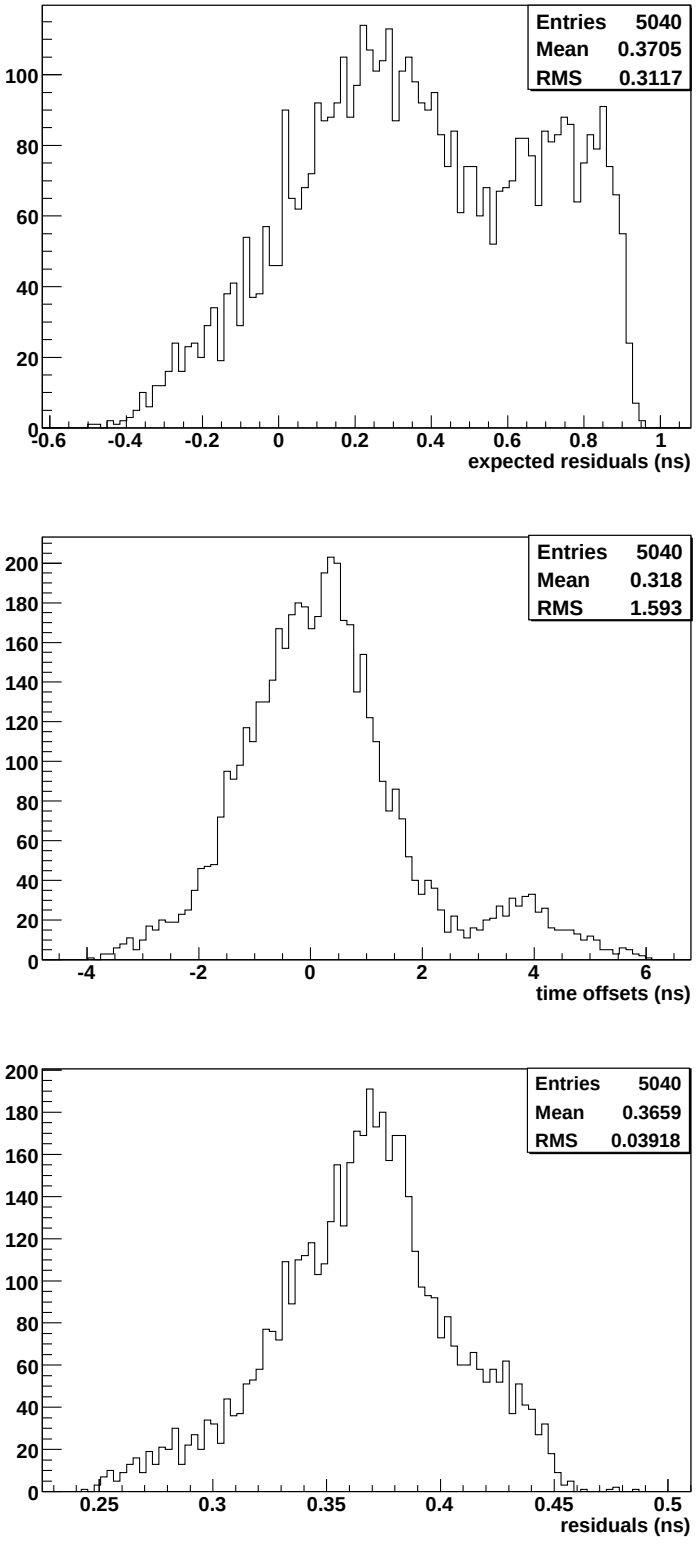

Figure 4.10: Simulation - First plot: distribution of the planar fit residuals when time-offsets are not present. Second plot: the same distribution when time-offsets have been introduced. Third plot: the residual distribution after the calibration.

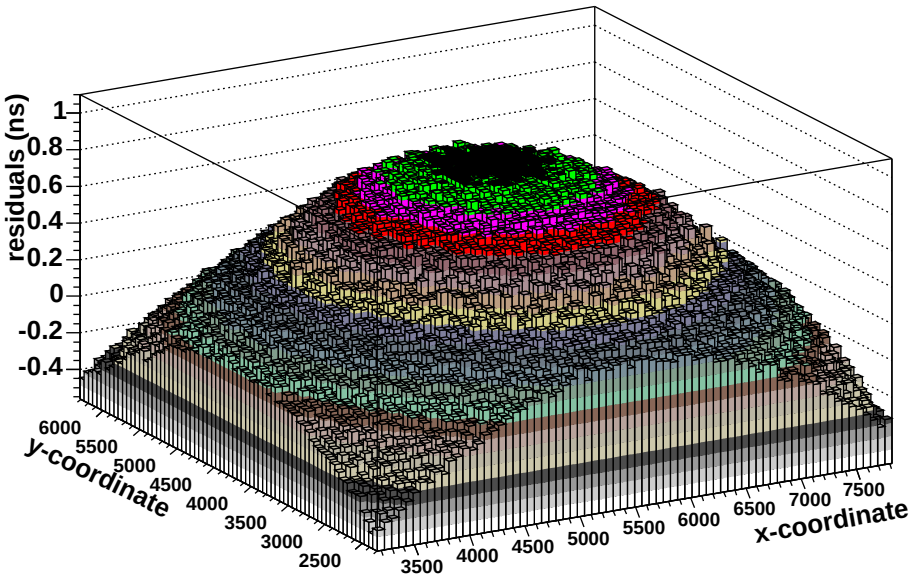

Figure 4.11: Simulation without time offsets - The planar fit residuals have a circular structure because of the shower conicity (first plot).

been introduced by the use of the planar fit because the shower front is indeed better reconstructed with a conical fit. Fig. 4.11 shows the residual distribution versus pad position without calibration and without time offsets: the circular structure is due to the fact that a planar fit is applied to conical showers (see Fig. 4.12). The residuals are positive for internal PADs (close to the center of the carpet) and negative for external PADs (on the edges of the carpet). According to this analysis the shower reconstruction with a conical fit permitted to remove the residual systematics. Conical calibration has been checked for ARGO-42 data. Results of CP method with conical correction applied to ARGO-130 data will be showed in Sec. 4.3.

4.2.1 Azimuth distribution from MC and estimate of South-North asymmetry

ARGO-YBJ array is situated at 30°06′38″N, 90°31′50″E, and its geomagnetic declination θ_H is $\sim 45°$. A small modulation in the azimuth distribution is expected as an effect of the geomagnetic field [33].
In the geomagnetic field, the secondary charged particles generated in EAS

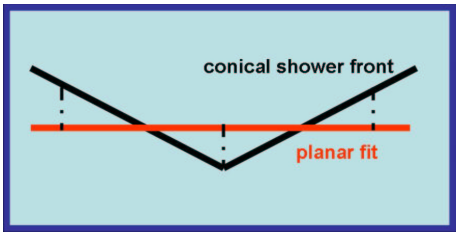

Figure 4.12: Conical showers reconstructed with a plane. Internal PADs have positive residuals, external PADs have negative residuals.

are rotated by Lorentz force. For showers arriving from the north the shower particles have higher deflection than the southern showers of the equal energy with the equal zenith angle. We define χ the angle between the primary momentum and the geomagnetic field as follows:

$$\chi = arccos(cos\theta cos\theta_H + sin\theta sin\theta_H cos\phi) \tag{4.2}$$

where ϕ is the primary azimuth with $\phi = 0$ referring to the geomagnetic north. The geomagnetic parameter g is defined as:

$$g = \frac{\sin\chi}{\cos^2\theta} \tag{4.3}$$

with $A = sin^2\theta + sin^2\theta_H(cos^2\theta - \frac{1}{2}sin^2\theta)$, $B = -\frac{1}{2}sin2\theta sin2\theta_H$. Thus,taking secondary electron as an example, the average shift in the shower plane [33] is:

$$d = \frac{h^2 B \sin\chi}{2E_e \cos^2\theta} \tag{4.4}$$

where h is the average vertical height of the electron trajectory, B is the geomagnetic field, E_e is the average energy of electron, θ is the primary zenith angle. According to Eq. 4.3 d is proportional to the geomagnetic parameter and inversely proportional to the enrgy of the secondary particle in the shower. The geomagnetic parameter at YBJ (Fig 4.13) is larger in the North than that in the South, that becomes more evident for larger zenith angles. Geomagnetic parameter leads directly to the stretch of the EAS lateral distribution. As a consequence a deficit of the event rate [33] from the geomagnetic South angle with respect to that from the geomagnetic North is expected causing modulations in azimuth distribution. The expected azimuth distribution from ARGO-42 simulation is shown in Fig. 4.14.

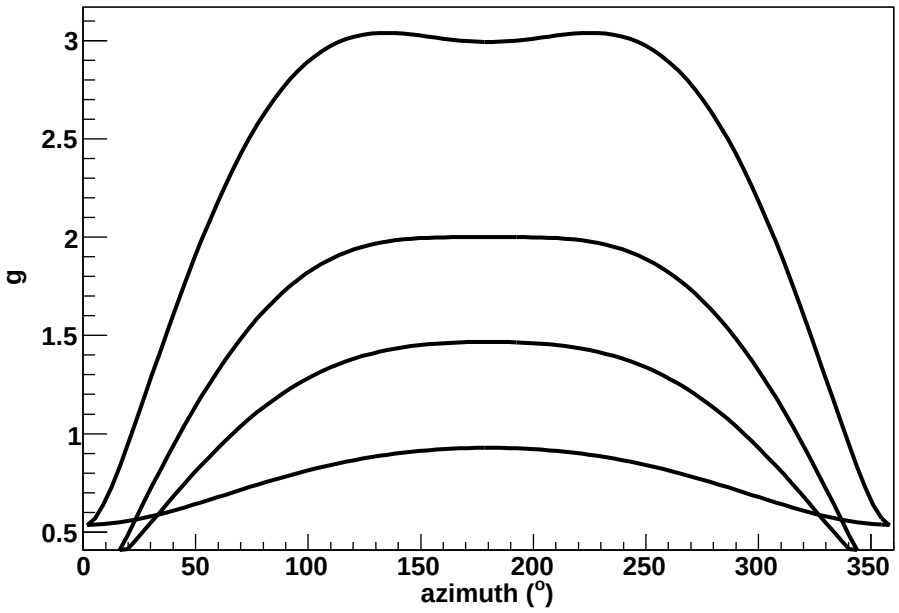

Figure 4.13: Geomagnetic parameter at YBJ varying with azimuth angle at different zenith angle (from bottom to top: 15°,35°,45°,55°).

The distribution is well fitted with two harmonics $p0[1 + p1\cos(\phi + p2) + p3\cos(2\phi + p4)]$. As it can be seen in Fig. 4.14 both first and second harmonics are equally prevailing. This is not tipical, in fact at the Yakutsk array ($62°N$,$130°E$; $\theta_H = 14°$) the first harmonic dominates while at the Chakaltaya array ($16.35°S$,$68.2°W$; $\theta_H = 88°$) the second harmonic prevails. In the sample used for simulations the number of events from North ($161.5° < \phi < 341.5°$) result less than the number of events from South. The asymmetry expected is:

$$\frac{2(S-N)}{S+N} \simeq 1\% \tag{4.5}$$

Tibet ASγ array (30.11° N,$130°E$; $\theta_H = 45°$) estimates a 2.5% higher rate from South direction with respect to North direction. This value is explained with geomagnetic field and with the slope of the hill where the array is located.

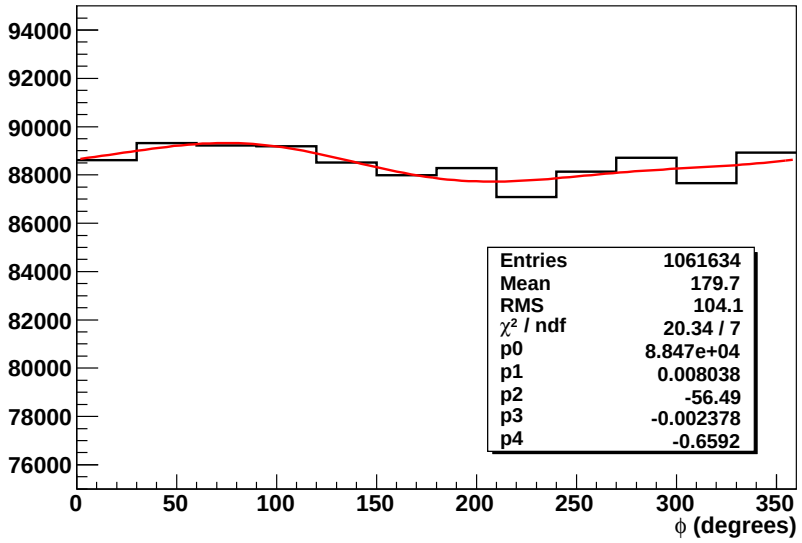

Figure 4.14: The expected azimuth distribution shows a South-North asymmetry of $\simeq$ 1%. The distribution is fitted with a function $p0[1 + p1\cos(\phi + p2) + p3\cos(2\phi + p4)]$.

4.3 CP method for ARGO-130

In case of CP Method with conical correction the Eq. 3.1 becomes:

$$t_{ij} - \Delta_j = l_i \frac{x_j}{c} + m_i \frac{y_j}{c} + t_{0i} + \frac{\alpha}{c} R_j \tag{4.6}$$

where α is the conicity parameter and R_j is the distance to the core of the PAD j. The calibration with conical corrections is applied in the following to the complete carpet (130 CLUSTERs) in data acquisition since June 2006. The runs have been chosen in order to have a stable data-taking. We selected 280 files with size larger than 500 MB (three days of data-taking, since 18th to 20th September 2006). Since a good reconstruction of the core position is crucial for the conical fit, events have been reconstructed with the following features:

- core reconstructed inside the carpet
- more than 1500 hits in each event

The residuals before the calibration are shown in Fig. 4.15. Each pad-time has been corrected in agreement with these residuals and the mean values of the direction cosines. The procedure has been repeated six times. For 344 pads (only 2.2% of all pads) the calibration was impossible because of the poor statistics or because they were really offline during the selected days. These pads have been corrected according to the mean correction of the corresponding chamber or cluster (when all the pads of the RPC are not calibrated). A calibration file with all corrections has been finally produced. The calibration has been applied to a smaller sample, 5 files with size larger than 1 GB of September 20, 2006. For this check no cuts have been applied to the events because the time corrections depend only on hardware differences (cable length, electronics delays and so on) and do not depend on analysis cuts or trigger conditions. The residuals calculated with Medea++ are shown in Fig. 4.16. As expected the residual distribution for planar fit is larger as an effect of conical shape of the shower front. Indeed Fig. 4.17 (first plot) shows the circular structure of the residuals expected when the planar fit is applied to conical showers. When the conical fit is used this systematics disappears and the residual distribution is more narrow (second plot of Fig. 4.17). In Tab. 4.4 87 pads with large residual (more than 3σ away from the Gaussian mean value) have been reported. These time shifts are not random fluctuations because only 40 pads are expected with so high residual, according to Gaussian statistics. Furthermore the 87 pads are in few CLUSTERs and chambers and in Fig. 4.17 the time shift is evident for

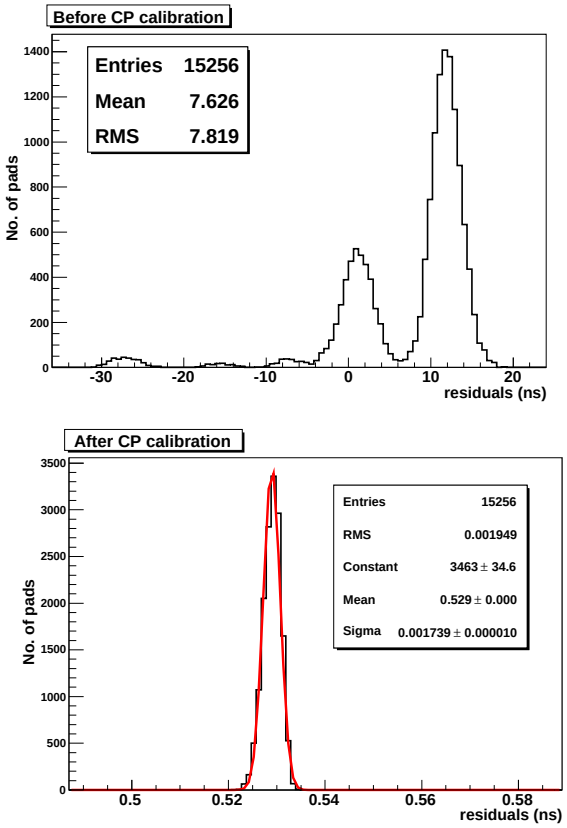

Figure 4.15: Distribution of residuals for ARGO-130: before (first plot) and after CP calibration (second plot). The conical fit is used for the event reconstruction.

some CLUSTERs. Thus these pads were affected by some time drift with respect to the sample used for the calibration. This question of the time drift in some CLUSTERs will be discussed and possibly solved in Sect. 4.4. The first plot of Fig. 4.17 shows the same systematics observed in the ARGO-42 simulation (Fig. 4.11). The planar fit does not reconstruct the shower shape. The systematics is much lower using the conical fit (second plot of Fig. 4.17) but it does not disappear at all. We can conclude that also the conical shape is only an approximation of the shower front.

pad	cluster	residual (ns)	pad	cluster	residual (ns)	pad	cluster	residual (ns)
70	31	0.74	4728	82	1.83	10606	151	1.71
130	32	0.75	4730	82	2.04	10744	152	2.57
202	32	20.90	4739	82	1.93	10921	158	0.66
980	39	0.75	4740	82	1.67	10923	158	0.74
2601	60	4.92	4779	82	1.73	11381	161	1.74
2603	60	3.52	4820	87	0.76	11741	164	1.80
2604	60	5.33	5505	92	1.66	12123	172	0.75
2605	60	4.12	6070	101	0.71	12512	175	0.66
2606	60	3.59	6130	102	0.72	12518	175	0.67
2607	60	2.35	6537	105	2.01	12519	175	0.66
2608	60	5.03	6555	105	1.67	13670	188	0.76
2609	60	4.53	6586	105	1.66	13781	189	-1.60
2610	60	7.31	6638	106	1.67	13782	189	-1.54
3121	65	0.67	6989	109	1.93	13783	189	-2.07
3160	65	0.66	7618	118	1.70	13784	189	-0.74
3193	65	0.76	7690	119	2.01	13785	189	-1.00
3199	65	0.76	7799	119	1.94	13786	189	-2.32
3229	65	0.75	8261	123	2.69	13787	189	-1.12
3481	68	0.69	8263	123	1.78	13788	189	-1.50
3789	74	-0.77	8264	123	2.78	13789	189	-0.91
4436	79	0.74	8265	123	1.66	13790	189	-1.41
4450	80	0.64	8266	123	1.81	14131	192	1.69
4693	82	1.76	8394	124	1.77	14530	200	0.76
4702	82	1.68	8670	131	1.72	14644	201	0.75
4709	82	1.77	9091	134	1.70	15369	207	0.68
4721	82	1.93	9316	136	1.68	15481	208	0.75
4722	82	1.76	10133	147	1.92	15571	208	2.03
4724	82	1.79	10136	147	1.68	15579	208	1.72
4726	82	1.84	10587	151	1.67	15580	208	1.89

Table 4.4: List of the 87 pads with residuals external to the Gaussian distribution (more than 3σ with respect to the Gaussian mean value).

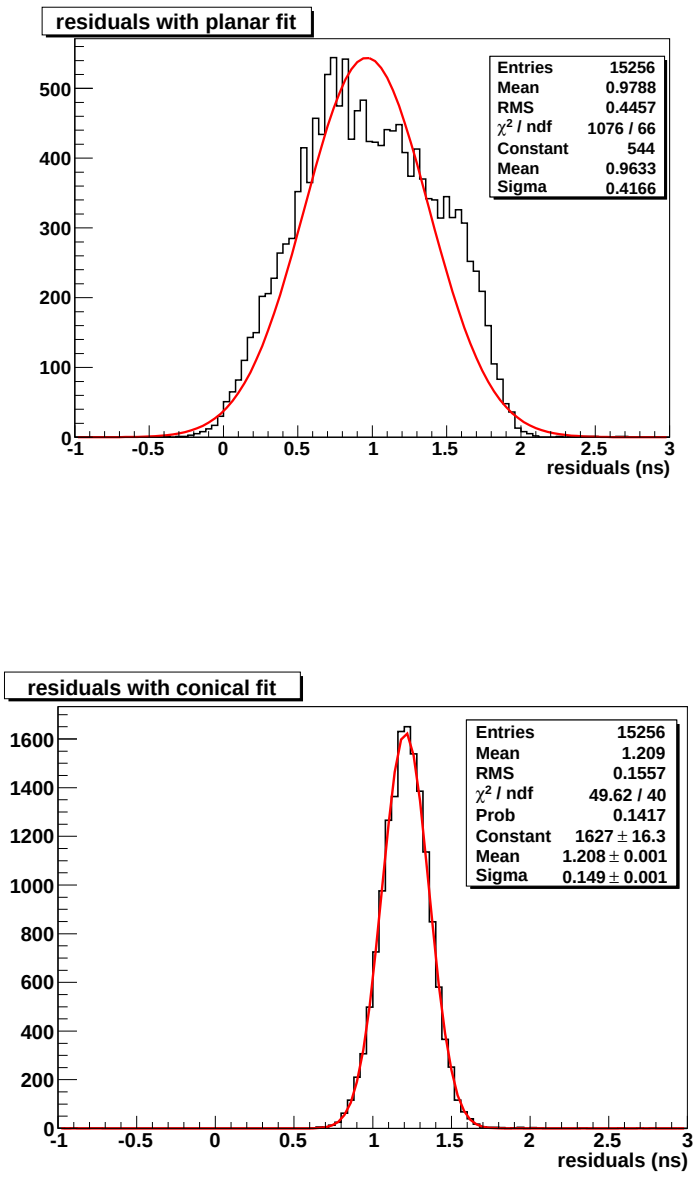

Figure 4.16: Calibration check for ARGO-130. Residuals after CP calibration with planar fit (first plot), with conical fit (second plot).

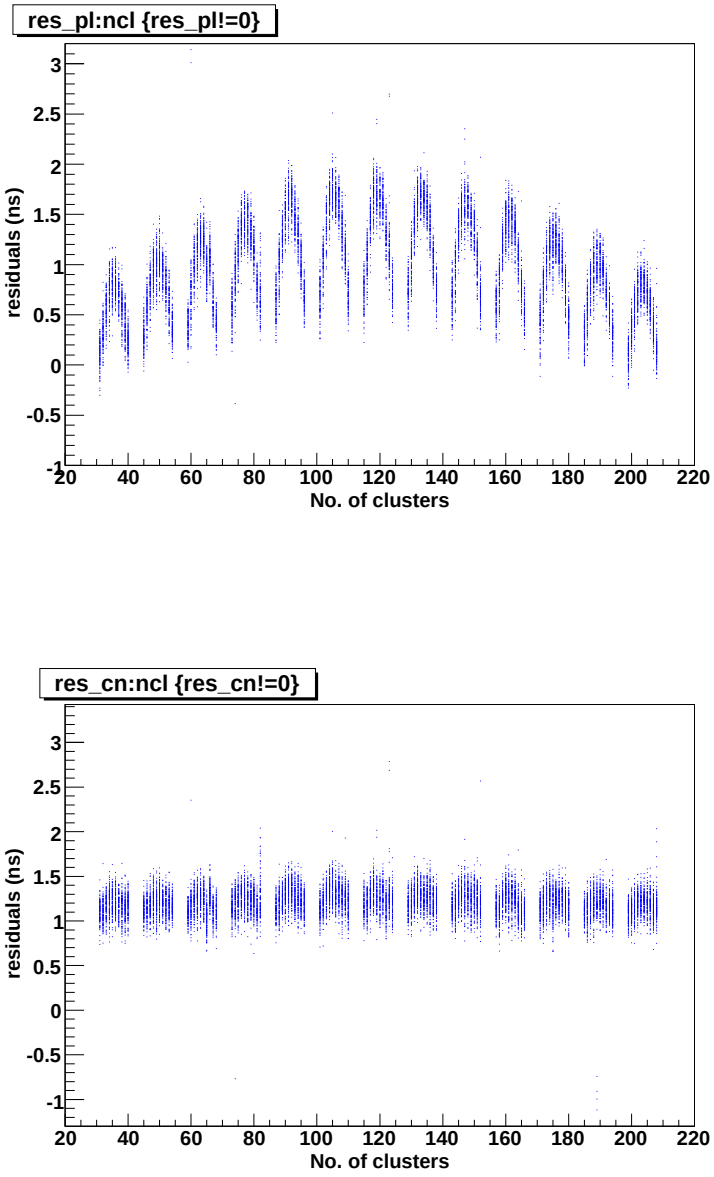

Figure 4.17: Calibration check for ARGO-130. Residuals vs cluster number after CP calibration with planar fit (first plot) and with conical fit (second plot). See the text for some comments.

4.3.1 Azimuth distribution and pre-modulation after calibration.

Before the calibration a strong modulation ($\sim 16\%$) is present in the azimuth distribution. We know that this is an effect of the Characteristic Plane. After the calibration this modulation is lower and lower (Fig. 4.18). As expected [37] the CP method annulls the mean values of the primary direction cosines but a small sinusoidal modulation is still present in the azimuthal distribution. The ϕ-distribution has been fitted with the function:

$$\frac{dN}{d\phi} = p0\,[1 + p1\cos(\phi + p2) + p3\cos(2\phi + p4)] \tag{4.7}$$

According to the fit coefficients and phases of the first and second harmonics due to the geomagnetic field (see Chapter 3)result:

$$g_1 = \frac{-p1}{1-\frac{1}{2}\langle\sin\theta\rangle\left\langle\frac{1}{\sin\theta}\right\rangle} = 1.0\%, \qquad g_2 = -p3 = 0.9\%$$

$$\phi_1 = p_2 = -0.673 \text{ radians}, \qquad \phi_2 = p_4 = +3.46 \text{ radians}$$

The estimated mean values of direction cosines according to Eq.s 3.10 are:

$$\langle l\rangle = +\frac{g_1}{2} cos\phi_1 \langle\sin\theta\rangle = +17\times 10^{-4} \qquad \langle m\rangle = -\frac{g_1}{2} sin\phi_1 \langle\sin\theta\rangle = +13\times 10^{-4} \tag{4.8}$$

The mean values of direction cosines after the CP corrections are:

$$\langle l\rangle = (4.38 \pm 0.15)\times 10^{-4} \qquad \langle m\rangle = (1.52 \pm 0.15)\times 10^{-4} \tag{4.9}$$

To complete the CP calibration a new systematical correction is necessary in such a way that the mean values of direction cosines become those of Eq. 4.8. But the correction is so small and the uncertainties in the fit of the azimuthal distribution are so large that this new correction has not been applied, assuming that the values (4.8) and (4.9) are compatible.

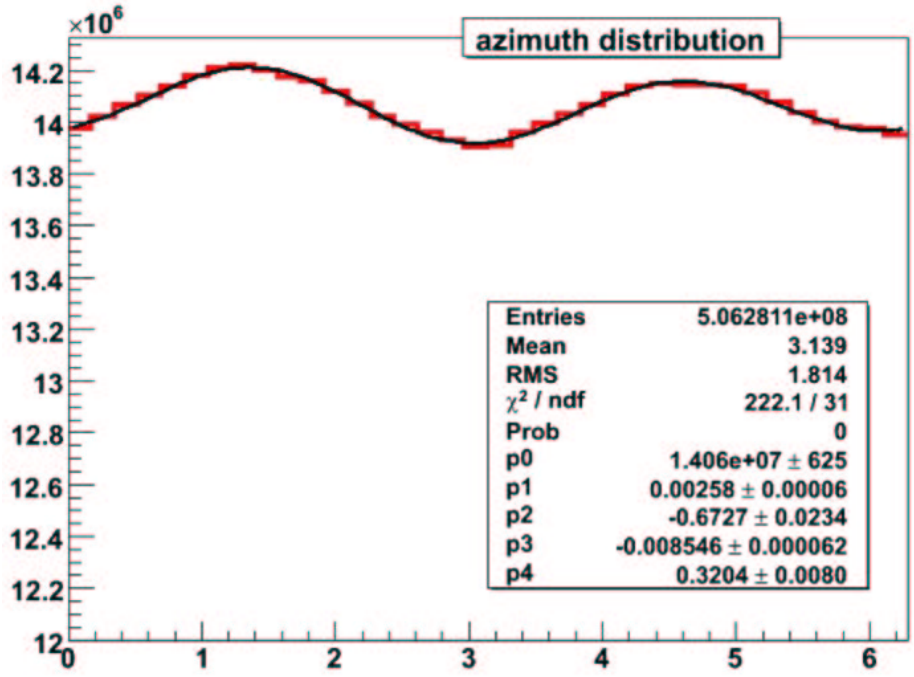

Figure 4.18:Azimuth angle distribution after CP calibration. The distribution is fitted with the function $p0\,[1 + p1\cos(\phi + p2) + p3\cos(2\phi + p4)]$.

4.4 TDC method to update the calibration

As shown in Fig. 4.19 the TDC peaks (T) have different values for different pad-positions (x, y). Their gradient is not null:

$$\vec{\nabla}\ T(x,y) = \vec{S}(x,y) \neq 0$$

They are distributed on a concave surface which becomes very regular applying the calibration timing corrections. The TDCs in the center of the carpet have values lower than those on the edge. This is an expected effect observed also in the simulation. The shape of the surface changes with the trigger conditions.
Taking into account the time (t) and using the same trigger, the calibration is valid as long as the TDC-surface is stable:

$$\frac{\partial}{\partial t}\vec{S}(x,y,t) = 0 \tag{4.10}$$

We do not worry if all TDCs change together of the same amount:

$$T(x,y,t) = T(x,y,t_0) + k(t) \tag{4.11}$$

where t_0 is the time of the data used for the calibration and $k(t)$ is a uniform term, independent on x, y, but varying with t. Indeed the shape of the surface does not change:

$$\vec{S}(x,y,t) = \vec{\nabla}\ T(x,y,t) = \vec{\nabla}\ [T(x,y,t_0) + k(t)] = \vec{\nabla}\ T(x,y,t_0) = \vec{S}(x,y,t_0)$$

and the condition (4.10) is fulfilled. On the contrary a new calibration is necessary when the concave surface is disformed:

$$\frac{\partial}{\partial t}\vec{S}(x,y,t) = \frac{\partial}{\partial t}\left[\vec{\nabla}\ T(x,y,t)\right] \neq 0$$

The period July-October 2006 has been analysed looking at the stability of the TDC according to (4.10) in order to distinguish different periods and to prepare different calibration files. When a significant change in the TDCs is found, the new calibration file is produced without the repetition of the complete CP calibration. We compare the TDCs in the data used for the CP calibration (T_0) with those in the period we want calibrate (T_{new}). The goal is to determine the calibrated TDC value (T^*) for each pad by means of the proper correction (δ). For the two data samples

$$T_0^* = T_0 + \delta_0 \tag{4.12}$$
$$T_{new}^* = T_{new} + \delta_{new} \tag{4.13}$$

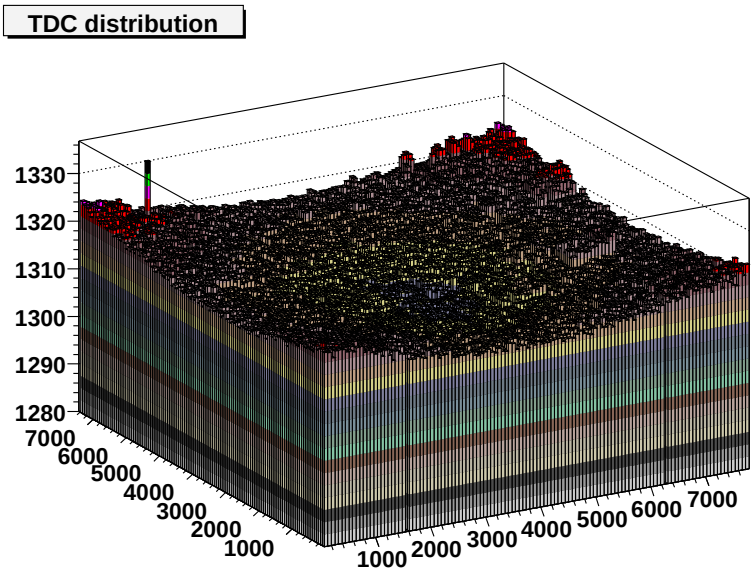

Figure 4.19: Map of the TDC peaks (after the calibration).

Requiring $T_0^* = T_{new}^*$, it is simple to estimate pad by pad the new corrections:

$$\delta_{new} = T_0 - T_{new} + \delta_0 \tag{4.14}$$

Fig. 4.20 shows the differences of TDC peaks in six periods of data-taking using the day 263 (September 20, 2006) like reference day. We can observe that the TDCs of CLUSTERs 32, 39, 171, 172 had large changes in time. As a result of this check, since the middle of July to the beginning of November 2006[1], we distinguish 5 periods (see Table 4.5) with considerable differences on TDC peak values. The choice of these five samples is obviously arbitrary, unexpected changes can also occure during shorter periods of data-taking. A day-by-day calibration in order to remove this arbitraryness.

The sample IV has been calibrated with the CP method. For the other samples we used the TDC method, that is the formula (4.14).

[1] The stable data-taking with 130 CLUSTERs starts since July 19, 2006.

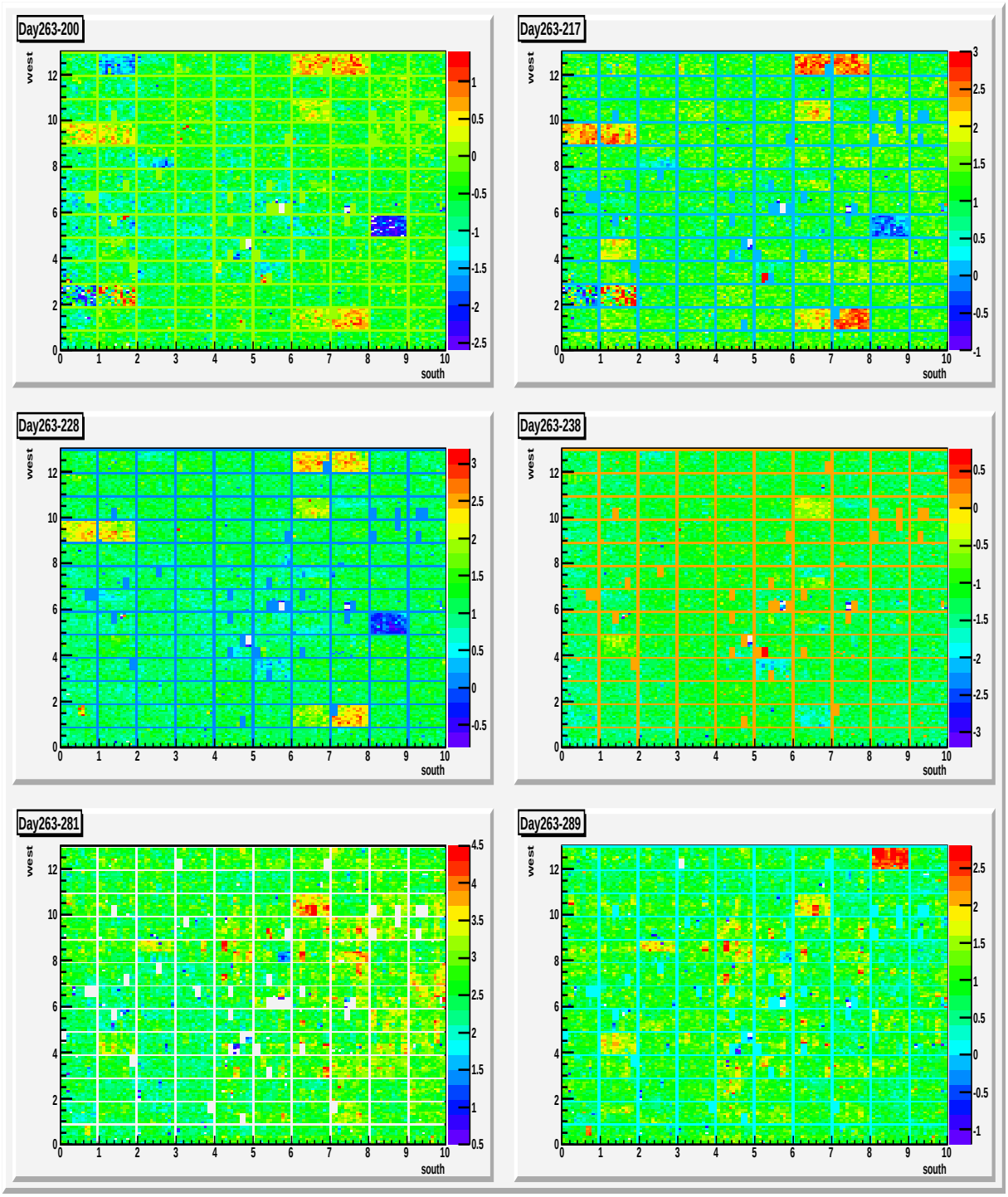

Figure 4.20: Differences of TDC peaks versus PAD position without calibration in six periods of data-taking. The day 263 (September 20, 2006) is used like reference day. The color scale is in TDC pitch (1.042 ns).

	since ...	to ...	days in 2006
I)	July 13	July 20	194-201
II)	July 21	August 6	202-218
III)	August 7	August 21	219-233
IV)	August 22	October 14	234-287
V)	October 15	October 27	288-300

Table 4.5: Five periods with different calibrations.

4.4.1 Check on the TDC method

The validity of the TDC method as a fast updating of the CP calibration has been checked calibrating the data collected in the day 306 (November 3, 2006) with both the methods. The corrections of the complete CP calibration result very close to those obtained with the TDC updating, based on the comparison of the TDC peaks with those of September 20 (see Fig. 4.21). Fig. 4.22 shows the differences between the two corrections. The distribution is well reproduced by a Gaussian function. We do not care about the mean value, only the width is critical. Anyway its value ($\sigma = 0.26\ ns$) is compatible with the statistical fluctuations of the TDC peaks (see next Sections). Thanks to this check we cannot still conclude that the TDC method is suitable to update the calibration constants. Further controls are necessary to understand the TDC shift due to temperature, different detector configuration and so on.

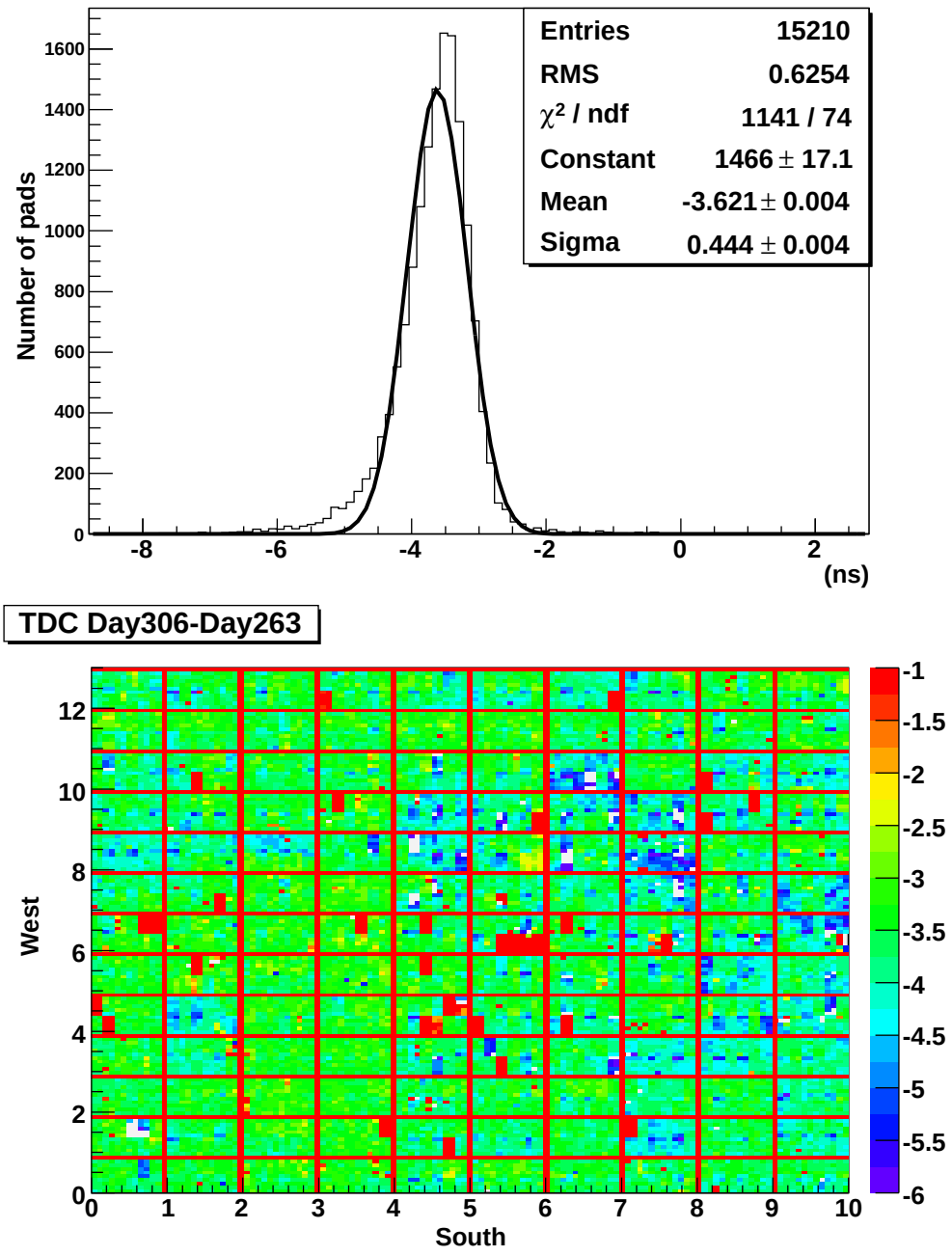

Figure 4.21: Difference of TDC peak values between September 20 and November 3, 2006. Firts plot: distribution. Second plot: map.

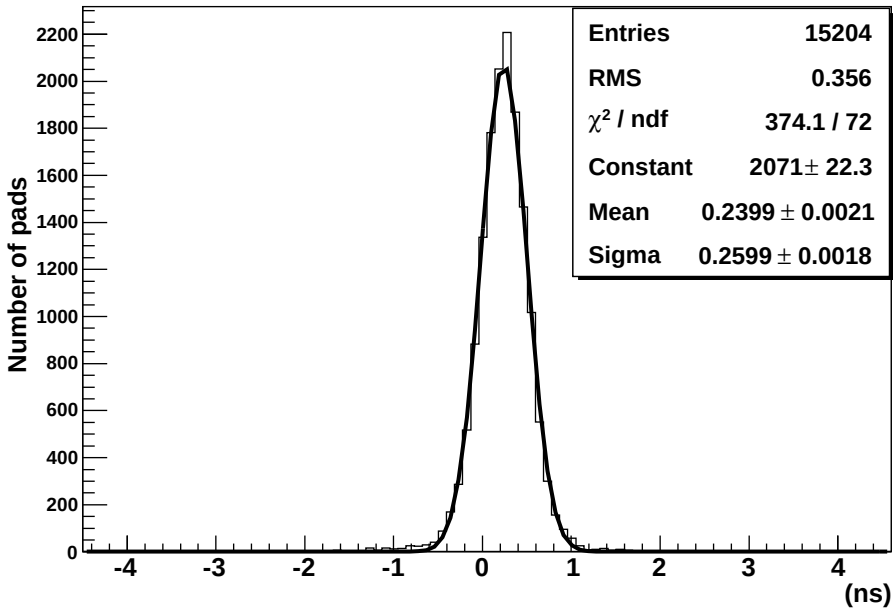

Figure 4.22: Differences between CP and TDC calibration for day 306 (November 3, 2006).

sample	difference	σ (ns)
high temperature	odd-even events	~ 0.51
low temperature	odd-even events	~ 0.39
odd events	high - low temperature	~ 0.52
even events	high - low temperature	~ 0.47

Table 4.6: Standard deviation values of TDC peak differences. The distribution is larger ($\sigma \sim 0.51\ ns$) for higher temperature, in agreement with following observations on the TDC behavior.

4.4.2 Dependence of TDC on temperature (night - day difference)

Thanks to DCS measurements we could take a look at the differences between night and day temperature (see Fig 4.23). The highest temperature (close to the chambers, yellow curve) is measured around 9:48 a.m. (Greenwich time), while the lowest temperature has been measured around 12:20 p.m. We have chosen two different samples during the day 204 (July 23, 2006), the former and the latter when the temperature close to the chambers was highest and lowest, respectively. Looking at the TDC peak differences (Fig. 4.24) we observe a collective shift ($\sim 3\ ns$) like $k(t)$ in the formula (4.11). Some edge-center difference is visible in the map but not so clear and lower than 1 ns. The standard deviation of the Gaussian fit is $\sim 0.36\ ns$. In order to disentangle the statistical fluctuations from the temperature systematics we use the odd-even method. Each sample is divided in two sub-samples, with even and odd events, respectively; therefore each sub-sample has the half statistics of the corresponding full sample (roughly 60×10^3 entries per pad). The standard deviations of the Gaussian fits of TDC peak differences are showed in Tab. 4.6 for various sub-samples . The width of the TDC peak difference between even and odd sub-samples is only statistical (σ_{stat}), because the two sub-samples are collected at the same time and in the same conditions. Therefore we estimate $\sigma_{stat} \sim 0.45\ ns$ (mean value between 0.39 and 0.51 ns). We can now estimate the temperature contribution (σ_{temp}) to the width of the difference distribution between the sample with highest temperature and the sample with lowest temperature:

$$\sigma^2_{high-low} = \sigma^2_{temp} + \sigma^2_{stat} \quad \Rightarrow \quad \sigma_{temp} \sim 0.20\ ns \tag{4.15}$$

We conclude that the main effect of the TDC dependence on temperature is a shift of all TDC peaks, negligible for the calibration. A minor effect is present, that is the shift is not the same for all pads (see the edge-center

Figure 4.23: Temperature vs Greenwich time: external (blue curve), inside the laboratory (purple curve) and measured close to the chambers (yellow curve). Data collected in July 2006.

difference), but this effect is of the order of 0.2 ns. Another temperature effect is the change of the width of the TDC distribution. The calibration cannot correct this effect but we investigated it to understand deeply the TDC behavior. In Figs. 4.25, 4.26 and 4.27 the TDC widths at different times (day-night, different days) are compared. The mean values are positive in all cases, that is during the day the TDC distributions are broader than during the night. The widening is different (0.42, 0.30 and 0.65 ns) and probabily depends on the temperature excursion. Anyway we observe that higher the mean value larger is the edge-center effect, clearly visible in the distribution and in the map, clearer than that observed in Fig. 4.24. Because of this observation we conclude that a temperature gradient is present on the carpet and the TDC behaviour depends on the temperature change. Another check about the temperature effect is possible looking at two parameters of the reconstruction (t_0 and χ^2, see Eq. 2.5). The average values of t_0 and χ^2 are plotted versus time in Fig.s 4.28 and 4.29 for two different days. The t_0 parameter is the time of a pad with position $x = y = 0$, its value is negligible for the direction reconstruction but it is a kind of estimate of the average TDC values. From Fig. 4.28 we observe that t_0 ranges within $\pm$ 0.6 ns with a cycle period of 24 hours (maximum at 6 a.m.), as expected because of the temperature cycle. The cycle is well reproduced in the two days with the exception of 4 hours (6-10 a.m.), may be for some storm or clouds.
The cycle is present also in Fig. 4.29 but the shape is different (maximum at 3 a.m.) and we do not observe significant differences between the two days. Presently we are not able to explain in detail this behaviour. Anyway we can estimate this effect taking into account that χ^2 is the average of the square residual (Δ):

$$\chi^2 = \frac{1}{N}\sum_{i=1}^{N}\Delta_i^2 = \left\langle \Delta^2 \right\rangle .$$

From Fig. 4.29 we estimate that the stronger variation of $\langle\Delta^2\rangle$ is

$$\frac{\langle\Delta_1^2\rangle - \langle\Delta_2^2\rangle}{2} = \frac{\chi_1^2 - \chi_2^2}{2} = \frac{129 - 125}{2} = 2\ ns^2.$$

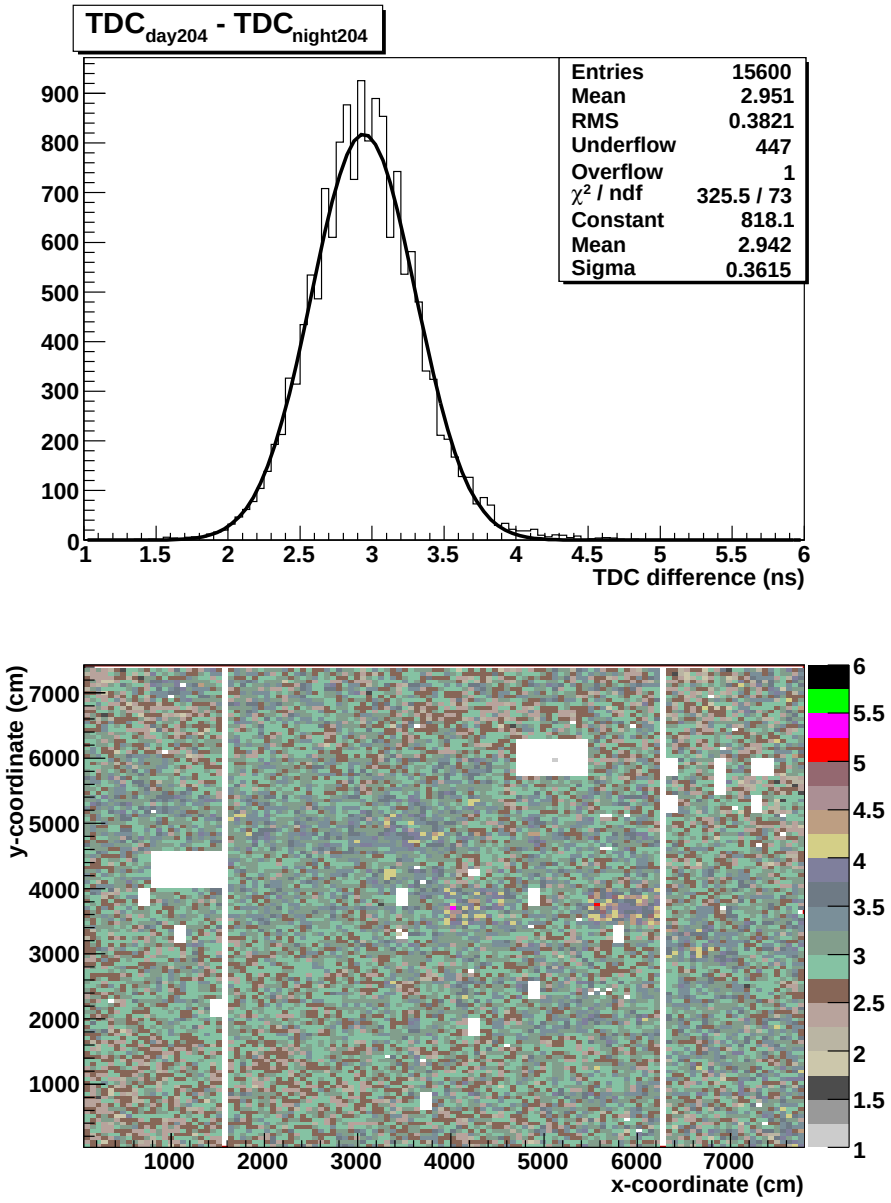

Figure 4.24: Difference of TDC peak values between day 204 and night 204. Firts plot: distribution. Second plot: map.

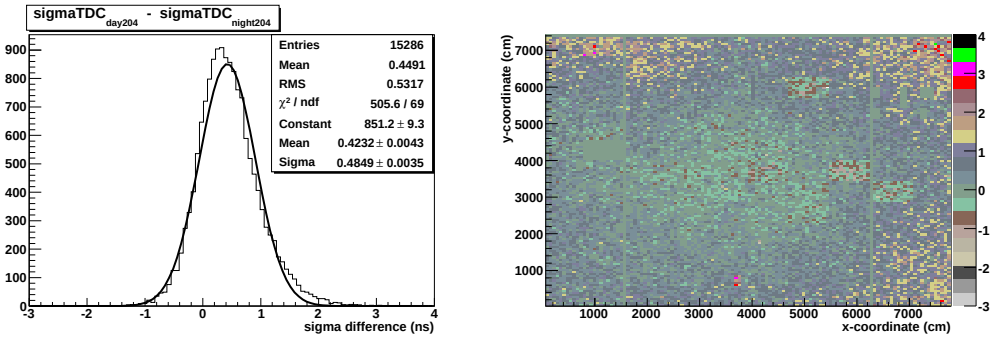

Figure 4.25: Difference of TDC widths between day 204 (July 23, 2006) and night 204. First plot: distribution. Second plot: map.

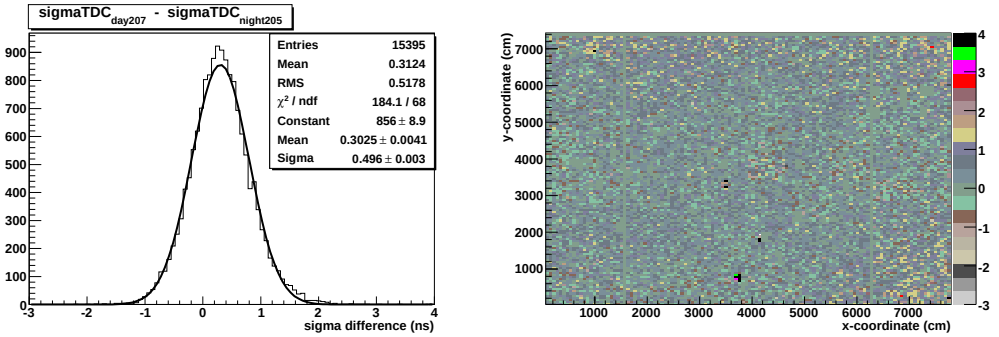

Figure 4.26: Difference of TDC widths between day 207 (July 24, 2006) and night 205 (July 26, 2006). First plot: distribution. Second plot: map.

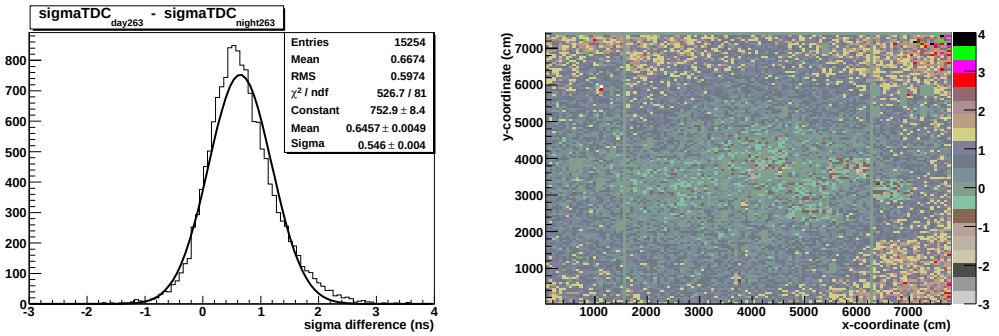

Figure 4.27: Difference of TDC widths between day 263 (September 20, 2006) and night 263. First plot: distribution. Second plot: map.

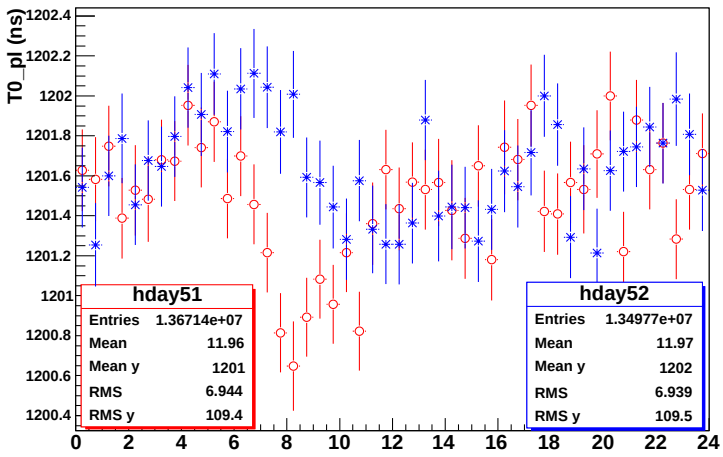

Figure 4.28: Planar fit t_0 versus Greenwich time (hours in the day) for days 52 and 52,2006.

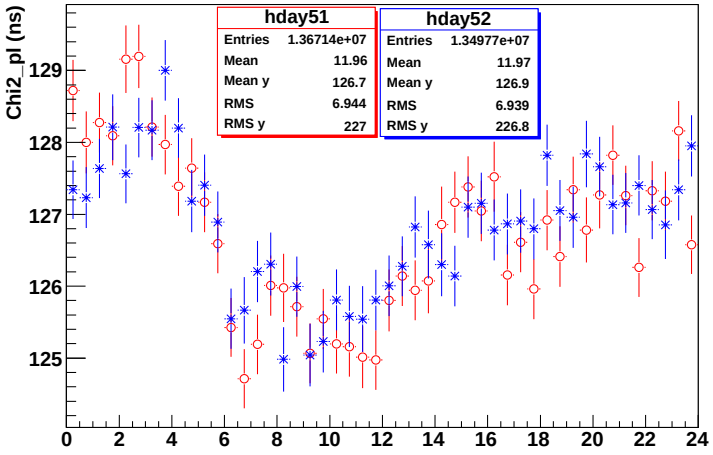

Figure 4.29: Planar fit χ^2 versus Greenwich time (hours in the day) for days 51 and 52, 2006.

4.4.3 Dependence of TDC on offline CLUSTERs

According to Fig. 4.19 we expect that the TDC peak values are higher on the edge and lower on the center of the carpet. Do we expect that also CLUSTERs close to an off-line cluster are on the edge and their TDC peak values are higher?

To answer we have studied the TDC distributions of 8 CLUSTERs all around cluster X (see Fig. 4.30) when the cluster X is in data-taking and when is off. We have used the data of day 239 (August 27, 2006) and 263 (September 20, 2006). In the first sample the cluster 65 is off while in the second sample it is on. We have studied also the CLUSTERs all around cluster 60 (symmetrical to cluster 65, online in both the data samples). The differences of the TDC peaks versus x, y coordinates, between the two samples, are shown in Fig. 4.31.

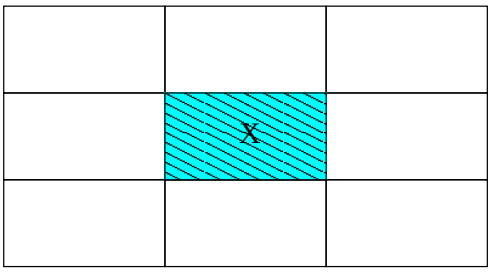

Figure 4.30: The coloured rectangle is the on-off cluster. We have studied the 8 CLUSTERs all around.

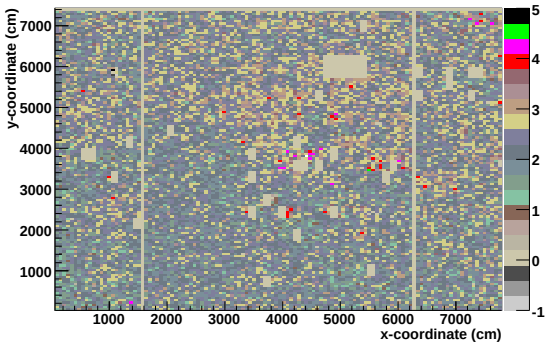

Figure 4.31: Map of TDC peak difference between day 239 (August 27, 2006) and day 263 (September 20, 2006).

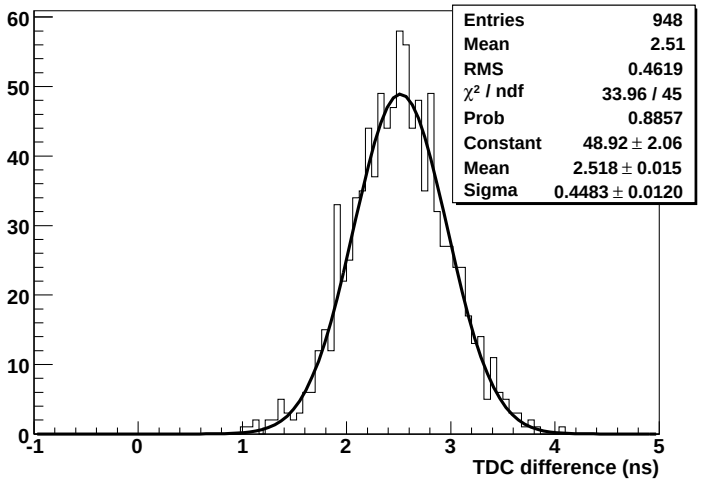

Figure 4.32: TDC peak difference between day 239 (August 27, 2006) and day 263 (September 20, 2006) around cluster 65 (cluster = 50, 51, 52, 64, 66, 78, 79, 80).

A very small effect around the cluster 65 seems to be present. Fig. 4.32 shows TDC peak difference between the two samples selecting only the 8 CLUSTERs close to cluster 65, while Fig. 4.33 shows the TDC peak difference for the CLUSTERs around cluster 60. The results are summarised in Tab. 4.7, also with the results of an odd-even study. No effects are visible: the peak shift is the same for CLUSTERs around CLUSTERs 65 and for CLUSTERs around cluster 60. Also the σ values are very close.

The effect becomes visible in peculiar conditions like those of Fig. 4.7 (4 CLUSTERs are offline on the edge of the carpet), but the TDC shift is only $\sim 0.5\ ns$. We conclude that the effect of off-line CLUSTERs on the TDC calibration is negligible.

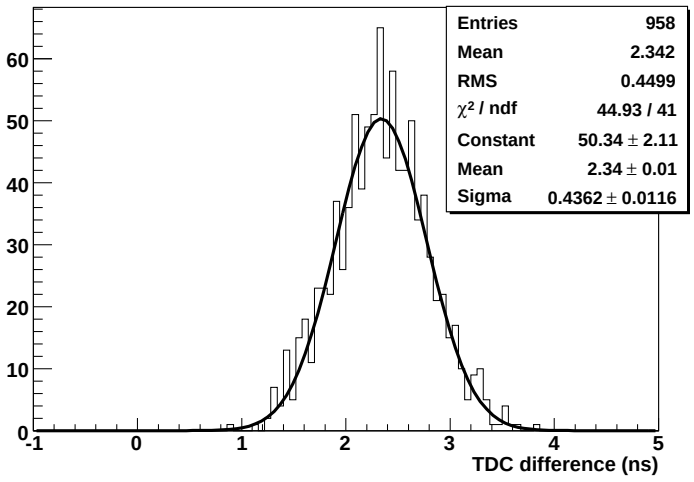

Figure 4.33: TDC peak difference between day 239 (August 27, 2006) and day 263 (September 20, 2006) around cluster 60 (cluster = 45, 46, 47, 59, 61, 73, 74, 75).

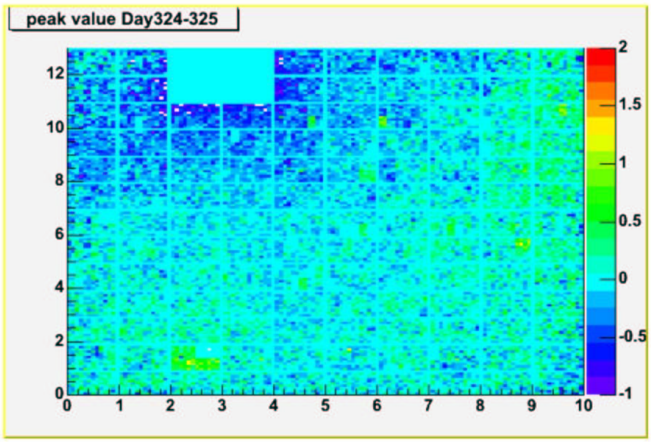

Figure 4.34: TDC peak difference between days 324 (November 20, 2006) and day 325 when CLUSTERs 33, 34, 47 and 48 were on and off, respectively.

difference	peak (ns)	σ (ns)	X cluster	days
even - odd events	-0.046 ± 0.014	0.40 ± 0.01	65 on	263
even - odd events	0.032 ± 0.014	0.40 ± 0.01	65 off	239
even - odd events	0.116 ± 0.016	0.41 ± 0.01	60 on	263
even - odd events	0.000 ± 0.015	0.43 ± 0.01	60 on	239
on-off	-2.245 ± 0.016	0.45 ± 0.01	65 on-off	239-263
on-on	-2.561 ± 0.017	0.44 ± 0.01	60 on-on	239-263

Table 4.7: TDC differences (peak and standard deviation) around test CLUSTERs (65 and 60).

4.5 Automatic procedure to update calibration file

An automatic procedure has been implemented in order to update the calibration file when some changes occur in the operation conditions of the detector. The selection of 5 periods for calibration (see section 4.4) is a good approximation but we verified unexpected changes can often occure during short periods of data-taking. Therefore we implemented a procedure to update automatically the calibration. The general idea is to provide a file calibration day-by-day looking at the differences of TDC peak values with respect to the data of a reference day (now September 20, 2006) used for the CP calibration, (see formula 4.14). The day-by-day procedure goes as follows:

- reading of 30 files with size greater than 500 MB, in order to have a significant statistics (almost 250×10^3 entries per pad)
- filling of 15600 histograms (one per pad) with the TDC values
- determination of TDC peak values by means of the Gaussian fit of the histograms
- output of a file ascii with useful informations (cluster number, pad number and TDC peak values)
- comparison of peak values of the examined day with those of the reference day
- production of the new calibration file using the formula (4.14)
- output of the new calibration file
- output of a root file containing a tree with the following variables:

- *day = day number*
- *year = year*
- *cluster = cluster number*
- *pad = pad number*
- *peak = TDC peak value in the day*
- *count = number of entries for pad*

- *sigma = standard deviation of Gaussian fit of TDC distribution*
- *diff = TDC peak difference with respect the reference day*

When a new trigger is introduced and the data with the old trigger are calibrated, the first TDC values with the new trigger can be used as reference values (T_0) in the formula (4.14).

5

Main results of ARGO-YBJ after calibration

In the search for cosmic point γ-ray sources with ground based arrays the main challenge is the rejection of the background due to charged cosmic rays. Therefore a good angular resolution is needed in order to reduce the search angular window and maximize the ratio signal/background. Angular resolution depends on the fluctuations of the shower development and on detector noise (time offsets randomly distributed on different portions of the detector, electronics effects, environmental noise, random errors in the reconstruction). Also the accuracy in estimating the arrival directions is mandatory in order to associate the signals with sources observed in other wavelengths. Systematic pointing error (see sec. 3.1) arises from possible detector misalignment and systematic errors in the reconstruction algorithms. Thus the timing calibration of the detector is fundamental: the residual correction and the systematical CP correction are devoted to improve the angular resolution and the absolute pointing, respectively. The effective improvements due to the calibration are presented in this chapter.
Moreover the improvement of the angular resolution depends strongly on the knowledge of the fine time and space structure of the shower disk, especially near the shower core. Measurement of the EAS disk structure was first attempted by Bassi, Clark and Rossi in 1953 [43] and continued up to date [44]. Connection between measurements close and far from the core was attempted by Linsley [45] on the basis of [46] and [47, 48]. Linsley's parameterization of the front thickness [49] is commonly used for correction of delays and improvement of array angular resolution. Some authors reported also modulations in time and sub-structures of EAS front [50, 51], making the scenario more and more intriguing. In this chapter a preliminary measurement of the average EAS disk structure will be presented comparing

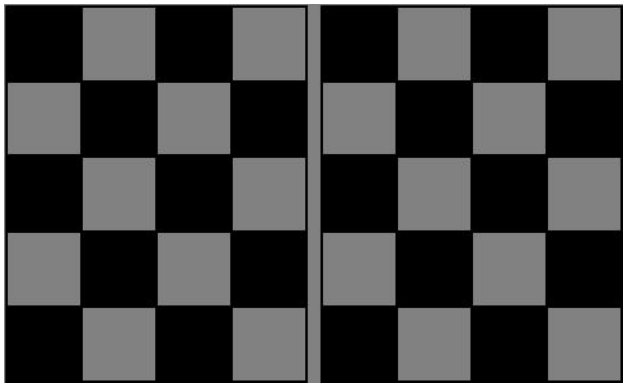

Figure 5.1: Chess board method. The two subarrays, the white and black array (or even-numbered and odd-numbered arrays), are handled as indipendent ones which view the same shower. The reconstructed angles by the two arrays are compared.

data with MC. This measurement could permit a better determination of EAS disk structure, a study of fluctuations and correlations between front profile, front thickness and core distance, as well as to reveal the presence of structures on the shower front.

5.1 Angular resolution: data-simulation comparison

After the timing calibration, the angular resolution has been estimated by means of the chess-board method. The detector is divided into two indipendent sub-arrays (white and black, as in Fig. 5.1). Each event is reconstructed separately on both the two sub-arrays [52, 53]. In this study the Ψ_{72} parameter is used, defined as the range in the angular distribution which contains 72% of the events. In Fig. 5.2 the opening angle Ψ_{72} calculated via the chess board method with data collected with ARGO-130 is compared, as a function of PAD multiplicity, to the MC simulation. The upper scale shows the estimated median energy of triggered events for the different multiplicity bins. As it can be seen, there is a fine agreement of the simulated result with the experimental one, thus validating both MC code and calibration. The resulting resolution is less than about 0.5° for showers with at least 100 hits (fired PADs) and at the level of 0.1° for very large multiplicity events.

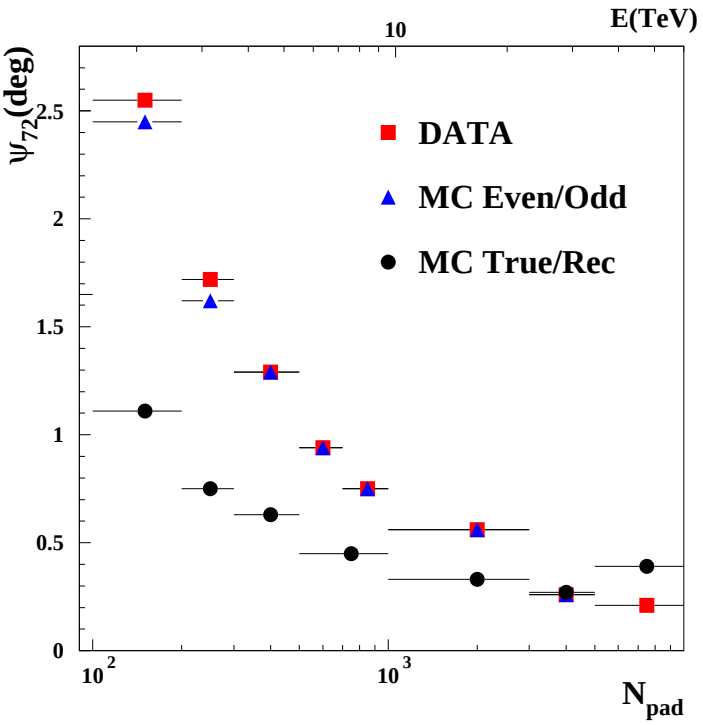

Figure 5.2: Comparison between the angular resolution for MC simulation and ARGO-130 data as a function of the pad multiplicity. The upper scale shows the estimated median energy of triggered events for the different multiplicity bins.

5.2 Moon shadow results

The analysis of the deficit of cosmic rays from the direction of the Moon is a well known method to determine the angular resolution of an EAS array [42]. Another aim of this method is to determine the orientation of the detector relative to the celestial coordinates and to investigate the systematical pointing accuracy. From July 2006 to October 2006 ARGO-YBJ detector has been put in data taking observing the Moon for $\sim$ 65.9 hours. Once the arrival direction is reconstructed, the events are assembled into sky maps. The maps are centerd on the Moon's position in equatorial coordinates [54]. The map consists of square bins of 0.1° side. In order to map equal areas of the sky into bins no matter what the Moon's position was, the coordinates used for the maps are $\Delta\delta = \delta_{event} - \delta_{Moon}$ on the ordinate and $\Delta\alpha = (\alpha_{event} - \alpha_{Moon})cos\delta_{event}$ on the abscissa, where δ is the declination and α is the right ascension. Once the background estimate is made, background maps are assembled in exactly the same way as the events maps. The two maps could then be compared and search technique applied to look for a deficit in the data maps compared to the background maps. The background estimate method used in this analysis depends on the fact that the flux of cosmic rays is isotropic in right ascension. This leads to the assumption that any real detected event in local coordinates could be associated to any detected time. All of the events detected in a short time interval are used to generate a fake data set as follows. The measured local coordinates (θ,ϕ) of each real event are paired with a time chosen randomly from the time interval. This set (t,θ,ϕ) constitutes a new fake background event. That is the fake event comes from the same local direction as the real event but at different time. To reduce statistical fluctuations, 10 fake events are generated for each real event. The effect of this method, the so-called "time swapping method", is to mix up the times of the events in the data sample. It is equivalent of randomly reassigning a new right ascension to each event, but keeping the declination of the event unchanged. This is because the selection of a new time is equivalent to a rotation of the celestial sphere with respect to the Earth. A weight is given to each fake event depending on the rate of the run, The fake data set has the same distribution in local coordinates as the real data have. The 2-dimensional sky maps may be analyzed directly. The ARGO-130 Moon shadow maps have been smoothed using a circular bin of about 1°. This has the effect of drawing out features in the map that occur on scales of 1°, such as the Moon deficit. The value of 1° is a typical choise for this kind of analysis and it is compatible with the angular resolution. From the square bins of 0.1° map a second map is constructed. A circular window of 1° radius is made summing the square bins. This window is then moved

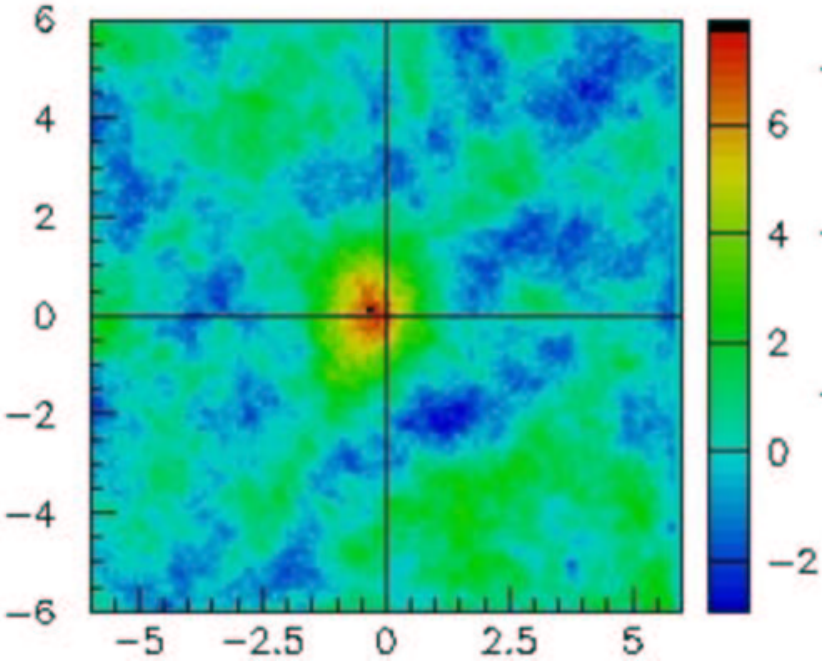

Figure 5.3: Significance of ARGO-130 Moon shadow for showers with $\theta < 50°$. The color scale indicates the significance of the deficit on a 0.9° search window centered on the $0.1° \times 0.1°$ bin.

at a step of 0.1° in both direction East-West and North-South. As a result, these circular bins are not indipendant one from another. The event maps and background maps are smoothed in the same way. Starting from these maps a final map is obtained putting in each bin the statistical significance $n_\sigma = \frac{N_{ev} - N_{bkg}}{\sqrt{N_{bkg}}}$, where N_{ev} is the observed number of events and N_{bkg} is the expected background. Fig. 5.3 shows the resulting smoothed map of the significance. the coordinates used for the maps are $\Delta\delta$ on the ordinate and $\Delta\alpha$ on the abscissa. The scale given on the right indicates the significance in each $0.1° \times 0.1°$ bin. The statistical significance of the dip due the shadow of the Moon is $\sim 7.9\sigma$ for events with a PAD multiplicity greater than 200.

5.3 The time structure of the extensive air shower front

Time and space structure of the extensive air shower disk depends on properties of the primary particle, on its energy and interaction mechanisms

with air nuclei. Questions related to cosmic rays sources, to energy spectrum and to elemental composition are still open challenges for investigation. Measurements of shower parameters with different detection techniques are required for a detailed knowledge of the shower front. A sketch illustrating the technique for studying an extensive air shower front with a surface detector is shown in Fig. 5.4. A flat array of detectors can measure the particles arrival times and densities at ground. Moreover the improvements of the simulation techniques used to describe the particle transport through the atmosphere [55, 56, 57, 58] allow an increasing degree of confidence in connecting signature of the primary cosmic ray to the observables as detected at ground. The high space-time granularity of the ARGO-YBJ detector allows a fine sampling of the shower front close to the core. The detector timing calibration (see Chap. 4) has been taken into account for this analysis.

5.3.1 Definition of the observables

The time structure of the shower disk has been studied as a function of distance to shower core in intervals of 1 m up to 40 m. The distance to core is computed on the shower plane, i.e on a plane perpendicular to the shower axis, which is specified by zenith angle θ and the azimuth angle ϕ of the direction of incidence. Thus the x,y coordinates have been rotated of an angle ϕ and Δx-distances have been projected on the shower plane as in the following (see also Fig. 5.5):

$$\begin{pmatrix} \Delta x_\phi \\ \Delta y_\phi \end{pmatrix} = \begin{pmatrix} x_i - x_c \\ y_i - y_c \end{pmatrix} \times \begin{pmatrix} \cos\phi & \sin\phi \\ -\sin\phi & \cos\phi \end{pmatrix}$$

$$\begin{matrix} \Delta x' = \Delta x_\phi \cos\theta \\ \Delta y' = \Delta y_\phi \end{matrix} \qquad R = \sqrt{(\Delta x')^2 + (\Delta y')^2}$$

where x_i and y_i are the fired PAD coordinates and x_{core} and y_{core} give the reconstructed position of the shower core in the detector plane. The following observables have been studied in the energy range between few TeV up to 20 TeV as a function of distance to shower axis:

- **the curvature** of the shower front as the mean of time residuals with respect to a planar fit (T_d in Fig. 5.4)

- **the thickness** of the shower front as the root mean square (RMS) of time residuals with respect to a conical fit (T_S in Fig. 5.4).

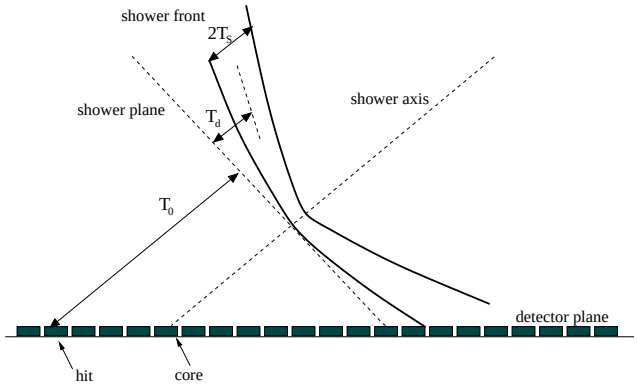

Figure 5.4: Sketch of shower front geometry and observables.

A set of well reconstructed data consisting of about 10^6 with ARGO-130 has been selected for this analysis. The event selection has been performed reconstructing the core with the algorithm LLF2 (see Sec. 2.6 in Chapter 3) over an area of $20 \times 20\ m^2$ centered on the carpet. A hit multiplicity greater than 200 and a quality cut on the χ^2/dof of the fit has been applied in order to reject mis-reconstructed events. A Monte Carlo study has shown that the applied cuts select well reconstructed events, mostly landing within the array (contained events).

5.3.2 Characteristics of the shower front

Fig. 5.6 shows the mean of time residuals with respect to a planar fit as a function of distance to shower axis for different PAD multiplicities and for different zenith angles less than 45°. It can be derived from simulation (see Fig. 5.7) that hit multiplicities of 200, 400, 600 and 800 correspond to average primary energies of about 4, 7, 11 and 15 TeV (for proton primaries with zenith angle less than 15°). The deviation from a planar fit increases with distance (up to about 8 ns at 40 m) and depends only weakly on hit multiplicity and zenith angles in the considered energy range. Fig. 5.8 shows the RMS of time residuals with respect to a conical fit as a function of distance to shower axis for different pad multiplicities and for zenith angles less than 15°. The thickness of the shower front (T_S, see Fig. 5.4) increases with distance (up to about 7 ns at 40 m) without a significant dependence on hit multiplicity in the considered energy range. No significant dependence on zenith angle has been observed both, for shower curvature and thickness, up to 45°.

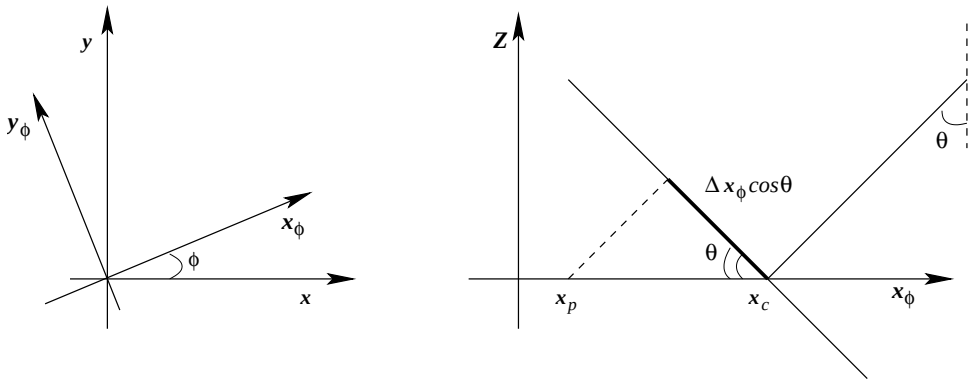

Figure 5.5: Sketch of rotations and projections performed for this analysis.

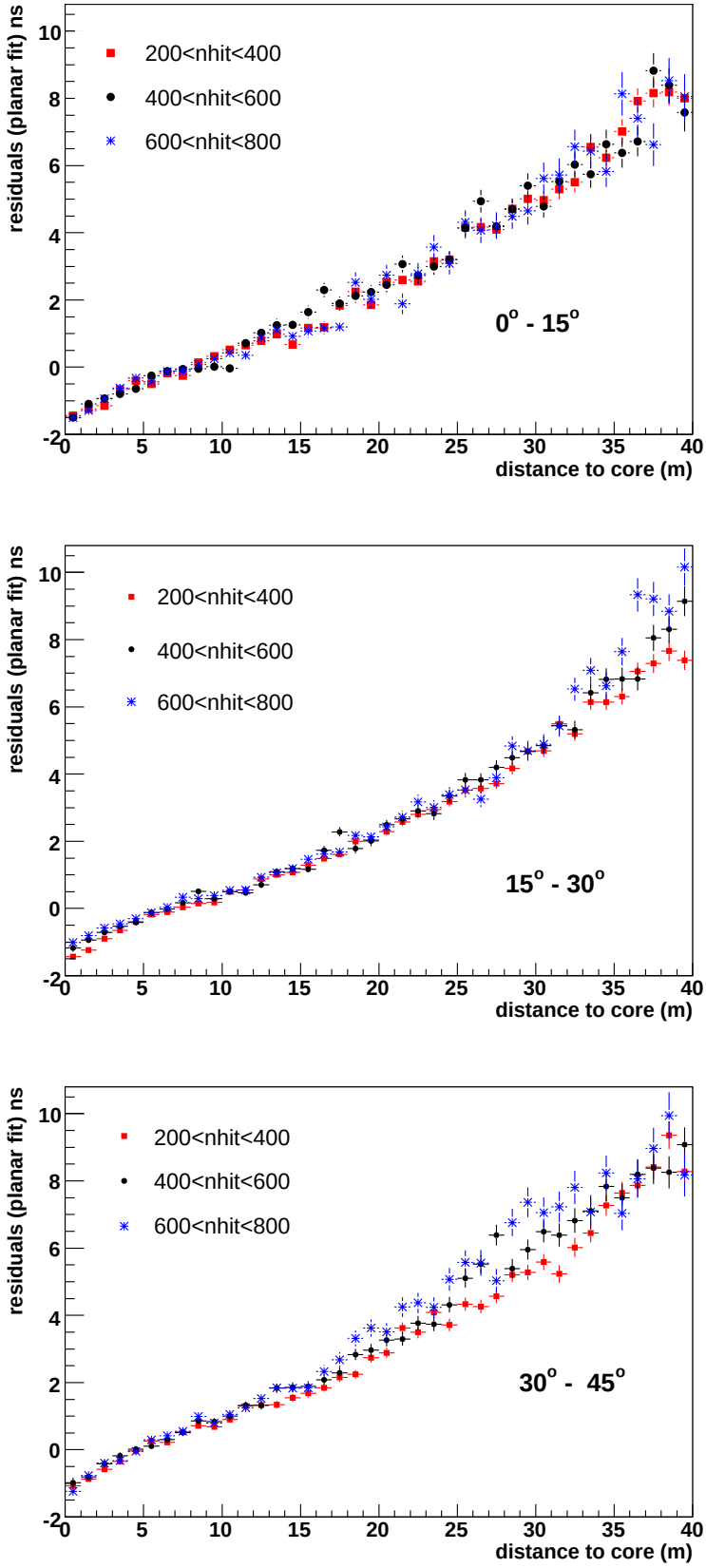

Figure 5.6: Real data - Mean of time residuals with respect to a planar fit as a function of distance to shower axis for different PAD multiplicities and different zenith angles less than 45°.

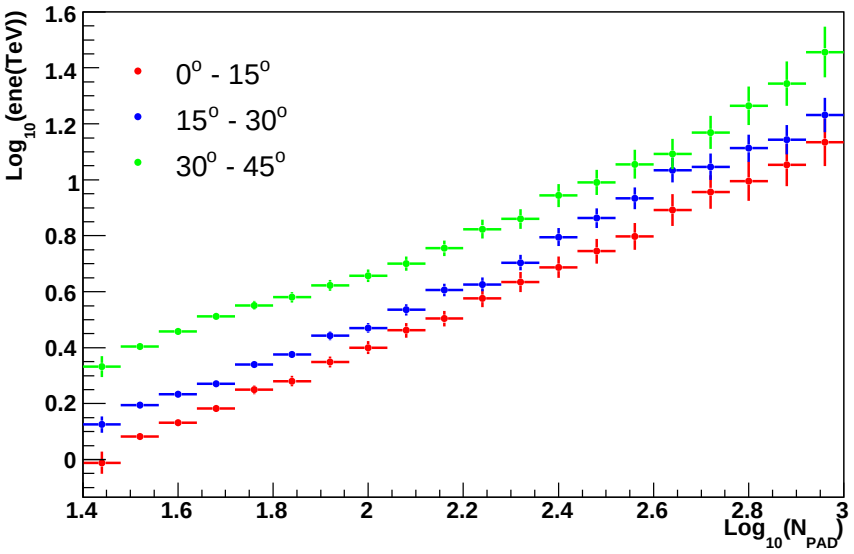

Figure 5.7: Simulation - Energy(TeV) versus PAD multiplicty (protons). For a given multiplicity the mean energy of the primary particle increases for inclined showers.

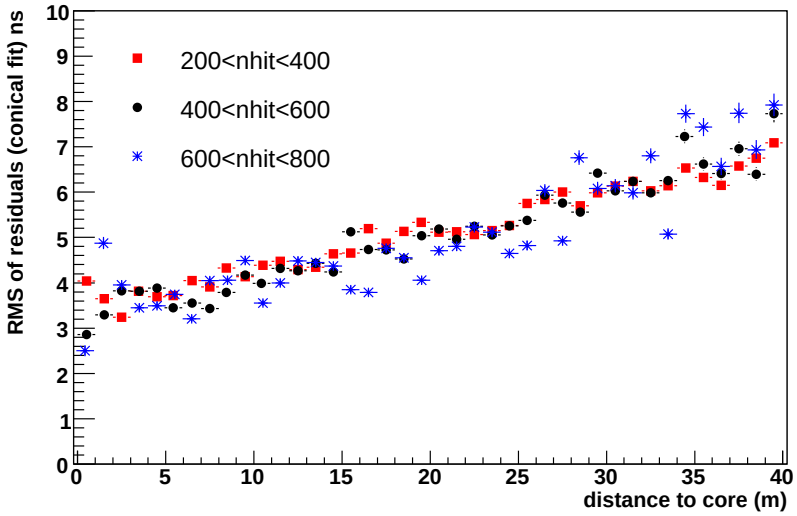

Figure 5.8: Real data - RMS of time residuals with respect to a conical fit as a function of distance to shower axis for different PAD multiplicities and zenith angles less than 15°.

5.3.3 Comparison Data-MC

A Monte Carlo study has been performed using a sample of about 6×10^6 proton-induced showers with zenith angle less than 45° and azimuth angle between 0° and 360°. The showers have been generated with CORSIKA (version 6.203) with a power law energy spectrum of -1 and in the energy range between 100 GeV and 1000 TeV. It has been chosen the package FLUKA (FLUctuating KAscade) [56] for low-energy hadronic interations and QGSJET01 [61] (Quark Gluon String Model with JETs) for high-energy hadronic interactions. The detector response has been simulated in detailed with a GEANT3 (v3.21) based code [62] (ARGOG). The areas of generation are listed in Tab. 5.1: they have been chosen much larger than the geometrical area of ARGO-YBJ because air showers may trigger the detector even if their core is very far. A system of weights has been then used to get the corrected triggering rates.

A preliminary comparison between data and simulation is discussed. Fig. 5.9

Energy range (TeV)	area of generation (m^2)
0.1-0.3	200×200
0.3-1	250×250
1-3	250×250
3-10	300×300
10-30	350×350
30-100	500×500
100-300	800×800
300-1000	1000×1000

Table 5.1: Area of generation used for the simulation.

show the distribution of pad multiplicity and of reconstructed zenith angle from simulation in comparison with data. A fairly good agreement is generally found. Fig. 5.10 shows the time residuals with respect to a planar fit for data (blue bullets) and simulation (red boxes) (pad multiplicity between 200 and 400 and zenith angle less than 15°). An agreement is found up to a distance of 15 m. At larger distances, the measured front curvature tends to be larger than expected by simulation. Similarly, the measured shower thickness has been found to be systematically larger than expected and this effect is larger at small distances to the shower axis. As a final remark, it should be pointing out that this simulation doesn't contemplate the contribution of heavier primary nuclei and doesn't yet reproduce the case of multiple hits on the same pad. This may account for the residual

discrepancy observed at large multiplicity (see Fig. 5.9).

5.4 Mass Composition

To inspect the dependence of the studied observables on primary mass, a dedicated simulation has been performed for proton and photon showers. 5000 protons and 5000 photons CORSIKA showers have been generated in the energy range between 3 and 10 TeV with zenith angle between 0° and 15°. The RMS of time residuals with respect to a conical fit is shown in Fig. 5.4 as a function of distance to shower axis, for proton and photon primaries. The selected events are required to have pad multipliticities larger than 200 and reconstructed core within an area of 40×40 m^2 centered on the carpet.

Though the measured difference is very small (at the level of the time resolution of the detector), this observable could provide, on statistical basis, a clue to $\gamma/hadrons$ separation and mass composition studies.
A further study has been carried out to investigate the correlation of shower conicity, quantified by the conity parameter α, with the atmospheric depth at shower maximum X_{max} for proton and photon primaries. For the same simulation sample (5000 protons and 5000 photons CORSIKA showers, 3-10 TeV and zenith angle between 0° and 15°), a reconstruction with conical fit has been performed leaving alpha as a free parameter of the fit. The results are shown in Fig. 5.12. A weak (moderate) correlation of α with X_{max} has been found for proton (photon) primaries. Further studies and an extended simulation with heavier primaries are needed (and planned) to draw a conclusion.

As a final remark, it should be pointed out that the analysis presented in this chapter is supposed to be preliminary. Indeed, a better selection of the reconstructed observables and further simulation studies should be done in order to better clarify the differences between data and simulation.

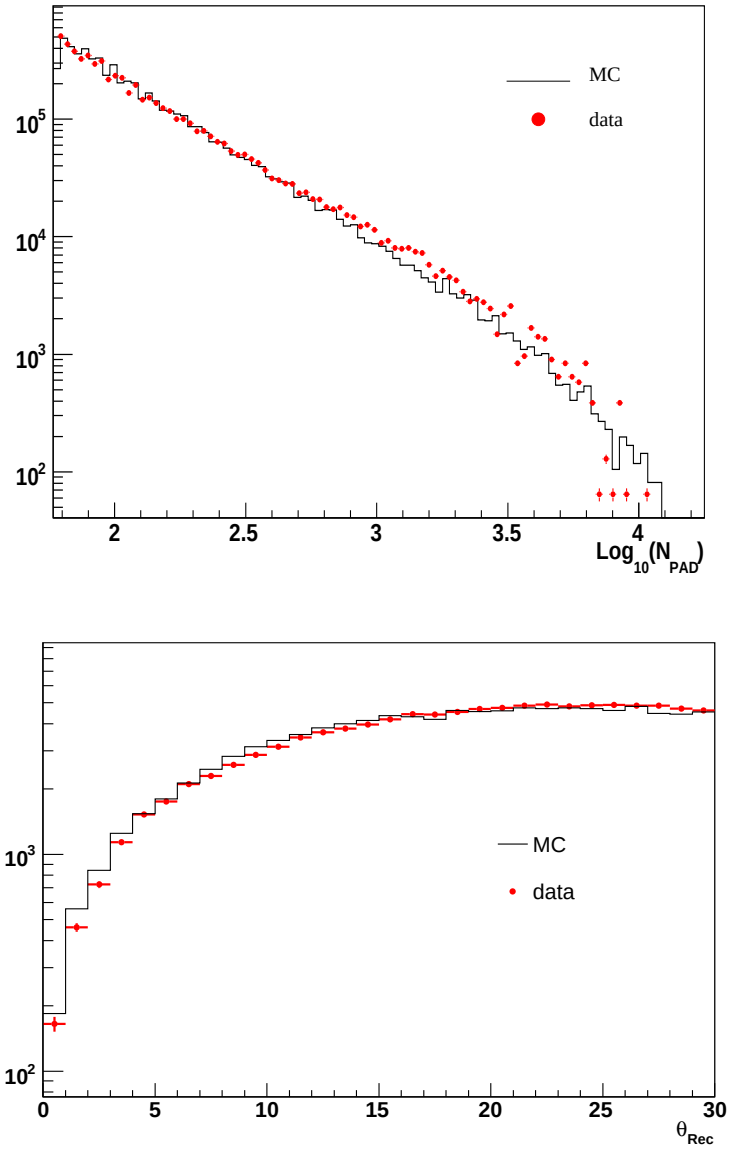

Figure 5.9: Comparison data MC - Good agreement with data and MC of PAD mutiplicity spectrum (first plot) and reconstructed zenith angle (second plot).

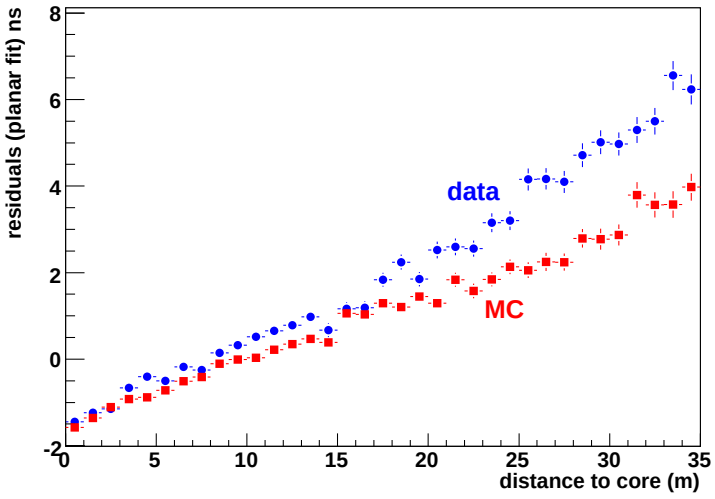

Figure 5.10: Time residuals with respect to a planar fit for data and simulation, for pad multiplicity between 200 and 400 and zenith angle less than 15°.

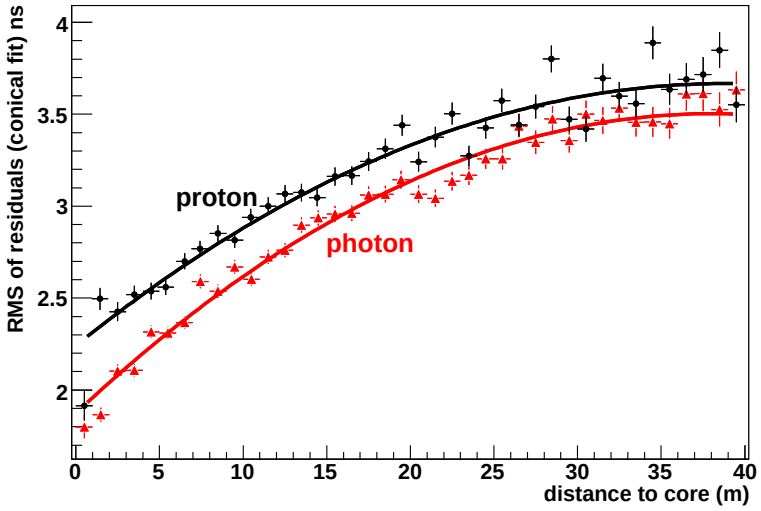

Figure 5.11: Simulation - RMS of time residuals with respect to a conical fit for proton and photon primaries, pad multiplicity between 200 and 400 and zenith angle less than 15°

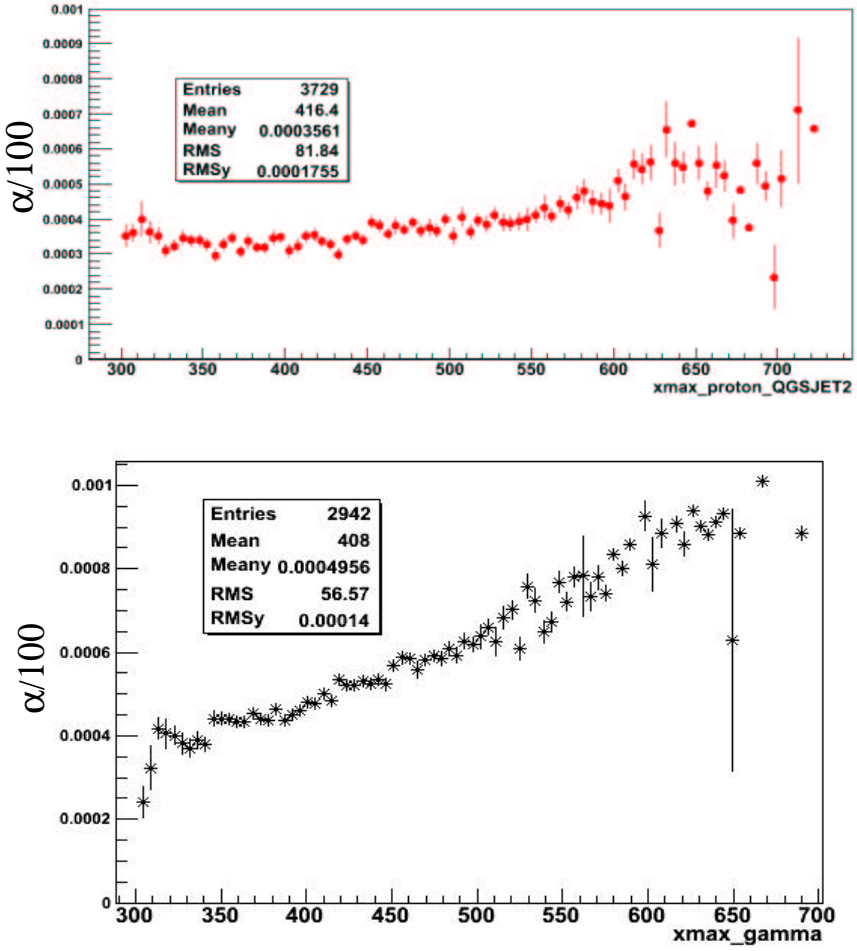

Figure 5.12: Simulation - Alpha conicity for proton (first plot) and for photon (second plot) primaries as a function of the atmospheric depth at shower maximum (X_{max}).

Conclusion

The most relevant items of this research are summarized in the following. An off-line timing calibration method has been studied and applied to the ARGO-YBJ detector. This method allows to calibrate the array repeatedly using the collected data and without disturbing the standard acquisition. The originality of the method is the definition of a Characteristic Plane (CP) introduced to analyze the effects of the time systematic offsets, such as the quasi-sinusoidal modulation on azimuth angle distribution. Residual and systematical CP corrections constitute the two steps of this timing calibration.

This procedure works also when a sinusoidal pre-modulation on the primary azimuthal distribution is present, for instance due to the geomagnetic field. The calibration has been performed with planar and conical fit of the showers on different configurations of the detector (ARGO-42, ARGO-104 and ARGO-130). The detector stability has been deeply studied in order to know when a new calibration was necessary. Also a fast update of the calibration has been introduced, it is based on the reproduction of the TDC distribution observed for calibrated data.

Simple and complete simulations have been performed to check the calibration procedure. The South-North azimuthal asymmetry at geomagnetic declination of ARGO-YBJ ($\theta_H \sim 45^\circ$) has been estimated by means of a full simulation. The development of EAS in the Earth's atmosphere down to the ARGO-YBJ altitude has been simulated with Corsika code, then the detector response has been simulated with a dedicated GEANT-based code (ARGOG). The simulated data have been analyzed with the same program (MEDEA++) used for real data.

As a result of the timing calibration, the angular resolution and the absolute pointing of the ARGO-YBJ detector are compatible with the expected ones. These results are confirmed by the chess-board analysis and by the Moon shadow measurement.

Moreover the proper time measurement permitted to undertake a deep study on the time structure of the shower front. Its curvature and its

thickness at different distances to the core have been studied. Preliminary results and comparisons with the simulation are available. The high space-time granularity of ARGO-YBJ, a more detailed analysis with larger statistics and a better selection of the reconstructed observables will permit a better knowledge of the fine time-space structure of the shower disk, especially near the core, improving the angular resolution and giving some important hints on energy, mass composition and shower age.

Bibliography

[1] J. Hörandel, *Advances in Space Research* **38** (2006), 1549.

[2] J. Hörandel, *Astropart. Phys.* **19** (2003), 193.

[3] B. Wiebel-Soth et al., *Astron. & Astroph.* **330** (1998), 389.

[4] M. Wiedenbeck et al., *28th Int. Cosmic Ray Conf.*, Tsukuba 4 (2003) 1899, 6019.

[5] W. Baade, F. Zwicky, *Phys. Rev.* **46** (1934), 76.

[6] E. Fermi, *Phys. Rev.* **75** (1949), 1169.

[7] W. Axford et al., *15th Int. Cosmic Ray Conf.*, Plovdiv 11 (1997), 132.

[8] M. Longair, *High Energy Astrophysics* **vol.2**, Cambridge, 1994.

[9] J. Hörandel, *astro-ph/0402356 v2*, 23 Feb 2004.

[10] P. Auger, R. Maze and T. Grivet-Mayer, *C. R. Acad. Sci. Ser.2* **206** (1938), 172.
P. Auger, R. Maze and T. Grivet-Mayer, *C. R. Acad. Sci. Ser.2* **207** (1938), 228.

[11] W. Kohlhorster, I. Matthes and E. Webber, *Naturwissenschaften* **26** (1938), 576.

[12] T.K. Gaisser and A.M. Hillas, *15th Int. Cosmic Ray Conf.*, Plovdiv 8 (1997), 353.

[13] D. Heck et al., *FZKA Report Forschungszentrum*, Karlsruhe (1998).

[14] www.lanl.gov/milagro.

[15] W. Heitler, *The quantum theory of radiation*, Oxford (1954).

[16] J. Matthews, *Astropart. Phys.* **22** (2005), 387.

[17] F. Arqueros et al., *Astron. Astrophys.* (2000), 359, 682.

[18] J.W. Fowler et al., *Astropart. Phys.* **15** (2001), 49.

[19] M. Glasmacher et al., *Astropart. Phys.* **10** (1999), 291.

[20] M. Amenomori et al., *Astrophys. Journal* **461** (1996), 408.

[21] T. Antoni et al., *Astrophys. Journal* **608** (2004), 865.

[22] M. Aglietta et al., *Astroparticle Physics* **3** (1994), 1.
M. Aglietta et al., *Astroparticle Physics* **21** (2004), 223.

[23] J. Abraham et al., *Nucl. Instr. and Meth.* **A523** (2004), 50.

[24] Z. Cao et al. for the ARGO-YBJ Collaboration, *29th Int. Cosmic Ray Conf.*, Pune 5 (2005), 299.

[25] G. Aielli et al., *Nucl. Instr. and Meth.* **A562** (2006), 92.

[26] S. Mastroianni et al. for the ARGO-YBJ Collaboration., *28th Int. Cosmic Ray Conf.* Tsukuba (2003), 769.

[27] D. Martello, C. Bleve, G. Di Sciascio, *27th Int. Cosmic Ray Conf* Hamburg Karlsruhe (2001).

[28] D. Martello et al., *28th Int. Cosmic Ray Conf.* (2003).

[29] P. Camarri et al., *29th Int. Cosmic Ray Conf.*, Pune (2005).

[30] C. Bleve et al., *ARGO-YBJ note 002/03.*

[31] A.M. Elø et al., *26th Int. Cosmic Ray Conf.*, Salt Lake City 5 (1999), 328.

[32] M. Nishizawa et al., *Nucl. Instr. Meth.* **A285** (1989), 532-539.

[33] A.A. Ivanov et al., *JETP Letters* **69** (1999), 288-292.

[34] G.W. Clark, *Phys. Rev.* **108** (1957), 450.

[35] H.H. He et al., *29th Int. Cosmic Ray Conf.*, Pune 6 (2005), 5-8.

[36] P. Bernardini et al. for the ARGO-YBJ Collaboration, *29th Int. Cosmic Ray Conf.*, Pune 5 (2005), 147-150.

[37] H.H. He, P. Bernardini, A.K. Calabrese Melcarne, S.Z. Chen, *"Detector Time Offset and Off-line Calibration in EAS Experiments"*, *Astroparticle Physics* (doi:10.1016/j.astrophys.2007.03.004).

[38] A.M. Elø, H. Arvela, *"The Timing Measurement in the Air Shower Experiment in Turku"*, *26th Int. Cosmic Ray Conf.*, Salt Lake City 5 (1999), 320 [OG.4.4.07].

[39] A.M. Elø, H. Arvela, *"Correction of Air Shower Timing Using Shower Data"*, *26th Int. Cosmic Ray Conf.*, Salt Lake City 5 (1999), 324 [OG.4.4.08].

[40] D. Martello and A. Surdo, *Internal Note ARGO-YBJ/2000-001* (2000).

[41] D. Heck, J. Knapp, J.N. Capdevielle, G. Schatz and T. Thouw, *Report FZKA 6019*, Forschungszentrum Karlsruhe (1998). *http* : $//www - ik3.fzk.de/ \sim heck/corsika/physics\_description/corsika\_phys.html$

[42] G.W. Clark, *Phys. Rev.* **108** (1957), 450.

[43] P. Bassi, G. Clark, B. Rossi, *Phys. Rev.* **92** (1953), 441.

[44] G. Agnetta et al., *Astropart. Phys.* **6** (1997), 301.

[45] J. Linsley, *Journal .Phys.* **G12** (1986), 51.

[46] C.P. Woidneck, E. Böhm, *Journal .Phys.* **A8** (1975), 997.

[47] J. Linsley, L. Scarsi, B. Rossi, *Phys. Rev. Lett.* **6** (1961), 485.

[48] J. Linsley, L. Scarsi, *Phys. Rev.* **128** (1962), 2384.

[49] J. Linsley, *Journal .Phys. G:Nucl. Phys.* **12** (1986), 51-57.

[50] H. Sakuyama et al., *Nuovo Cimento* **C6** (1983), 147.

[51] G.B. Khristiansen et al., *21th Int.Cosmic Ray Conf.*, Adelaide 9 (1990), 150.

[52] G. Di Sciascio and E. Rossi for the ARGO-TBY collaboration, *Proc. of the "Incontro Nazionale di Astrofisica delle Alte Energie"* (2003).

[53] G. Di Sciascio et al., *29th Int.Cosmic Ray Conf.*, Pune India (2005).

[54] S. Vernetto et al., *26th Int.Cosmic Ray Conf.*, Salt Lake City (1999): astroph/9906185

[55] D. Heck et al., *Report FZKA 6019*, Forschungszentrum Karlsruhe.

[56] A. Fassoó et al., *Fluka: Status and Prospective of Hadronic Applications*, *Proc. Monte Carlo 2000 Conf.*, Lisbon.

[57] N. Kalmykov et al., *Nucl. Phys.* **B** (Proc.Suppl.) **52B** (1997), 17.

[58] J. Horandel, *Journal Phys. G:Nucl. Part. Phys.* **29** (2003), 2439.

[59] D.E. Alexandreas, G.E. Allen, D. Berley et al., *23th Int. Cosmic Ray Conf.*, Calgary 1 (1993), 212.

[60] A.V. Plyasheshnikov, *22th Int.Cosmic Ray Conf.*, Dublin 1 (1991), 488.

[61] N.N. Kalmykov and S.S. Ostapchenko, Yad. Fiz. **56** (1993), 105.

[62] CERN Program Library Long Writeup W5013 (1994)